UNIVERSITY OF PADOVA

Master Thesis in Physics

GAIA GALAXY SURVEY

SIMULATED OBSERVATION OF GALAXIES WITH ESA GAIA SATELLITE

by

Mattia Vaccari

Supervisor	Cosupervisor	Cosupervisor
Prof. A. Saggion	Prof. E. Høg	Prof. P.L. Bernacca
Department of Physics	Astronomical Observatory	Department of Astronomy
University of Padova	University of Copenhagen	University of Padova

ACADEMIC YEAR 1999-2000

Contents

Introduction

"Galaxies are to astronomy what atoms are to physics"

Allan Sandage

The understanding of the structure, formation and evolution of galaxies is certainly one of the most important challenges for contemporary astronomy, not only because galaxies are important in their own right, but also because their study can provide clues to new laws of physics.

In recent years, extragalactic astronomy has experienced a great progress both from the observational and theoretical point of view, thanks to developments in both instrumentation and numerical techniques. On the observational side, this field of astronomical research has traditionally been dominated by large-aperture ground-based telescopes, capable of peering deeply into the sky. With the advent of the Hubble Space Telescope, however, and particularly thanks to the superb, large-field-of-view images provided by WF/PC and WFPC2, the dramatic scientific case for extragalactic studies at high spatial resolution, presently achievable from above the Earth's atmosphere only, has been fully demonstrated, to the extent that the next planned large-aperture space observatory, the Next Generation Space Telescope, has as its main scientific goal the investigation of the formation and evolution of galaxies.

In this historical context, following on the huge success of Hipparcos, the first dedicated astrometric satellite, some three years ago ESA has started, in collaboraton with the European astronomical community, the feasibility studies for GAIA, a revolutionary astrometric satellite mission. According to its present design, established after extensive industrial and scientific studies, the GAIA satellite will perform astrometric and photometric measurements of unprecedented accuracy over a magnitude-limited sample of about a billion stars brighter than $V \simeq 20$. For more than a hundred million stars, the satellite will also perform radial velocity measurements so as to identify the position of stars in the six-dimensional phase-space, in the first stereoscopic survey of our Galaxy. The GAIA mission is now a short-listed candidate for selection by the European Space Agency as Cornerstone 5 of its Horizons 2000 Scientific Programme. Selection is expected in September 2000 and, if selected, GAIA could be launched around 2009.

In the framework of the feasibility studies for the GAIA mission, the opportunity of performing galaxy astrometric and photometric observations in parallel with star observations was suggested in early 1998 by Prof. Erik Høg from the Astronomical

Observatory of the University of Copenhagen. This thesis, carried out in part at the Astronomical Observatory of the University of Copenhagen and in part at the Asiago Astrophysical Observatory of the University of Padova, is the result of a study intended to demonstrate the feasibility and scientific potential of such observations. Preliminary results were presented in three reports (Vaccari and Høg 1999a, Vaccari, Høg and Makarov 1999 and Vaccari and Høg 1999b) to the Science Advisory Group established by ESA for the GAIA mission, which has now included the observation of galaxies in the mission baseline design under the name of GAIA Galaxy Survey.

The GAIA Galaxy Survey is basically a nearly all-sky, high-spatial-resolution, multi-color and multi-epoch astrometric and photometric survey of the central regions of galaxies brighter than $I \simeq 17$. More than 3 million galaxies would be observed in at least 4 colors with a spatial resolution better than 0.4 arcsec. Such observations would yield a large, high-quality and uniform dataset that could be used for statistical studies of spatial distribution and core photometric structure of bright galaxies down to low Galactic latitudes. The galaxy spatial distribution on the sky will be used to probe the large-scale structure of the Local Universe, whereas high-spatial-resolution surface photometry of the galaxy innermost regions will shed light onto the wealth of structures that appear to be present at the center of most galaxies. In the foreseeable future, an observation campaign of this kind could not be carried out by other telescopes, either from the ground, due to seeing and related difficulties in star-galaxy discrimination, or from space, due to the premium on the observing time of space observatories. Galaxy observations could instead easily be obtained by GAIA with only a small effort in terms of mission design, data transmission and analysis. Besides providing the astronomers with an unprecedented wealth of fundamental information on our Galaxy, the GAIA mission could thus also yield a significant contribution to the study of external galaxies.

Chapter 1

The Historical Context of the GAIA Mission

The origin and development of every momentous scientific undertaking is profoundly influenced by the historical context in which it arises. Following this general rule, the GAIA mission has its roots in the recent dramatic development of space astronomy, and specifically in the renaissance experienced by astrometry thanks to space techniques. Although this study deals with the possibility of performing galaxy observations with the GAIA satellite, an outstanding astrometric accuracy is an essential prerequisite to implement the galaxy observation strategy that is here proposed. More in general, most characteristics of the present mission design are best understood when considering that GAIA is mainly an astrometric satellite. It will therefore be useful to briefly review the advantages offered by space astronomy over ground-based astronomy as well as to describe in some detail the characteristics and results of Hipparcos, the ESA astrometric satellite which can be regarded as GAIA "ancestor" and to which GAIA design owes much[1].

1.1   The Advantages of Space Astronomy

Since the 1950s, artificial satellites have been used for a wide range of applications, thus providing the vast knowledge that was necessary in order to launch and operate relatively low-cost satellite-borne astronomical telescopes. Even though such early missions were primarily motivated by the need of extending the observations to almost all wawelengths of the electromagnetic spectrum, in the following we will concentrate our attention on optical telescopes, owing to the fact that GAIA will observe in the optical region.

Roughly speaking, the performance of an imaging telescope can be expressed in terms of its sensitivity and angular resolution. In principle, both can be improved by increasing the aperture, and thus the light-gathering area[2]. Unfortunately, in recent years

---

[1] A short review of the most significant steps in the history of astrometry is given in Appendix B.

[2] The angular resolution may alternatively be increased by means of interferometric techniques, e.g. by combining the signals from two or more telescopes. Ideally, one should thus obtain a resolution

conventional monolithic mirrors have virtually approached the practical maximum size. Besides, however large its aperture may be, the angular resolution of a ground-based telescope ultimately becomes limited by problems connected with terrestrial environment only. In order to cope with these difficulties, a wide range of new techniques, such as mosaic and light-weight mirrors, active and adaptive optics, was developed. Still the most direct way to do so is to position a telescope in a far enough place so as to make the influence of terrestrial environment negligible. This remarkably difficult undertaking is justified by the manifold substantial advantages of space-based astronomy over ground-based astronomy, which can be summarized as follows:

- **Atmospheric Turbulence and Refraction**: space and time variations in chemical and physical properties of the atmosphere cause variations in the refractive index of different atmospheric regions. Since a telescope collects light over a large area, differences in refraction along different paths lead to random and systematic deviations of light rays, which are referred to as atmospheric turbulence and atmospheric refraction, respectively. The problems posed by these two phenomena are quite different. Atmospheric turbulence smear the image of an otherwise point-like source to a spot whose Full-Width at Half-Maximum (FWHM) is called *seeing*. The typical seeing at a good observing site is of order 1 arcsec, and only 5% of the observations at a superb site such as Cerro Paranal, where ESO Very Large Telescope is being built, have a seeing better than 0.4 arcsec. Since the diameter of the Airy Disk of an 8 m aperture telescope is of order 35 mas[3], Atmospheric turbulence degrades the possible diffraction-limited angular resolution of such a telescope by at least an order of magnitude, and is therefore the main factor limitating the performance of currently available large ground-based telescopes. atmospheric refraction causes a systematic displacement of the positions of celestial bodies of order 1 arcsec, and therefore can in principle be corrected for, but the space and time varying correction to be applied is never perfectly determined, especially at large zenith angles, where the path followed by light rays through the atmosphere is particularly long. This is a strong limitation to the accuracy of wide-angle astrometry, which requires observations carried out with different telescopes and at different times to be compared and combined.

- **Atmospheric Extinction**: photons reaching Earth from space are scattered and absorbed by molecules and dust that populate the atmosphere. Photons in most wavelength regions are virtually completely absorbed, leaving only two relatively small "windows" available for ground-based astronomical observations, namely the optical window (300 nm $\lesssim \lambda \lesssim$ 800 nm) and the radio window (1 mm $\lesssim \lambda \lesssim$ 20 m). Even in the optical window, however, absorption and scattering dim and redden the celestial bodies to an extent increasing with zenith angle. Since the actual amount of atmospheric extinction is difficult to determine, with a ground-based

---

equivalent to that of a telescope with an aperture equal to the separation of the telescopes, or baseline. This is however fairly difficult to realize from a technological standpoint.

[3]Hereafter, mas and μas stand for a thousandth and a millionth of second of arc, respectively. The abbreviations and conversion factors of angular units used in this study are summarized in Appendix A.

telescope one usually has to measure the brightness of stars with respect to some reference star whose "true" brightness (i.e. the brightness as seen from outside the atmosphere) is reasonably well known, and then deduce the unknown star's "true" brightness. This procedure can prove very accurate, but requires that the reference star and the unknown star are very close in the sky, so that one has still to be able to correct for atmospheric extinction the brightness of an all-sky dense net of reference stars.

- **Mechanical Flexure**: the Earth's gravitational field tends to bend the truss structure of large, heavy ground-based telescopes, so that the resulting image is distorted. This distortion can be made negligible by positioning a satellite far from Earth, e.g. in a geostationary orbit or in the L2 Lagrangian point of the Sun-Earth system.

- **Thermal Stability**: a ground-based telescope is subject to temperature variations characterizing the Earth's surface, which in turn cause continuous expansion and compression of the instrument's parts. The resulting image distortion can be reduced by putting a satellite in an orbit such that the exposition to sunlight is approximately constant. Besides, the low temperature of space environment simplifies the detectors' cooling, which is necessary in order to reduce the detectors' readnoise.

- **All-Sky Coverage**: a ground-based telescope can efficiently observe a limited portion of the sky depending on its geographical coordinates. In order to compile an all-sky astrometric catalogue, for instance, one has to combine several partially overlapping regional catalogues. Each of these will introduce its own systematic errors, thus degrading the goodness of the single catalogues' results. For this reason ground-based narrow-field astrometry is usually much more accurate than ground-based global astrometry, where systematic errors often dominate the error budget. This issue is particularly important because any absolute astronomical reference system obtained from radio observations of extragalactic objects, such as the recently established International Celestial Reference System (ICRS, Arias et al. 1995), needs a routinely accessible optical counterpart. Hipparcos observations have for instance been linked to the ICRS, thus discovering errors of several tenths of arcseconds in the most accurate optical astrometric catalogue obtained from ground-based observations, the FK5.

- **Sky Background**: even at a superb observing site, even in the best environmental conditions, the sky is never completely dark. This is a particularly serious drawback when, as in surface photometry, one has to subtract the contribution from the sky background from the observed surface brightness distribution of faint diffuse objects. The sky background as seen from space is substantially fainter than from the ground. Besides, its most rapidly varying components seen in ground-based images originate in the atmosphere and are therefore absent in space observations.

> This allows a much more accurate correction for the sky background than it is generally possible to accomplish from the ground.

Space observations were first carried out from rockets in the 1960s, but it was not until the 1970s that they were extensively carried out from Earth satellites. Since then, thanks to the many advantages we mentioned, space-based astronomy has continuosly gained in importance. Among other factors, this rapid development has been made possible by the close collaboration between the scientific community, the industry and the new-born national and international space agencies. In a European context, the efforts of the different national space agencies were coordinated by the European Space Agency (ESA), whose activity has in time greatly contributed to the success of the European astronomical community[4].

1.2   The Hipparcos Mission

Astrometry at first did not benefit from the revolution brought in astronomy by space observations. This was partly due to its lack of "appeal" with respect to other fields of astronomical research, but it is fair to say that the lack of ideas on how one could fully exploit the advantages of space environment for astrometric measurements also played an important role. Finally, in the late 1960s a good idea for an astrometric satellite by Pierre Lacroute finally managed to stand out. At the time the case for accurate parallax determinations was very strong, because they were needed to calibrate the extragalactic distance scale by measuring the distances to nearby stars. The traditional method for ground-based parallax determination made use of photographic plates taken with instruments with very long focal lengths, and thus with very small fields of view. These could only yield a star's parallax relative to an average parallax of a few background stars, whose parallactic displacements were in the same direction but in general of different sizes. An estimate of this background parallax gave an approximation for the correction to be applied to obtain an absolute parallax (see Section 2.1). Such estimates were however difficult and uncertain, and it was not uncommon to see, between independent parallax determinations for the same star, differences much larger than the accuracies indicated for the single determinations. As a consequence, the accuracy of ground-based parallax determinations, painstakingly obtained for a few thousand stars, was at best of the order of 8 mas. To a first approximation, the distance range within which the distances can be determined with an accuracy better than a given threshold is inversely proportional to the accuracy of parallax determinations, and thus the number of objects whose distances are "well-determined" increases very rapidly as the error on the parallax decreases. Therefore, the poor accuracy achievable from the ground was a severe limitation, for many types of stars of great astrophysical importance, including the most reliable standard candles, were too rare to be found within the surveyable volume. Lacroute's basic idea was to combine the images from two areas widely separated on the sky onto one detector, and to do this several times a year. The parallactic

---

[4]A short history of ESA space science activities is given in Appendix C.

displacements of the two fields would be uncorrelated and therefore allow a reliable determination of absolute parallaxes. This technique could not be employed successfully from the ground, as it required a very well determined and stable angle between the two viewing directions, and determination of large angles from the ground is seriously affected by atmospheric refraction. The first proposal of a space mission implementing this technique was submitted to the French Space Agency in 1966, but its realization appeared too complex at that time, and in 1970 further studies were stopped. The basic idea survived within ESA, however, and thanks to the input of several new ideas originating from the study group assembled by ESA in 1975, the concept of a space astrometry mission became more and more realistic. In 1980, the Hipparcos[5] mission (ESA 1997a, ESA 1997b, van Leeuwen 1997 and Kovalevsky 1998), the first dedicated astrometric satellite mission ever, was finally approved by ESA. The basic requirement in order to have a sufficient scientific impact with respect to ground-based data was then considered the acquisition of astrometric data for about 100 000 stars evenly distributed over the sky with an accuracy better than 2 mas for positions and parallaxes and 2 mas/yr for proper motions. The astrometric data would be complemented by multi-epoch photometric data for all stars in the very wide Hp band. A second experiment, proposed by Erik Høg and consisting in an astrometric survey of a million stars complete to about $V = 11$, was later incorporated in the mission and named Tycho[6]. This parallel experiment would also acquire photometric data in two wide bands, B_T and V_T, roughly resembling the Johnson B and V bands, that would be useful to the main mission as well in order to correct the observations for chromatic aberration.

The mission design that was established in order to meet these requirements considered a spinning satellite in geostationary orbit whose spin axis preceded around the Sun-satellite direction, or Sun axis, thus allowing a complete and uniform coverage of the sky. The two viewing directions, perpendicular to the spin axis and separated by an angle very close to 58 deg which is called the *basic angle*, were projected on the same detector by the *beam combiner*, a mirror that was cut in two halves and glued back at an angle equal to half the basic angle. In order to accurately calibrate the basic angle on the basis of the satellite's smooth rotation, the satellite in general and the beam combiner in particular required a mechanically and thermally very stable environment, which was to be achieved thanks to the large distance from Earth characterizing geostationary orbits and to the constancy at 43 deg of the *Sun angle*, i.e. the angle between the spin axis and the Sun axis. The images from the two fields of view were then superposed on the focal plane by an all-reflective Schmidt-like telescope working in the visible with $\lambda/60$ rms mirrors and a small aperture of 29 cm. The detector system consisted of photoelectric detectors in conjunction with slit systems for signal modulation, and was in many ways similar to that which is used in meridian circles. In both cases the objects crossed the field of view, as a result of the satellite's and Earth's rotation, respectively.

---

[5] Hipparcos is both an acronym for HIgh Precision PARallax Satellite and a dedication to the second century BC Greek astronomer Hipparchus, whose name is generally associated with the first "modern" catalogue of star positions.

[6] After the 16th century Danish astronomer Tycho Brahe (1546–1601), who discovered the nova in Cassiopeia in 1572 and compiled the most accurate pre-telescope era catalogue of positions of stars.

The central part of the focal plane was equipped with an image dissector tube and used for the main experiment, whereas at the two sides two photomultipliers were used for the star detection process that was necessary for the main experiment and for the Tycho experiment.

This revolutionary mission concept, however, posed some challenging problems that had never occurred before. At a very early stage of the mission, it became clear that the reduction of the large and complicated dataset which was to result for any star from the whole mission could not be accomplished in just one run, due to the huge computer resources that would be needed to do so. However, in 1976 already Lennart Lindegren designed a three-step reduction system which was to be adopted and which allowed to handle the problem with only a small loss of accuracy. Even so, the data reduction was to be very delicate, as there was no independent material available with which to compare Hipparcos results, and it was decided that it would be beneficial to the project if more than one group carried out the full data reduction process. This led to the establishment of two consortia, whose collaboration greatly improved the quality of the final catalogues. It was then necessary to select the stars to be observed, on the basis both of the desired scientific goals and of the mission's constraints, the most stringent of which being that the stars had to be uniformly distributed over the sky and that their positions at the epoch of observation had to be known *a priori* with an accuracy better than 1.5 arcsec. Following the submission of observing proposals, a laborious selection process involving massive simulation of observations brought to the identification of an optimal observing list of about 120 000 stars. All that was known about these in terms of astrometry, photometry, multiplicity information, spectral type and radial velocity was gathered in order to optimize the observation strategy and was later published in *The Hipparcos Input Catalogue* (Turon et al. 1992).

The satellite was designed and constructed by a European industrial consortium led by Matra Marconi Space and Alenia Spazio and on August 8, 1989 was launched into a geostationary transfer orbit by an Ariane 4 launcher. Despite the failure of the Apogee Boost Motor, which was to put the spacecraft into geostationary orbit but left it stuck in a highly elliptical one, the satellite acquired data for 3.5 years, significantly exceeding all the mission goals. In 1997, after painstaking verifications of the data quality and four years after the end of data acquisition, the mission results were finally published by ESA. *The Hipparcos and Tycho Catalogues* (ESA 1997a) contain high-quality astrometric data (positions, proper motions and parallaxes) with an accuracy[7] in the 0.5–2 mas range for about 120 000 stars (Hipparcos), and in the 10–60 mas range for over 1 000 000 stars (Tycho). The astrometric data were complemented by photometric data in the Hp band for Hipparcos stars and in the B_T and V_T bands for Tycho stars, and a great deal of additional data on variable and multiple stars was made available as well. The final results were about 1.5 to 2 times better than the original aims and improved the

---

[7] Following the glossary at the end of Volume 1 of ESA 1997a, in this work *accuracy* indicates the uncertainty of a measured quantity due to accidental and systematic errors, whereas *precision* denotes the uncertainty of a measured quantity due to accidental errors only. Accuracy and precision are often used synonymously with *external standard error* and *(internal) standard error*, respectively. Finally, *bias* indicates the uncertainty of a measured quantity due to systematic errors only.

accuracy of orders of magnitude with respect to ground-based measurements.

The astrophysical significance of such a large and uniform dataset became apparent early during the mission, and was later confirmed by the high and steady rate of Hipparcos-based articles' publication[8].

Besides, despite the careful reduction of the observations that had been carried out, it became clear that important information was still "hidden" in the raw Hipparcos and Tycho data. Therefore, even after the catalogues' publication, great care has been given at fully exploiting the scientific potential of the data. As a first step, proper motions with an accuracy of about 2.5 mas/yr were obtained independently by Urban, Corbin and Wycoff 1998 and Høg et al. 1998a for most Tycho stars by comparing Tycho positions with the one-century old positions of the Astrographic Catalogue stars obtained by Urban et al. 1998. The recently completed thorough re-reduction of Tycho raw data in combination with a large number of ground-based catalogues has then allowed to increase by a factor of 2.5 the number of observed stars. The resulting Tycho 2 Catalogue (Høg et al. 2000a and Høg et al. 2000b) contains positions and proper motions for the brightest 2.5 million stars in the sky, complemented by components of 7 500 resolved double stars with separation down to 0.8 arcsec. Further dedicated data reduction procedures are now being developed for an optimal treatment of double and variable stars, which will result in the largest duplicity and variability survey ever, the so called Tycho 3 Project. These improvements demonstrate a fundamental principle of astrometric measurements, namely that they are a particularly valuable resource for future analysis and comparison. The content of the Hipparcos, Tycho and Tycho 2 Catalogues are summarized in Table 1.1. These must be considered as the present state-of-the-art in astrometry, and may be compared with the measurement capabilities expected from GAIA, and described in Section 2.7, in order to evaluate the achievable progress.

In summary, the Hipparcos mission put an end to the long-standing strict separation between astrometry and astrophysics by dramatically demonstrating the deep astrophysical significance of extremely accurate global astrometric observations. A further improvement of orders of magnitude in terms of accuracy and number of objects is now expected from the next generation of astrometric satellite missions such as GAIA, proposed to ESA in the framework of its Horizons 2000 long-term scientific programme. These outstanding observational capabilities could be the key towards the solution of one of the major problems in contemporary astronomy, namely the understanding of the structure, formation and evolution of the Galaxy.

---

[8] To obtain a quantitative estimate of the impact that Hipparcos data had on astronomical research the Astrophysics Data System (e.g. `http://cdsads.u-strasbg.fr`) was searched for articles published from January 1994 (i.e. about 5 months after the end of the satellite's operations) to December 1999 containing the 'hipparcos' word in the title; 542 articles, i.e. about 90 articles/year, were found.

Table 1.1: Basic results of the Hipparcos mission. The Hipparcos, Tycho and Tycho 2 Catalogues: number of objects, astrometric and photometric accuracy, multiplicity and variability information from ESA 1997a (Hipparcos and Tycho) and Høg et al. 2000a (Tycho 2).

Hipparcos Catalogue	
Entries	118 218
Mean Star Density	$\simeq 3$ stars/deg^2
Limiting Magnitude	$V \simeq 12.4$ mag
Completeness	$V \simeq 7.3$–9.0 mag
Median Precision of Positions (J1991.25) for $Hp < 9$	0.77 mas in RA
	0.64 mas in Dec
Median Precision of Proper Motions for $Hp < 9$	0.88 mas/yr in RA
	0.74 mas/yr in Dec
Median Precision of Parallaxes for $Hp < 9$	0.97 mas
Parallaxes determinaed to better than 10%	20 853
Parallaxes determinaed to better than 20%	49 399
Systematic Errors in Astrometry	< 0.1 mas
Solved Double or Multiple Systems	12 195 (2 996 new)
Median Photometric Precision in Hp for $Hp < 9$	0.0015 mag
Periodic Variables	2 712 (970 new)
Tycho Catalogue	
Entries	1 058 332
Mean Star Density	$\simeq 25$ stars/deg^2
Limiting Magnitude	$V_T \simeq 11.5$ mag
Completeness	$V_T \simeq 10.5$ mag
Median Precision of Positions (J1991.25) for $V_T < 9$ mag	7 mas
Median Precision of Positions (J1991.25) for All Stars	25 mas
Systematic Errors in Astrometry	< 1 mas
Median Photometric Precision for $V_T < 9$ mag	0.014 mag in B_T
	0.012 mag in V_T
	0.019 mag in $B_T - V_T$
Median Photometric Precision for All Stars	0.07 mag in B_T
	0.06 mag in V_T
	0.10 mag in $B_T - V_T$
Tycho-2 Catalogue	
Entries	2 529 913
Mean Star Density	$\simeq 60$ stars/deg^2
Limiting Magnitude	$V \simeq 12.4$ mag
Completeness to 99%	$V \simeq 11.0$ mag
Completeness to 90%	$V \simeq 11.5$ mag
Median Precision of Positions (J2000.0) for $Hp < 9$	7 mas
Median Precision of Positions (J2000.0) for All Stars	60 mas
Median Precision of Proper Motions for All Stars	2.5 mas/yr
Systematic Errors in Positions	< 0.1 mas
Systematic Errors in Proper Motions	< 0.5 mas/yr

1.3 The Birth and Development of the GAIA Concept

The dramatic success of the Hipparcos mission and the lessons that had been learned from this first dedicated astrometric satellite made the idea of a more ambitious but conceptually similar astrometric satellite mission very popular within ESA, which had a great interest in maintaining the European leadership in this research area.

During the satellite operations already, the Hipparcos community started to discuss the critical issues involved in the design of such a mission, aimed at fully exploiting the astrophysical significance of extremely accurate astrometric observations performed on a large sample of the Galactic stellar population. As a result of this process, in 1993 two astrometric mission proposals, under the name of ROEMER (later ROEMER+) and GAIA, were made within ESA. Both retained the proven Hipparcos-like concept of a scanning satellite performing multi-epoch and multi-color observations along (at least) two lines of sight, and benefitted from technological advances such as Charge Coupled Devices (CCDs). The main difference between the two proposals was the chosen optical configuration. The ROEMER+ (Høg 1995) optical system consisted of two Baker-Schmidt telescopes, each producing a direct image on the focal plane, whereas GAIA's (Lindegren and Perryman 1995) consisted of three Fizeau-type interferometers. Although more challenging from a technological point of view, the interferometric option had been recommended by ESA survey committee for the Horizon 2000+ plan, in consideration of interferometry's future prospects for space applications, and it thus seemed to prevail in the community (Lindegren and Perryman 1996). However, it was later recognized that a more conservative approach was desirable, and the interferometric option was accordingly discarded in favour of direct imaging[9] . At the same time, the accommodation of an instrument for radial velocity measurements on the satellite was proposed as well, in order to create a six-dimensional phase-space map of the Galaxy, and thus greatly enhance the scientific case of the mission.

In early 1997 ESA established a Science Advisory Group (SAG) for the GAIA mission, whose function was to coordinate the preparation of a detailed Study Report on the mission, which would have formed the basis of the selection process by ESA. The SAG monitored the Concept and Technology Study (CTS) that was carried out for ESA by Matra Marconi Space from September 1997 to January 1999 in order to establish a mission design that satisfied the scientific requirements under given budgetary constraints and to identify the necessary technological developments and space qualifications. The interferometric option was pursued in a separate study carried out by Alenia Aerospazio as part of ESA technological research programme.

The Study Report on all scientific, technological and financial aspects of the mission

---

[9] GAIA was the Greek goddess of Earth worshipped as the universal mother who had created the Universe. More recently her name was taken by James Lovelock for his theory on the interdependency of the Earth's biosphere and biological organisms. It is therefore perhaps appropriate that it is now the name given to an ambitious project to unravel the structure, origin and evolution of such a complex entity as our Galaxy. Unfortunately the original meaning of the GAIA acronym, "Global Astrometric Interferometer for Astrophysics", explicitly referred to the interferometric option, so that the mission currently lacks an "official" name.

is due to ESA in summer 2000 (ESA 2000). The selection of the Horizons 2000 Corner-stone 5 mission is now expected by ESA in September 2000. If selected GAIA could be launched in 2009.

1.4 GAIA and the Near Future of Space Astrometry

We now live in what may be called the Golden Age of Space Astronomy. Many space-craft are being launched every year, and most of these provide us with the deepest and highest-resolution images ever, thus allowing the investigation in greater detail of long-standing problems and the discovery of completely new phenomena. Even if, due to budgetary reasons, the majority of astronomical observations will still be carried out from the ground, the future prospects of space astronomy are very bright, since the development of new kinds of space telescopes is underway. In particular, even if conventional imaging and spectroscopic telescopes will still play an important role, the launch of interferometric telescopes is likely to prove the most significant achievement of observational astronomy in the next twenty years or so.

As for astrometry, some tasks could be performed with large space telescopes like the HST, but most will require, if only for the premium on HST-like telescopes' observing time, a smaller dedicated satellite. The missions that are currently being planned for the near future show a keen interest in both imaging and interferometric telescopes. For instance, NASA has already approved two astrometric missions, FAME and SIM, whose launch is expected around the middle of the upcoming decade. FAME is an imaging mission, namely a small Hipparcos-like scanning satellite superposing the images from two fields of view on a CCD-covered focal plane, and will perform an all-sky astrometric and 4-color photometric survey of the 40 million brightest stars. On the other hand, SIM will be the first space mission to make use of optical interferometry, and its main goal is to perform astonishingly accurate astrometric observations, at the level of 3 μas, for 20 000 objects as faint as $V = 20$ mag. These two missions are remarkably complementary in both design and scientific goals, and illustrate the twofold need of modern observational astronomers: small datasets of superb accuracy and large, uniform databases of somewhat lower accuracy. In its present design, the GAIA mission would satisfy, at least to a certain degree, both these demands with an astrometric, photometric and spectroscopic all-sky survey of the highest accuracy. In Table 1.2, GAIA performance is compared to that of the other mentioned missions. Note that the astrometric accuracy is a strong function of the observed object's magnitude, and that only the accuracy at the limiting magnitude is given here for all missions, while the accuracy expected for GAIA at different magnitudes is given in Section 2.7. Figure 1.1 illustrates the history of astrometric accuracy from Hipparchus to GAIA. The dramatic potential of space observations is shown by the jump in accuracy achieved by Hipparcos over ground-based observations and the still greater progress achievable by GAIA with respect to Hipparcos.

Table 1.2: GAIA measurement capabilities with respect to Hipparcos and future astrometric missions approved to date. Name of the mission, funding space agency, expected year of launch, expected limiting magnitude in the V band, total number of observed stars and astrometric accuracy at the limiting magnitude expressed in mas. USNO stands for the United States Naval Observatory . See text for details about the quoted accuracy.

Mission	Agency	Launch	V_{lim}	Stars	Accuracy at V_{lim}
Hipparcos	ESA	1989	12	120 000	2
FAME	USNO/NASA	2004	15	40 million	0.220
SIM	NASA	2005	20	> 20 000	0.003
GAIA	ESA	2009	20	> 1 billion	0.200
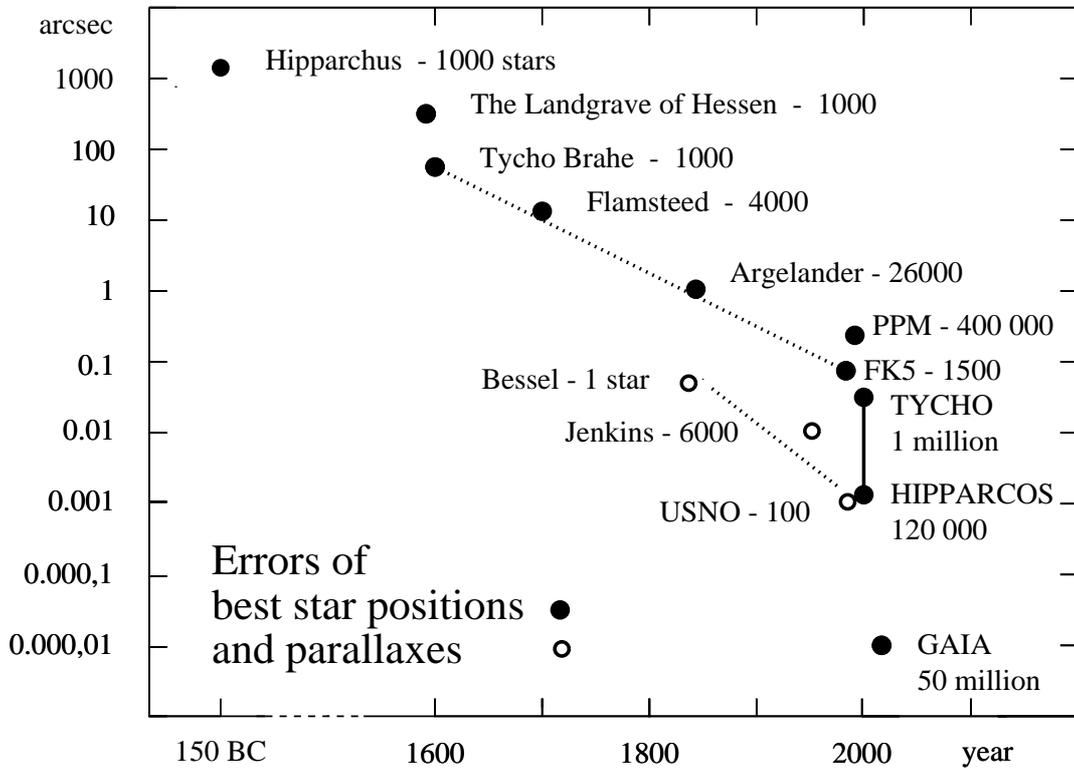
Figure 1.1: Errors of best star positions and parallaxes in history. Accuracy and number of measured stars are indicated. A conservative number of 50 million stars at an accuracy of 10 μas is here indicated for GAIA for both positions and parallaxes, but the number of measured stars at this level of accuracy may be substantially larger (see Table 2.2). Courtesy of Erik Høg, Copenhagen University Observatory.

Chapter 2

The GAIA Mission Design

The GAIA mission has been designed to solve one of the most difficult, yet deeply fundamental challenges in modern astronomy: to understand the structure, formation and evolution of our Galaxy. The basic requirement in order to achieve this goal is that of obtaining extraordinarily accurate three-dimensional positions and velocities as well as colors in several bands for a significant sample of the Galaxy's stars. The current mission design (Gilmore et al. 1998, Mérat et al. 1999, Straižys 1999 and ESA 2000), which was essentially established during the Concept and Technology Study carried out for ESA by Matra Marconi Space, not only fully meets this requirement but also promises to yield a wide range of "by-products" of fundamental scientific relevance in their own right. Even if it will be subject to further optimization in the near future, in its present form already the mission design comprises a detailed description of all relevant aspects, including spacecraft, payload and satellite operations.

2.1 The Measurement Principle and the Scanning Law

The main objective of the GAIA mission is to perform global or wide field astrometry as opposed to local or narrow field astrometry. In local astrometry a star's position can only be measured with respect to neighbouring stars in the same field. Even with an accurate instrument, the errors become prohibitive when making a survey, due to the need of combining measurements obtained in different fields, and thus affected by systematic and accidental errors. The principle of global astrometry, is instead to link stars with large angular distances in a network where each star is connected to a large number of other stars in every direction. In order to do so, the measurement of large angular distances through the simultaneous observation of two fields of view separated by a large angle is required.

This principle, first demonstrated by the success of the Hipparcos mission, can be exemplified by the problems encountered in the measurement of stellar parallaxes as it can be obtained with narrow-field instruments, illustrated in Figure 2.1. These are usually based on the measurement of the motion of a star S with respect to a number of background stars near to S on the sky, which are themselves in parallactic motion. The

relation between the relative parallax $\pi_{rel} = (\phi_2 - \phi_1)/2$ of S with respect to a generic background star S_0 and the absolute parallax of S π_{abs} is then $\pi_{abs} = \pi_{rel} + \pi_0$, where π_0 is the absolute parallax of S_0. In practice, one has to estimate the average absolute parallax of the background stars, and this estimation introduces an error that usually dominates the global error budget. This limitation presently does not allow to measure parallaxes with an accuracy better than about a few mas. In wide-field astrometry, instead, the measurement of large angular distances allows one to measure the absolute parallax $\pi_{abs} = (\phi_2 - \phi_1)/2$ of a star without the need to apply poorly determined correction factors, and the accuracy can thus be improved by orders of magnitude.

Narrow–Field Astrometry
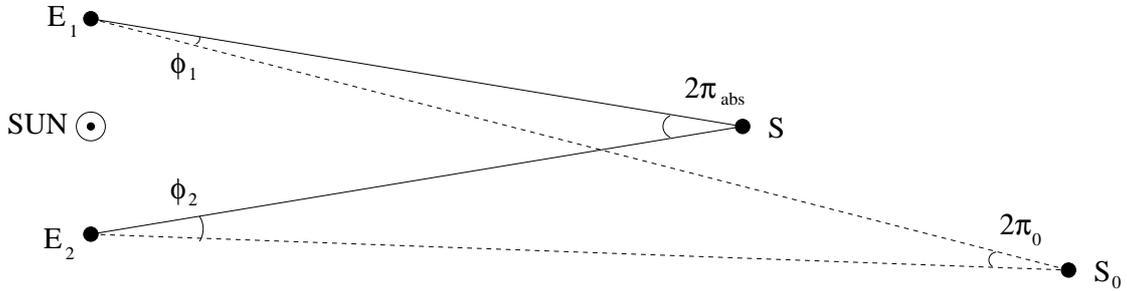
Wide–Field Astrometry
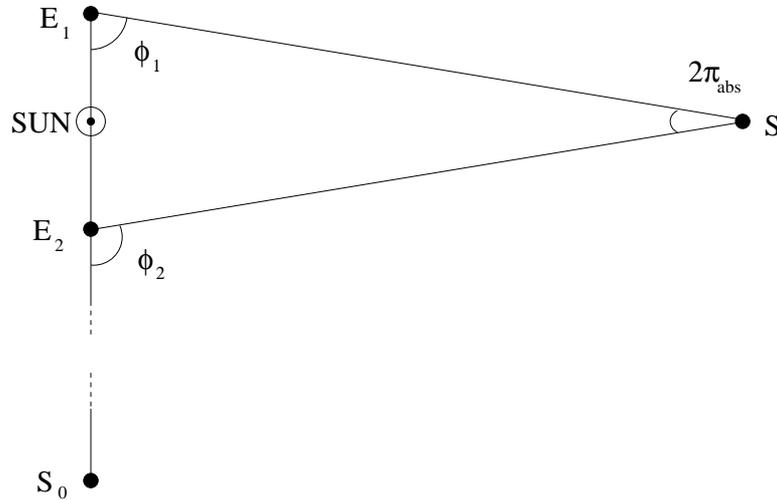
Figure 2.1: Narrow-field and wide-field astrometry. In narrow-field astrometry the measurement of the parallax of a star S involves the application of a poorly determined correction to the observed value to take into account the parallactic motion of background stars such as S_0, whereas in wide-field astrometry one can directly measure absolute parallaxes, thus obtaining a much better accuracy.

Accordingly, the GAIA payload must therefore provide two lines of sight, which can be obtained either with a single telescope and a beam combiner, as in Hipparcos, or with two separate telescopes. In either case, an high stability and an accurate knowledge of the variations of the basic angle between the two lines of sight is required in order to calibrate the astrometric measurements. The beam combiner option, however, leads to severe opto-mechanical problems for large-aperture (say above one meter or so) telescopes. Besides, the superposition of two fields of view onto a single focal plane causes crowding and object confusion on the focal plane, which become appreciable when observing faint objects. Therefore, the two-telescope concept was retained for the GAIA design and later refined with the inclusion of a third spectrometric telescope.
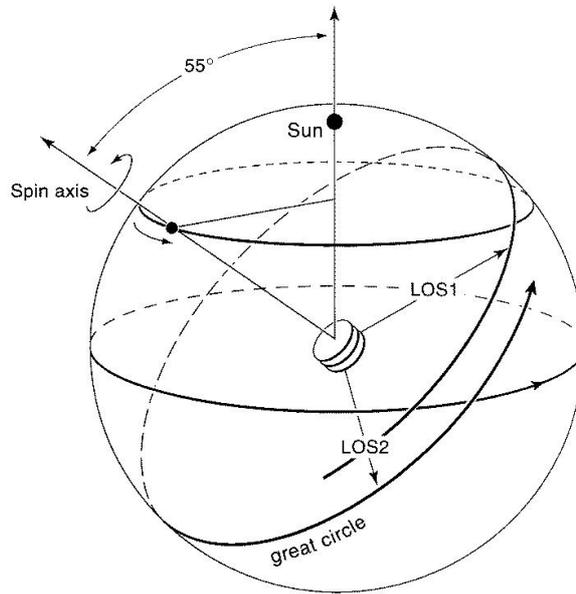
Figure 2.2: GAIA scanning law. The satellite spin and Sun axes at an angle of 55 deg are indicated, together with the lines of sight of the two astrometric instruments and two consecutive great circles. The satellite spin period is of about 3 hours, and the corresponding scanning speed is thus of 120 arcsec/s.

For a continuous accurate calibration of the basic angle, the two astrometric lines of sight must point to the same sky regions at small time intervals. This is achieved by means of an axisymmetric payload and a three-hour period (i.e. 120 arcsec/s) spin motion of the satellite about its symmetry axis, which is perpendicular to the instruments' lines of sight. From the instruments' standpoint, the stars thus cross each field of view with a uniform motion. As for Hipparcos, the scan direction is a privileged one, and the position measurements are essentially performed in this direction only. The complete and uniform sky coverage that is needed to build the star network is then obtained through a slow precession of the spin axis about the Sun axis. The angle between these two axes, or Sun angle, is thus kept constant, in order to minimize the thermal gradients

in the payload. For GAIA, the optimization of the scanning law has led to a un angle of 55 deg (43 deg for Hipparcos) and a precession period of 72 days (57 days for Hipparcos). This scanning law ensures that each sky region is observed several times during the whole mission with nearly isotropic orientations of the scanning directions. The slow precession of the spin axis generates a line of sight motion across scan of 0.51 deg over a spin period, while the field of view height is 0.68 deg. The overlapping between consecutive scans allows the calibration of some instrumental parameters such as the basic angle using the same stars. The GAIA scanning law is illustrated in Figure 2.2, while its typical sky coverage pattern is exemplified by the actual scanning of the Hipparcos satellite over a short period shown in Figure 2.3.
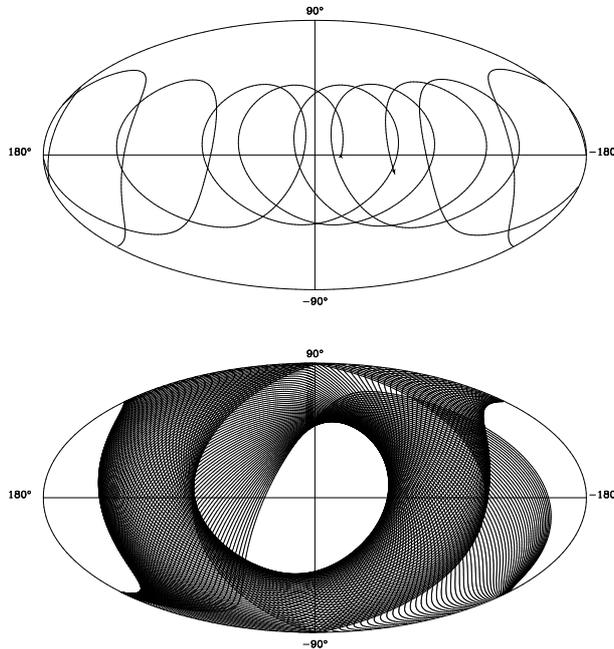
Figure 2.3: GAIA/Hipparcos sky coverage. The top figure shows the path of Hipparcos spin axis over a four-month period. The scan direction is indicated by the arrows. The bottom figure shows the actual scanning by Hipparcos during one complete precession of the spin axis (57 days). For clarity, only one reference great circle out of five is indicated. The actual scanning is five times denser.

The apparent peculiarity of the adopted observation strategy draws a sharp distinction between scanning satellites like GAIA and conventional "point-and-stare" space observatories such as the HST. The distinction is fairly similar to the one existing between conventional ground-based telescopes and meridian circles, i.e. the telescopes that are typically used for ground-based astrometric measurements. Like meridian circles, GAIA will only detect relatively bright stars, due to the short exposure times that are allowed by a continuously scanning instrument. Unlike meridian circles, however, GAIA will be able to combine many observations of any sky region, obtained at different epochs

and at different position angles, so as to significantly raise the all-mission signal-to-noise ratio. The number of observations of a given sky region mainly depends on its ecliptic latitude, owing to the fact that the chosen scanning pattern is symmetrical with respect to the Sun-satellite direction. The number of observations of 5000 random sky regions by both astrometric instruments is given as a function of the ecliptic latitude for a 5-year mission in Figure 2.4. The maximum, average and minimum number of observations are about 420, 170 and 100 (i.e. 210, 85 and 50 per astrometric instrument), respectively, where the latter value is obtained for sky regions near the ecliptic.
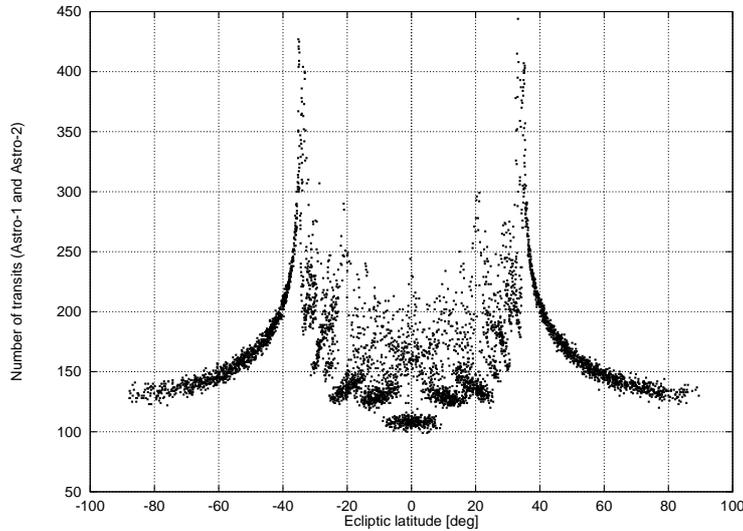
Figure 2.4: Number of observations of 5000 random sky regions by both astrometric instruments over a 5-year mission as function of ecliptic latitude. The average number of observations is 170. Courtesy of Lennart Lindegren, Lund Observatory.

2.2 The Spacecraft

The design of the GAIA spacecraft (Figure 2.5) was essentially driven by the adopted scanning law and by the requirement of a high thermal and mechanical stability. Additional constraints were posed by the expected budget and by the recommended use of the ESA Ariane V launcher for the satellite's insertion into orbit. Its fundamental characteristics are passive thermal control system, high level of thermo-mechanical separation between the payload and service modules, and monolithic payload module made of a high-performance material. The diameter and height of the spacecraft are 4.5 m and 3.1 m, respectively. Its dry mass is about 2 000 kg, which, with about 1 000 kg of propellant, gives a launch mass of about 3 000 kg.
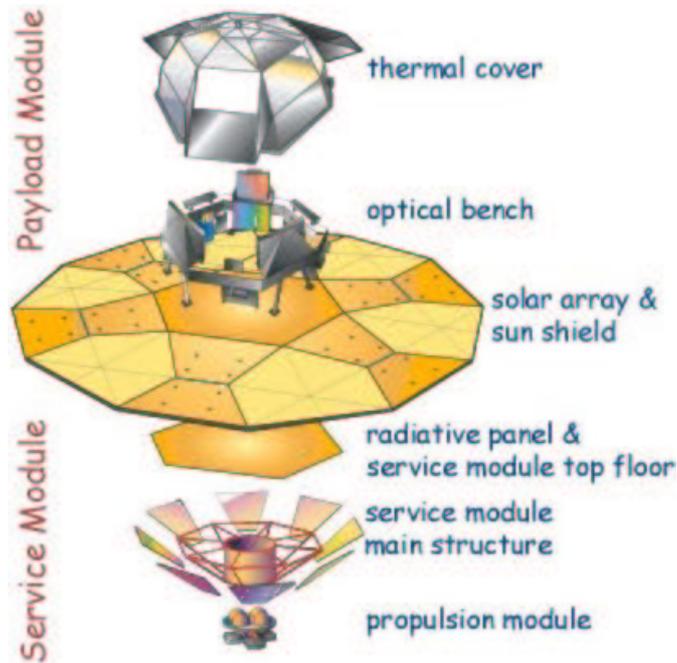
Figure 2.5: An exploded view of GAIA spacecraft. The whole spacecraft spins as a single structure around the symmetry axis (vertical in this view). This arrangement, in combination with the adopted scanning law, provides the required thermal and mechanical stability.

2.3   The Service Module

The service module has a conical shape in order to minimize turning shadows and thus thermal gradients. The propulsion system is located at the cone's apex, while the solar array and sun-shield assembly is at its basis.

The service module structure is made of aluminium and interfaces with the Ariane V adapter on one side and with the payload module on the other side. All units accommodated into the module are thermally coupled to the six lateral panels of the module, which are used as radiators and covered with optical solar reflectors.

The function of the solar array and sun-shield assembly is to protect the payload from heating and sunlight, while exploiting the solar radiant energy for the satellite power supply. It consists of six deployable solar panels which during launch are stowed against the lateral panels. The solar panels are connected by thermal foils that are spread between them, so as to provide a nearly-circular 9.5 m diameter sun-shield, whose rear face is covered by thermally insulating sheets.

2.4 The Payload Module

Although fixed or slowly variable biases are self-calibrated in the data reduction, variations at a frequency higher than or equal to the spin frequency cannot be corrected. It is therefore mandatory that the design ensures a basic angle stability (or at least a knowledge of the basic angle variations) at a level significantly below the nominal accuracy over the spin period of 3 hours. This stringent requirement is met by the present design, (Figure 2.6), which considers a monolithic toroidal structure entirely made of Silicon Carbide (SiC), a low-expansion, high-conductivity and homogeneous material. These qualities minimize the mechanical flexure and thermal expansion experienced by the truss structure, the mirrors and the detectors during the mission.
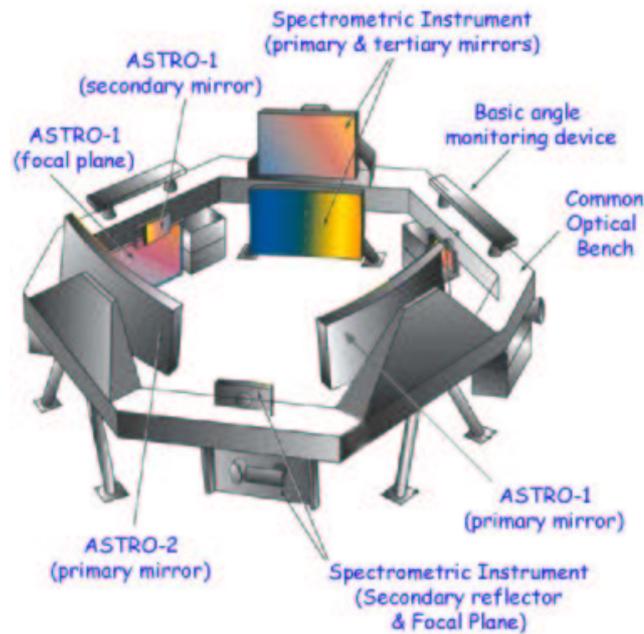
Figure 2.6: GAIA pay-load module. The two astrometric instruments and the spectrometric instrument are indicated.

The payload module is radiatively and conductively decoupled from the sun-shield by means of a thermal cover screening the whole module. Baffles and further covers are applied on the instruments' apertures, the latter being removed once in orbit. The payload temperature is thus passively stabilized at about 200 K. The payload module is also mechanically decoupled from the service module by releasing in orbit two of the three bipods connecting the two modules. A device was also designed for continuosly monitoring the basic angle variations with an accuracy better than 1 μm rms and therefore guaranteeing the payload performance. It basically consists of a laser source illuminating simultaneously the two astrometric telescopes.

The three instruments are mounted on this axisymmetric structure with their lines

of sight perpendicular to the satellite symmetry axis. The basic angle between the lines of sight of the two astrometric instruments is of 106 deg, while the line of sight of the spectrometric instrument lies on their axis of symmetry. The three instruments are essentially identical all-reflective telescopes. The mounting plates and mirrors are also made of SiC, and the focal planes are covered with CCDs.

Since the mission design has not been "frozen" yet, there still is some discussion about which would be the best choice for some critical instrumental parameters. This is the case e.g. for the photometric system, which will consist of a set of broad bands in the astrometric instruments and a set of medium bands in the spectrometric instrument. The choice of the photometric system to be implemented is of particular importance because the GAIA database will include such a large amount of high-accuracy information that it will be the reference for many decades. Several options are presently being discussed, differing both in the number of bands and in their response curves, and these uncertainties are reflected in the following, where only the broad-bands of the photometric system are of interest. In the description of the focal planes of the astrometric instruments, we will follow Mérat et al. 1999, who generically consider a non-specified, four-color broad-band photometric system. In the simulation of galaxy observations, instead, we will consider the five-color system originally proposed by Høg, Knude and Straižys 1999 and later variously modified, which we will hereafter refer to as the $fgriz$ system, owing to the fact that at the time of carrying out the simulations the expected photoelectron count rates were made available in this system. Finally, the broad bands of the Asiago Photometric System (Moro and Munari 2000), one of the present candidate systems, are used to illustrate how the final GAIA broad-band photometric system could look like.

2.4.1   The Astrometric Instruments

The two precisely identical astrometric instruments, or Astros, are used for astrometry and multi-color broad-band photometry, and are referred to as preceding and following astrometric instrument, or Astro-1 and Astro-2, respectively.

Each telescope is a three-mirror anastigmat featuring a rectangular aperture[1] of 1.7 m × 0.7 m = 1.49 m^2, an inter-mirror distance of about 3 m and a focal length of 50 m. The image scale on the focal plane is thus of about 4.1 arcsec/mm, while the instrument's Airy Disk is an ellipse of axes 135×325 mas^2 at $\lambda_{eff,V} \simeq 550$ nm and 195×470 mas^2 at $\lambda_{eff,I} \simeq 800$ nm. The aperture is elongated in the scan direction, so as to provide the narrowest PSF in the measurement direction while being compatible with the volume of the spacecraft and the optical quality of the mirrors. The large primary and tertiary mirrors are polished to $\lambda/30$ rms, while the smaller secondary mirrors are polished to $\lambda/50$ rms, yielding a diffraction limited performance over the whole field of view.

The focal plane of each telescope is basically a rectangular mosaic made of more than 300 of CCDs, giving a field of view of 0.80 deg × 0.68 deg $\simeq$ 0.54 deg^2. A rectangular

---

[1] Henceforth, when referring to the size of (a portion of) a surface of the instrument such as the aperture or the focal plane, $x \times y$ will indicate a size of x along scan and of y across scan.

pixel size of $9 \times 27 \ \mu m^2$ or $37.2 \times 111.6 \ mas^2$ was chosen in order to match the Airy Disk shape and thus providing an higher resolution in the scan direction. The large focal length allows a proper sampling of the diffraction pattern with about 4 pixels along scan and 3 pixels across scan covering the Airy Disk. CCDs of two different sizes are used in order to increase redundancy in some key areas of the focal plane such as the sky mapper and the overlapping regions. Smaller CCDs have a size of 2780×1075 pixels $= 25.020 \times 29.025 \ mm^2 \simeq 103 \times 120 \ arcsec^2$, while bigger CCDs are the same size along scan and twice as large across scan, giving a size of 2780×2150 pixels $= 25.020 \times 58.050 \ mm^2 \simeq 103 \times 240 \ arcsec^2$. An observed object follows a nearly horizontal line on the focal plane with a speed given by the spinning period, and therefore successively crosses all the columns of CCDs. With the 3-hour spinning period provided by the scanning law the object has an along-scan speed of 120 arcsec/s, corresponding to about 3200 pixels/s or 0.31 ms/pixel. Due to the high speed, the charges accumulated in the CCD pixels cannot be read out as it is done with conventional imaging telescopes, but a dedicated integration technique must be used. In the case of GAIA, the CCDs will be operated in Time Delay Integration (TDI), a concept introduced for an astrometric satellite by Høg 1993. The idea is to let the integration process follow the image while it is moving across the CCD. In practice, every 0.31 ms, i.e. every time the image has moved of one pixel along scan, all charges are quickly shifted by one pixel in the scan direction. The readout of the accumulated charges takes place at the serial register at the "end" of each CCD. The image is thus integrated over the entire crossing of each CCD, leading to an exposure time of about 0.86 s per CCD per scan. The main drawback of this technique is the additional smearing of the image due to the charge shift and to the slow across-scan motion of the objects, which together cause an appreciable but acceptable loss of resolution. On the other hand, the loss of resolution due to the non optimal charge transfer efficiency is expected to be negligible.

The focal plane layout is represented in Figure 2.7. The 25 columns of detectors covering the focal plane are functionally grouped in four parts: the Astrometric Sky Mapper (ASM, 4 columns), the Astrometric Field (AF, 16 columns), the Photometric Sky Mapper[2] (PSM, 1 column) and the Broad-Band Photometer (BBP, 4 columns). A thorough description of the functions fulfilled by the different parts of the focal plane is given in Section 5.1. In brief, the ASM is used for object detection, the AF for multiple multi-epoch astrometric measurements, the PSM to generate a 1 arcsec radius high-resolution map around each detected star and the BBP for multi-color and multi-epoch broad-band photometry.

The ASM, the AF and the PSM work without filters in a very broad band, having a response curve defined by the telescope transmittance and the Quantum Efficiency (QE) of the presently agreed-upon CCD, the so called CCD#1B. The resulting response curve extends in the range of wavelengths 250–1050 nm, and the zero-point of the magnitude scale, the so called G (GAIA) magnitude, is such that for most stellar types the G magnitude has a value which is intermediate between V and I. The BBP columns

---

[2] The Photometric Sky Mapper is often referred to as the last column of the Astrometric Field, but, in consideration of its different function, it was decided to clearly distinguish it in this study.

Figure 2.7: The focal plane of the astrometric instruments. The physical division in CCDs and the logical division in 4 parts of the focal plane are indicated. The nearly horizontal motion of the observed objects along scan resulting from the scanning of the satellite is illustrated. The lines between the CCDs include a small dead zone (4 mm and 500 μm along and across scan, respectively) between consecutive rows and columns. Note that the along-scan and across-scan size of the CCDs are here slightly not in scale.

work in four different broad bands defined by the product of the aforementioned global response curve and the response curve of four filters.

The $fgriz$ photometric system (Høg, Knude and Straižys 1999) adopted in this study consists of five passbands of about 100 nm width. A rectangular response and a peak transmission of 0.90 is assumed for all filters. Roughly speaking, the fgr bands closely resemble the BVR bands, while the iz bands together cover a waveband with the same center as the I band. The QE curve of the CCD#1B is shown in Figure 2.8, in which the normalized response curves for the Asiago Photometric System (Munari 1999) have been preferred for illustrative purposes to the corresponding curves for the $fgriz$ system. The specifications of the two photometric systems are given in Table 2.1.

Figure 2.8: GAIA broad-band photometric system. The absolute response curve of CCD#1B and the normalized response curves of the five broad-band filters of the Asiago Photometric System. Filter specifications taken from Moro and Munari 2000.

2.4.2 The Spectrometric Instrument

The design of the spectrometric instrument, or Spectro, is still somewhat uncertain, partly due to the fact that its inclusion in the payload was decided relatively late in the course of the mission preliminary studies and partly because, as far as spectrometry was concerned, the experience of previous space missions gave little or no help in tackling the problems posed by the continuous scanning motion of the satellite. For this reason, even if it is generally agreed that the instrument will be used for radial velocity measurements and for medium band photometry, the instrumental parameters and the instrument's general design itself are provisional and will be subject to further discussion.

According to the provisional design, the three-mirror telescope features a 0.75×0.7 m^2 aperture, a focal length of 4.17 m and a field of view of 2×1 deg^2, over which the instrument provides diffraction-limited performance. A central part of size 1×1 deg^2 of the field of view is devoted to spectroscopic radial velocity measurements

Table 2.1: Specifications of the $fgriz$ and Asiago broad-band photometric systems. The central wavelength λ_c and the bandwidth $\Delta\lambda$ are the centre and the width of the passbands for the $fgriz$ system but denote the peak and FWHM of the bands' response curves for the Asiago system. Filter specifications taken from Høg, Knude and Straižys 1999 and Moro and Munari 2000.

$fgriz$ system					
Band	f	g	r	i	z
λ_c	445	550	650	750	850
$\Delta\lambda$	110	100	100	100	100
Asiago system					
Band	$b300$	$b480$	$b630$	$b792$	$b964$
λ_c	300	480	630	792	964
$\Delta\lambda$	141.5	150	150	172	170

(Radial Velocity Spectrometer, or RVS), while the two regions making up the rest of the field are devoted to medium-band photometry in a number of bands depending on the photometric system that will finally be adopted (Medium-Band Photometer, or MBP). The first portion of the preceding region of the MBP actually works without filters (i.e. in the G band) and is used as a dedicated sky mapper to detect objects crossing the field of view and to cross-identify them with those observed by the astrometric instruments. The RVS is a slitless spectrograph consisting of a collimating lens, a disperser and an imaging lens, working at unit magnification in a symmetrical configuration. The spectrum of the object crossing the field of view is spread across scan over about 600 pixels and the radial velocity is derived from the Doppler shift of some spectral lines in the wavelength range 850–875 nm. The CCDs covering the focal plane are operated in TDI, giving an integration time per scan of 3 s per band in the MBP and 30 s per spectra in the RVS. A CCD with a QE curve shifted towards the red with respect to that used in the Astros and with a square pixel of 10 μm side, the so called CCD#2, is used in order to optimize the instrument for the wavelength range chosen for radial velocity measurements. The spectral and spatial resolution are thus about 0.4 Å/pixel and 0.5 arcsec/pixel, respectively.

2.5   The Satellite Launch, Orbit and Operations

An obvious advantage for any accurate measurement is the location of the instrument in a benign environment. Accordingly, the scientific requirements of the GAIA mission call for a very quiet operational orbit, in terms of thermo-mechanical stability as well as instrument's exposure to radiation.

The selected operational orbit is a small-extension Lissajous or Halo orbit around the L2 Lagrangian point of the Sun-Earth system, 1.5 million km from Earth, the same selected for FIRST and PLANCK and proposed for the NGST. The main characteristics of such an orbit that make it preferable with respect, e.g., to the geostationary orbit

planned for, but non achieved by, the Hipparcos satellite, are a low radiation flux due to the long distance from Earth and a stable thermal environment due to the continuous and uniform illumination from the Sun (Pace 1997). The long distance from Earth, however, severely limits the affordable data transmission rate to the ground (see Section 2.6).

The spacecraft is designed for launch by Ariane V into a standard Geostationary Transfer Orbit (GTO). The transfer from the GTO to the operational orbit is done with a 400 N engine right after the separation of the launcher. A redundant set of 10 N thrusters is used for orbit correction during the transfer phase and for the final insertion into the operational orbit. During the operations, a pointing stability better than 2 mas/s over 1 s is required in order to follow the scanning law without blurring the star image on the focal plane. This is achieved thanks to a set of Field Emission Electric Propulsion (FEEP) microthrusters with a thrust of the order of 1 mN, which are used in combination with a wide field star sensor and the sky mappers of the astrometric instruments.

The selected operational orbit and the attitude control system provide a 6 year lifetime, including 8 months for the transfer between the GTO and L2 orbit and some margin, giving at least 5 years of observation without occultations of the field of view or eclipses of the Sun, and even more than that assuming a small correction manoeuvre after a few years of operations.

2.6 Data Handling

For a space telescope the overall data handling is a very complex process requiring the control of many different aspects. This is particularly true for GAIA, since this mission will acquire data continously and at an high rate, so as to require highly automated and reliable procedures.

During the mission, two very different kinds of data are routinely acquired, processed on-board, transmitted to ground and here reduced, namely the "housekeeping" data needed for the spacecraft control and the scientific data proper. The former are obviously needed on a continuous time basis, while the latter can also be transmitted "once in a while", provided that a sufficiently large storage device is accommodated on the spacecraft and that the total amount of transmitted data at the end of the mission meets the scientific requirements.

For this reason, communication between the satellite and the Earth is done via two sets of equipment. An X-band telemetry and telecommand link with an omnidirectional coverage provides a permanent control of the spacecraft via a continuous but relatively low data rate of 6 kbit/s. A dedicated telemetry link, also in the X-band, provides the transmission of the scientific data at a much higher rate of 3 Mbit/s only when a ground station is "visible", and is complemented by a 100 Gbit solid state memory ensuring the temporary storage between two consecutive transmission periods. Since only one ground station is likely to be affordable for the mission, giving a mean visibility period of 8 hours a day, the resulting mean science data rate is of 1 Mbit/s. During the mission the satellite will therefore transmit to ground something like 20 Tbyte of data, a huge

amount of information. A special CCD reading strategy was thus developed in order to identify the CCD regions containing useful information, so as to observe as many objects as possible, the achievable telemetry rate being fixed. Such strategy is described in detail in Section 5.1. Some level of data compression, by a factor in the 2–3 range, is then performed to furtherly increase the total amount of scientific information contained in the transmitted data. It is believed that such a compression rate could be easily achieved with minimum impact on the data quality. Still, the telemetry rate presently poses the most stringent constraint on the number of objects that GAIA can observe, meaning that the nominal number of 10^9 observed objects could be made even larger if an higher telemetry rate could be achieved.

A dedicated scientific data chain includes all the units required for the acquisition, the aforementioned discrimination, the compression and the storage of the data. The raw data are then transmitted to the ground without any further processing, and are readily made available to the astronomers for the data reduction proper.

The processing of GAIA raw data into consistent sets of astrophysical data is an extremely challenging task. It is not just the amount of data that is formidable, but even more so the intricate relationships between different pieces of information gathered with the various instruments throughout the mission. A highly automated, yet sophisticated data processing system will be required to take care of the bulk reductions. At the same time, a great deal of flexibility and interaction is needed to cope with special objects or astrophysical investigations, many of which cannot be foreseen at the software design stage. On the other hand, the delicate calibration of instrumental parameters and satellite attitude, necessary to interpret the data in terms of absolute astrometric and photometric quantities, must be protected from unintentional modification. It is envisaged that an object oriented database might provide a suitable environment for the GAIA data processing. O'Mullane and Lindegren 1999 have accordingly developed a simplified model and have tested it using the Hipparcos Intermediate Astrometric Data contained in ESA 1997a. Basically, the data reduction starts with the so called great circle reduction, i.e. the processing of the data for each one-dimensional strip scanned by the satellite, which will allow to locate the objects relative to each other. Then the reduction process has to orient and phase the different great circles with respect to each other in what is called the sphere reduction. More specifically, this model follows a general scheme known as Global Iterative Solution, outlined in Chapter 23 of ESA 1997a and consisting of a cyclic sequence of three processes which are applied until convergence to four data sets, namely the CCD data, the calibration data, the sky data and the attitude data. The tested approach seems to be feasible and appropriate for the purpose of GAIA data processing.

2.7   Expected Measurement Capabilities

Roughly speaking, GAIA will observe all objects brighter than $V = 20$ in the Astrometric Instruments (astrometry and broad-band photometry) and all objects brighter than $V = 16-17$ in the Spectrometric Instrument (radial velocity measurements and medium-

band photometry). The sample that will thus be observed, almost unimaginable in size and accuracy by any previous standards, will contain a significant portion of the Galaxy's stars, including huge numbers of exotic objects sparsely represented in the solar neighbourhood, thus helping to put many fields of astronomical research on a more sound statistical basis. The final catalogue will approximately contain 340 000 objects down to $V = 10$, 26×10^6 to $V = 15$, 250×10^6 to $V = 18$ and over 10^9 to $V = 20$. The average sky density of the final catalogue at $V = 20$ will thus be about 25 000 stars/deg^2. Large numbers of peculiar objects such as solar system minor planets (1 million), extra-solar planets (30 000), supernovae (100 000) and quasars (500 000) will be detected and observed as a natural part of the main observing programme, while, a special observing strategy had to be designed for the detection and observation of about 3 million galaxies, as is described in Section 5.1.

As for the accuracy of the measured quantities, a clear distinction must be made between the epoch accuracy and the all-mission accuracy. The former is the accuracy of a measured quantity obtained from only one observation of the object, while the latter is the accuracy obtained at the end of the mission, when all the observations of the same object have been put together and all attitude, calibration and sky data are available. Actually, due to the short exposure times, single observations are obtained with a relatively low signal-to-noise ratio, and the all-mission accuracy is then about $\sqrt{N}$ times better, where N is the total number of observations. The single observation accuracy is however sufficient to determine proper motions and parallaxes from multi-epoch positions and light curves for variable stars from multi-epoch brightnesses.

From a statistical standpoint, the accuracy of both astrometric and photometric measurements is basically determined by the number of detected photons emitted by the object. As for GAIA, since the one-scan exposure time is fixed and the number of observations is approximately the same all over the sky, the main paramenter determining the all-mission astrometric and photometric accuracy is therefore the brightness of the observed object. A weaker dependence on the object's position on the sky and spectrum can then be seen, arising from the scanning law followed by the satellite and the spectral response curve of the detectors, respectively.

The all-mission astrometric accuracy averaged over the sky is given in Table 2.2 for a G2V star of different G magnitudes. On the basis of Galaxy models the accuracy of parallaxes and proper motions can be translated into relative errors on distances and tangential velocities. It is estimated that 21 million distances will be determined to better than 1 per cent, 46 million better than 2 per cent, 116 million better than 5 per cent and 220 million better than 10 per cent. As for proper motions, 44 million will be determined to better than 0.5 km/s, 85 million better than 1 km/s, 210 million better than 3 km/s, 300 million better than 5 km/s and 440 million better than 10 km/s.

Expected accuracies of epoch photometry in the G band and all-mission photometry in the $fgriz$ bands are given in Figure 2.9. Accuracies of a few hundredths of magnitude are expected for stars of most spectral types of $G \simeq 18$. When combined with the medium-band photometric measurements performed by the spectrometric instrument, paramenters such as the spectral class, effective temperature, surface gravity, metallicity, interstellar extinction and color excess will be determined for most observed objects.

Table 2.2: GAIA all-mission astrometric accuracy. Median all-mission accuracy of positions, proper motions and parallaxes at different G magnitudes for a G2V star from a 5 year mission. The median value is calculated over uniformly distributed sky regions.

G	mag	10	11	12	13	14	15	16	17	18	19	20	21
Position	μas	3	3	3	4	6	9	15	23	39	70	140	440
Proper Motion	μas/yr	3	3	3	4	5	8	13	20	34	60	120	380
Parallax	μas	4	4	4	5	7	11	17	27	45	80	160	500

Distances and absolute magnitudes of objects whose parallax is too small to be measured astrometrically will also be obtained from photometric measurements.

The accuracy of radial velocity measurements is expected to be in the 1-10 km/s range, the former value being achieved for stars brighter than $V \simeq 15$ and the latter for stars of $V \simeq 17$.

2.8   Overall Scientific Objectives

Since its conception, the main scientific goal of the GAIA mission was a better understanding of the structure, formation and evolution of the Galaxy we live in. During the mission design phase, however, it was realized that its scientific potential was substantially more far-reaching. According to the extensive mission preliminary studies, all branches of astrophysics will greatly benefit from the immense quantity of extremely accurate data provided by GAIA.

Current understanding of the physics of individual stars will be revolutionized. Very accurate data covering the whole Hertzsprung-Russell diagram, from pre-main sequence to stellar death, will be available even for short-lived stellar evolutionary phases, not only for single stars but also for large numbers of binary and multiple systems. The spatial distribution of dark matter within the Galaxy will be determined. A census of the minor bodies in the Solar System, together with measurements of the number of planets around stars as a function of spectral type, will quantify planetary system formation modeling, and optimize the search for extra-trerrestrial life. A large, well-defined all-sky catalogue of galaxies and quasars will quantify studies of the structure of the local universe and of much larger scale structures at high redshift. The stars, galaxies, active galactic nuclei and quasars mapped by GAIA are the natural complement to surveys at other wavelengths, from ground-based radio observations to space-based high-energy measurements. Fundamental physics will benefit from local metric mapping, which will test general relativity to unprecedented accuracy. More specifically, the scientific topics that will be addressed by GAIA include (Gilmore et al. 1998, Straižys 1999 and ESA 2000):

- **Galactic Astrophysics**: origin and history of our Galaxy — tests of hierarchical structure formation theories — star formation history — chemical evolution — inner bulge–bar dynamics — disk–halo interactions — dynamical evolution — nature of the warp — star cluster disruption — dynamics of spiral structure —
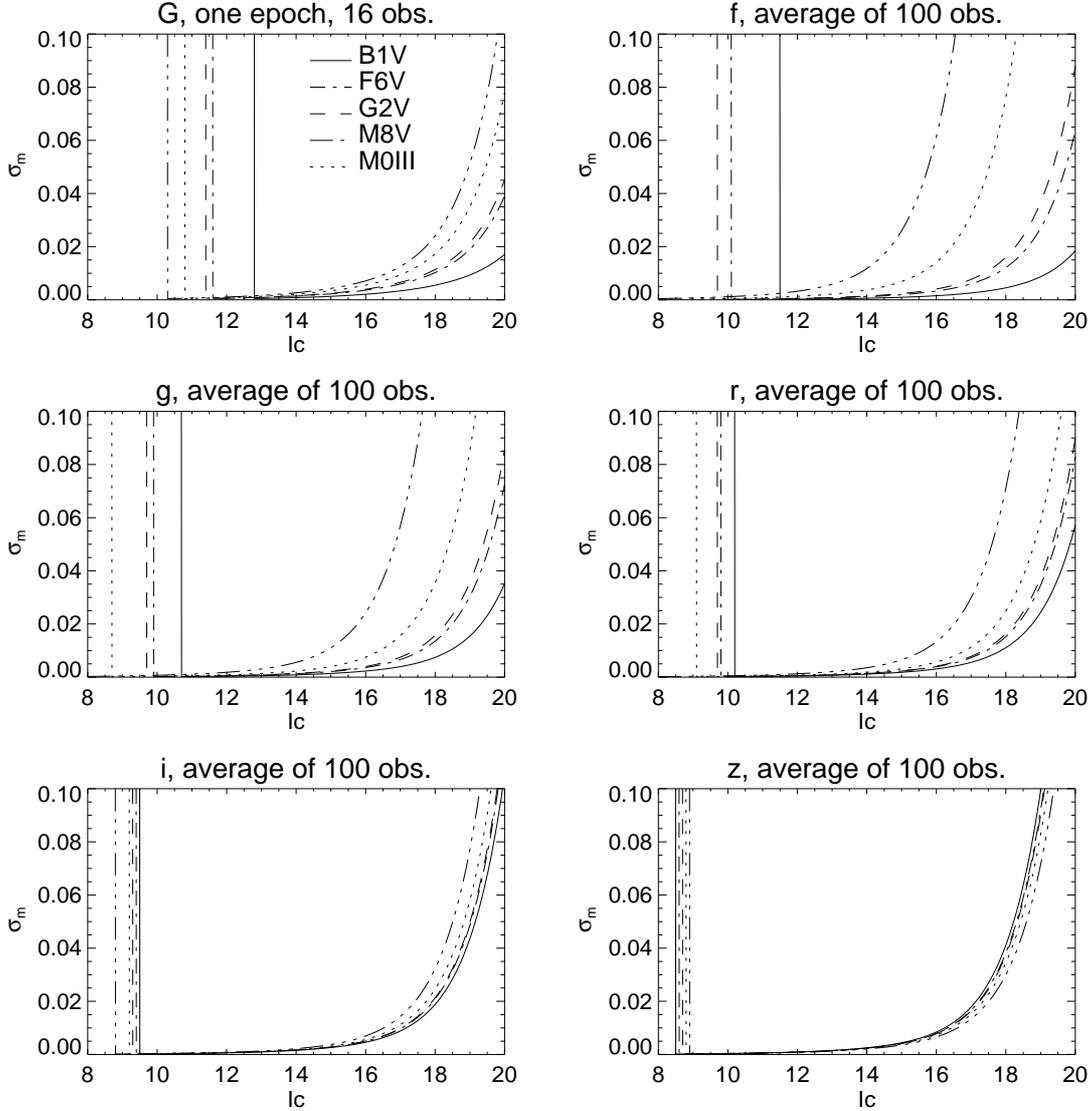
Figure 2.9: GAIA broad-band photometric precision. Median expected broad-band photometric precision for stars of different spectral types as function of I_C magnitude. Single-scan precision in the very broad G band and 100-scan precision in the five broad $fgriz$ bands. An extinction of $A_V = 0$ was assumed. Vertical lines indicate saturation of the CCD at bright stars. The quoted figures are for the Astro-1. For the Astro-2 the photometric performance is expected to be the same for bright stars and slightly better for faint stars, due to a different CCD binning (see Section 5.1). From Høg, Fabricius, Knude and Makarov 1999.

distribution of dust — distribution of dark matter — detection of tidally disrupted debris — Galaxy rotation curve — disk mass profile

- **Stellar Astrophyiscs**: *in situ* luminosity function — dynamics of star forming regions — luminosity function for pre-main sequence stars — detection and categorization of rapid evolutionary phases — complete and detailed local census down to single brown dwarfs — identification and dating of oldest halo white dwarfs — age census — census of binary and multiple stars —

- **Distance Scale and Reference Frame**: parallax calibration of all distance scale indicators — absolute luminosities of Cepheids — distance to the Magellanic Clouds — definition of the local, kinematically non-rotating metric

- **Local Group and Beyond**: rotational parallaxes for Local Group galaxies — kinematical separation of stellar populations — galaxy orbits and cosmological history — zero proper motion quasar survey — cosmological acceleration of the Solar System — surface photometry of galaxies — detection of supernovae

- **Solar System**: deep and uniform detection of minor planets — taxonomy and evolution — inner Trojans — Kuiper Belt objects — disruption of Oort Cloud

- **Extra-Solar Planetary Systems**: complete local census of large planets to 200–500 pc — orbital characteristics of several thousand systems

- **Fundamental Physics**: γ to 5×10^{-7} — β to $3 \times 10^{-4} - 3 \times 10^{-5}$ — solar J_2 to $10^{-7} - 10^{-8}$ — $\dot{G}/G$ to $10^{-12} - 10^{-13}$/yr — constraints on gravitational wave energy for $10^{-12} - 4 \times 10^{-9}$ — constraints on Ω_M and Ω_Λ from quasar microlensing

Throughout the history of science, substantial enhancements of the measurement capabilities have always brought to the discovery of unpredicted phenomena. GAIA will provide multi-epoch astrometric, photometric and spectroscopic measurements of objects ranging from solar system objects to quasars, thus constructing the first all-sky phase-space map of the Galaxy as well as probing the large-scale structure of the low and high redshift universe. Further scientific results whose nature and importance cannot be foreseen are therefore to be expected. As Galileo wrote, "if they could have seen what we now see, they would judge how we judge".

Chapter 3

Scientific Case for Galaxy Observations with GAIA

As we saw in the previous Chapter, the GAIA mission was essentially conceived with the purpose of precisely measuring star positions in order to disentangle the stars' parallactic and proper motions. Consequently. the mission design resulting from the preliminary studies, and whose main features are a continuous, relatively quick rotation of the satellite (i.e. short single-scan exposure times) and rectangular telescope apertures (i.e. elliptical Airy Disks), is certainly more suitable for the accurate centroiding of point-like sources than for two-dimensional morphological studies of diffuse sources.

Still, as soon as the mission design was firmly established, it was realized that the scientific case for two-dimensional observations of high-surface brightness regions with GAIA was potentially dramatic. Although such an idea came up relatively late in the course of the misssion feasibility studies, it was soon integrated in the mission baseline design under the name of GAIA Galaxy Survey.

Accurate positional measurements and high-resolution, multi-color photometric observations of the inner regions of about 3 million galaxies are unique datasets GAIA could provide with only a minimum effort in terms of mission design and telemetry. Owing to the late inclusion of galaxy observations in the mission design, it has not yet been possible to consider in detail the wide-ranging scientific objectives that could thus be addressed, and the objectives that are here briefly mentioned are therefore to be considered a minimum.

3.1   Galactic and Extragalactic Astronomy

The planet we live on is located towards the outskirts of the Milky Way, a gravitationally-bound conglomeration of stars, gas and dust, or galaxy, similar to countless other such systems observed on the sky. These systems, in turn, are arranged into bound clusters and still larger structures, but it is the galaxies themselves, due to their being physically and dynamically isolated systems, except for occasional collisions and mergers with other galaxies, that are usually regarded as the fundamental building blocks of the Universe.

The dramatic sight of a diffuse stream of light stretching across the sky has intrigued people since ancient times, the Greeks and the Romans already suggestively referring to it as the Milky Way. It was only in 1610, however, that Galileo's first spyglass observations produced evidence that our Galaxy is in fact a swarm of faint stars which cannot be resolved with the naked eye. Faint, diffuse, almost elliptical objects have been known ever since under the name of *nebulae*, but until well into the twentieth century there has been no general agreement about their nature. This was mainly due to the long-standing confusion between the Galactic clouds of ionized gas and the external galaxies, two classes of objects that could only be clearly distinguished through either accurate distance measurements or spectroscopic observations. Owing to the difficulties in carrying out such observations at the required level of accuracy, and even though the hyphotesis that the nebulae are in fact separate "island universes" has been put forward in the eighteenth century already by Immanuel Kant, until the 1920s it was by no means clear that any objects existed beyond the boundaries of the Milky Way.

The clinching observation came in 1922, when Edwin Hubble, using the superior optics of the recently-completed 100-inch telescope at Mount Wilson, managed to resolve a few nearby nebulae into stars and established that the brightnesses of a few of those seen in M31 varied in the characteristic periodic manner of Cepheid variables. Using the already-established period-luminosity relation characterizing these stars, he was able to estimate the distance to M31, firmly demonstrating that it was not an element of the Milky Way but a comparable stellar system in its own right, and thus marking the birth of extragalactic astronomy. Since then, Galactic and extragalactic astronomy have been remarkably complementary research fields, and though each has developed its own characteristic methods, the degree to which they have influenced each other cannot be overestimated. Generally speaking, small-scale phenomena are best observed within our Galaxy, where they are sufficiently nearby to be seen clearly. Large-scale galactic structures, on the other hand, are often best observed in external galaxies where we have a clear perspective on the whole system. One of the future major steps towards the understanding of Galactic structure, formation and evolution, the GAIA mission will further demonstrate this principle by significantly contributing to extragalctic astronomy as well through observations of large samples of objects such as stars belonging to Local Group galaxies, nearby galaxies and quasars.

3.2   Galaxy Surface Photometry

Galaxies are very complex objects whose structure, formation and evolution are far from completely understood. An essential step towards putting the study of galaxies on a quantitative basis is the measurement of their surface brightness distribution. This is a particularly difficult undertaking for several reasons, but mainly because the detector response is not perfectly uniform over the focal plane, because the sky over which galaxies are observed is never completely dark and because, particularly in ground-based telescopes, the image of a point-like source which is formed on the telescope focal plane is a spot of relatively large size.

3.2.1 Flat-Fielding

The first step in the reduction of galaxy surface photometry, the *Flat-Fielding* is the correction of errors introduced by differences in sensitivity between different regions of the focal plane. These are essentially due to two effects, namely differences in the intrinsic sensitivity of the detector elements, e.g. the pixels of a CCD, and to dimming of images towards the edge of the field of view. The errors arising from this correction usually dominate the final error budget, e.g. in HST observations, but in the case of GAIA they are expected to be negligible, at least as far as the mission average measurements are concerned. This is because the superposition of measurements obtained from a large number of scans at different positions and position angles will effectively average over any non-uniformities, thus reducing the flat-fielding errors to negligible levels.

3.2.2 Sky Background

Even when the surface brightness contributed by the Sun and the Moon are not taken into account, the sky is never completely dark. One then has to subtract this contribution from the surface brightness measured in each region of the sky in order to derive the surface brightness contributed by the foreground object. In the optical region, the surface brightness of the moonless night sky, or *Sky Background*, results from several contributions, the most important of which are:

- The *Air Glow*, produced by photochemical processes that take place in the upper atmosphere. This component is characterized by irregular variations in the intensity and in the spectrum on short space and time scales, but generally is stronger at long wavelengths and increases with latitude. Clearly, this component is relevant for ground-based or Low-Earth-Orbit observations only.

- The *Zodiacal Light*, due to interplanetary matter, through scattering of sunlight and thermal emission by dust particles and line emissions by gas atoms.

- The *Integrated Starlight*, due to faint stars not individually accounted for.

- The *Diffuse Galactic Light*, due to interstellar matter, through scattering of starlight and thermal emission by dust particles and line emissions by gas atoms.

- The *Diffuse Extragalactic Light*, due to external galaxies that are not individually accounted for.

The total sky background, as well as the relative importance of its various components, vary greatly with wavelength, with time, with Galactic and ecliptic coordinates and from observatory to observatory. Leinert et al. 1998 give a detailed account of the values of the sky background over a wide range of wavelengths, from the far ultraviolet to the far infrared. Generally, zodiacal light is the greatest contribution, followed by air glow, integrated starlight, diffuse Galactic light and diffuse extragalactic light. Table 3.1 gives typical values for the sky background as observed from the ground in the $UBVRI$ bands.

Table 3.1: Typical values of the sky background as seen from the ground in the $UBVRI$ bands. Surface brightness values expressed in mag/arcsec^2. From Binney and Merrifield 1998.

μ_U	μ_B	μ_V	μ_R	μ_I
22.0	22.7	21.8	20.9	19.9

If seen from above the atmosphere, the sky background is fainter by a factor depending on the waveband. In the V band this factor can be as large as 1.5 mag, and still larger factors can apply at longer wavelengths. Specifically, Gilmore 1997 has provided values of the sky background obtained excluding stars from some low Galactic and ecliptic latitude HST WFPC2 images. These values are listed in Table 3.2, and are believed to overestimate the typical sky background.

Table 3.2: Typical values of the sky background as seen from space in the BVI bands. Values are actually given in the HST bands F450W, F606W and F814W, closely resembling the BVI standard magnitudes (see Holtzman et al. 1995b). 1 σ random errors, derived from measurements at many different parts of the field, are of about 0.05 mag/arcsec^2. From Gilmore 1997.

μ_B (F450W)	μ_V (F606W)	μ_I (F814W)
22.87	22.06	21.46

Note, however, that the sky background as measured by GAIA will be slightly brighter, due to unresolved objects, an effect which can conservatively be taken into account by increasing the values given in Table 3.2 by 0.5 mag. Note also that the real sky can be much brighter, due to scans through the Moon, bright planets, Galactic nebulae and very crowded regions. All such special cases need to be considered individually. In the following, specifically in Chapter 5, we will accordingly assume an I-band sky background of $\mu_{bg,I} = 21.0$ mag/arcsec^2. Note that, in this context, the corrections to be applied for the conversion between HST WFPC2 magnitudes and standard $UBVRI$ magnitudes, which in principle could be carried out using the HST WFPC2 calibration by Holtzman et al. 1995b, are negligible.

The accuracy in the determination of the sky background is a critical factor in the final accuracy of galaxy surface photometry, and particularly for low-surface-brightness galaxies or in the outermost faint regions of otherwise high-surface-brightness galaxies. In these cases, one often has to follow the galaxy surface brightness distribution down to less than 1% of the sky background. Such measurements will clearly be meaningless unless the sky background can be extremely accurately determined, and small errors in the determination of the sky background can result in large errors of the derived galaxy surface brightness radial profile. Even more dramatic errors are to be expected in the radial distributions of galaxy color indices, since these have to be obtained by subtracting two derived surface brighness radial profiles.

Besides the already significant advantage of the lower sky background, space observations are relatively easy to correct for this effect, since they do not suffer from the rapidly varying (in space and time) air glow. On the other hand, the typically small field of view of space observatories does not generally allow a very accurate determination of the sky background in the surroundings of a diffuse object such as a galaxy. This is still a severe problem with CCD detectors, e.g. with HST observations. It is expected, however, that this will not be the case for GAIA, since the Astros, provided the necessary data can be accommodated into the telemetry, will be able to map the sky background over the whole sky at the desired resolution. It should also be emphasized that the dominant contribution to the measurement errors in GAIA surface photometry is the readnoise, with an essentially negligible contribution from the sky background.

3.2.3 Point Spread Function and Seeing

Although it can be mathematically defined as a probability density function (see Subection 6.2.2), in practice the Point Spread Function (PSF) of a given observation taken with a given instrument describes the surface brightness distribution generated by a point-like source on the focal plane of the instrument during the observation. Thus, roughly speaking the PSF also describes the angular resolution achieved in an observation, which is degraded by instrumental defects as well as by environmental effects.

The most important contributions to the PSF come from atmospheric turbulence, or seeing, diffraction, geometric and chromatic aberrations. The quality of virtually any ground-based astronomical observations, however, is limited by seeing only. Despite the remarkable progress made in adaptive optics techniques, space observatories presently provide the only means to achieve truly diffraction-limited images, and thus small-scale information on a number of astronomical objects. Most of the outstanding results derived from HST observations are due to its unprecedented angular resolution, obtained with a relatively modest-size telescope.

In galaxy surface photometry, seeing most clearly affect the observations near the galaxy centers. The true surface brightness radial profiles of galaxies, for instance, tend to diverge, as $r \rightarrow 0$, as negative powers of r. The effect of seeing is to make the observed profile fainter at small radii and brighter at large radii, introducing a central region of nearly constant surface brightness of size approximately equal to the the FWHM of the PSF. The observation of steep brightness cusps at the centers of nearby galaxies, such as those found from HST observations by Lauer et al. 1995 and Byun at al. 1996, have therefore been prevented until recently by this effect. Moreover, since some theoretical models, e.g. King dynamical models, predict internally flat profiles of this kind, it was until recently widely believed that the observed flat profiles indicated true flat profiles rather than artifacts introduced by seeing. Another observational effect due to seeing is the distortion of the galaxy isophotes, namely their systematic rounding with respect to the true ones near the galaxy centers. The overall effect of seeing is thus to prevent the ground-based study of small-scale phenomena in most external galaxies.

In this respect, the high angular resolution and the all-sky coverage provided by GAIA will allow to peer into the cores of a large sample of galaxies, thus yielding

an unequaled wealth of information on the inner photometric structure and brightness profile, suitable for statistical studies.

3.3 The GAIA Galaxy Survey

Since the time of the Herschels, surveys of bright galaxies have provided the foundations upon which much of observational cosmology rests. Traditionally, these have been carried out on large-scale photographic plates, and only with the recent Sloan Digital Sky Survey CCDs have been successfully employed to image a significant portion of the northern sky. Owing to the revolutionary nature of the GAIA mission, the GAIA Galaxy Survey has little in common with previous galaxy survey projects, its main advantages being the nearly all-sky coverage, a well-defined selection function and a very high angular resolution. The overall measurement capabilities expected from the GAIA Galaxy Survey are described in the following Chapters. For the time being, and for a general discussion of its scientific objectives, it suffices to say that multi-color, multi-epoch photometry at a resolution better than 0.4 arcsec for some 3 million galaxies will be obtained.

Growth of structure in the Universe is believed to proceed from small-amplitude perturbations at very early times. Their growth from the radiation-dominated era to the present has been extensively studied, particularly in the context of the popular hierarchical clustering scenario. Many aspects of this picture are fairly well-established. Others are subject of active definition through redshift and imaging surveys of galaxies, and the microwave background experiments. There are several aspects of this research which require very wide area imaging surveys with high angular resolution to provide high-reliability catalogues of galaxies and quasars extending to low Galactic latitudes. Here GAIA will contribute uniquely, by detecting and providing multi-color surface photometry at high angular resolution for all sufficiently high surface brightness galaxies. This provides a valuable and unique dataset at two levels: for study of the large-scale structure of the Local Universe probed through the spatial distribution of galaxies and for statistical studies of the photometric structure of their central regions.

3.3.1 Spatial Distribution of Galaxies with GAIA

The primary scientific requirement is for a very wide angle survey, reaching into the "zone of avoidance" al low Galactic latitudes, with a well-defined selection function. Such data are not available from ground-based imaging surveys, as star-galaxy separation to the required reliability cannot be achieved without high spatial resolution imaging. Simulations (see 5.6) indicate that the number of galaxies which can be detected and for which useful broad-band photometry can be obtained is of order 3 millions, corresponding to a magnitude limit of $I \simeq 17$ for a typical galaxy. Fainter and more compact galaxies around will instead not be detected in very large numbers due to the short integration time and relatively high readnoise. Detected galaxies will provide a measurement, through deconvolution of the measured angular power spectrum, of the spectrum of fluctuations well beyond the expected peak. Such data are both a natural complement to

the ongoing redshift surveys, and also provide an input catalogue for future extensions of those surveys. The very great volume surveyed locally both makes the survey an important local normalisation and potentially allows study of the largest scale lengths, without evolutionary complications.

A primary science case for such studies arises from the difficulty in understanding the peculiar motion of the Local Group. It is well-established that the Local Group has a peculiar motion of about 600 km/s towards $(l, b) = (268°, 27°)$. If our understanding of the gravitational instability picture for the growth of structure, and measurements of Ω_0 and biasing are valid, this must be explicable as acceleration by identifiable galaxy clusters, or massive single galaxies. The largest of these sources, especially the Great Attractor and Perseus-Pisces, remain poorly mapped, being at low Galactic latitudes.

A second scientific goal concerns the amplitude, shape and length of structure in the Local Universe. Large filaments, walls, and the Supergalactic Plane dominate the nearby galaxy distibution. All are lost, with present data, within $20°$ of the galactic Plane. It is not yet even clear if the Supergalactic Plane is a plane at all. It we are to understand the local large-scale structure, a reliable nearly all-sky galaxy survey is essential. At low Galactic latitudes random errors in star-galaxy classification, due to seeing, convolved with the numerical predominance of stars, prevent construction of such a catalogue, The combination of GAIA spatial resolution and multi-color photometry will allow substantially improved analyses.

3.3.2 Galaxy Surface Photometry with GAIA

The GAIA Galaxy Survey will also provide multi-color information for individual galaxies, allowing detailed multi-color photometric studies of their central regions. This will include those galaxies for which redshifts are being obtained directly or in follow-up programmes (SDSS, 2dF, 2MASS and DeNIS surveys), directly linking morphology and spectra. Detailed analysis of the inner luminosity profiles of a large sample of galaxies will define the true incidence of core structures and complex morphologies. Inner color gradients will map recent star formation and dust lanes. Central luminosity cusps may indicate massive black holes.

Those galaxies with bright cusps within the central GAIA PSF can be analysed as astrometric targets, in the same way as stars. In this case, which will include many active galactic nuclei, astrometric "jitter", i.e. a motion of the photocenter, may be detectable, if a significant contribution to the flux is spatially variable, e.g. due to the appearance or displacement of a feature in the source or to activity in the core region.

While specific modeling will be required on a case-by-case basis, correlation of motion of the photocenter with optical variability in Seyfert nuclei and quasars can test if nuclear starburst supernovae are a significant luminosity source. In case where no jitter is seen, these sources define the reference frame. The relative location of the optical nuclei and the active nuclei can also be measured with high angular accuracy.

Photometric studies of bright galaxies allow detailed analyses of internal structures such as spiral arms and star formation regions. For fainter, and less well-resolved galacies, simper analyses of such parameters as bulge-to-disk ratio and central photometric

cusp or nucleus structure are appropriate (Okamura et al. 1999). For the faintest useful images, model-based two-dimensional image analyses, typically involving maximum likelihood comparison of the images data with a set of simple models, have been developed and applied, especially to surveys as the HST MDS (Ratnatunga et al. 1999). These methodologies are capable of reliable analysis of galaxy images with signal-to-noise ratios comparable to those GAIA will produce for galaxies to magnitude $I \simeq 17$. A crucial advantage of the GAIA Galaxy Survey over other studies is that it will automatically be nearly all-sky and magnitude-limited. The selection function of the observed sample of galaxies will be well-defined in terms of galaxy angular size and surface brightness.

The scientific value of this huge and homogeneous database will impact all fields of galaxy research, naturally complementing the several redshift surveys and the deeper pencil-beam studies with very large telscopes. Among the most important unique GAIA science products will be the determination of the color and photometric structure in the central regions of a nearly magnitude-limited sample of relatively bright galaxies. Recent studies of early-type (Faber et al. 1997) as well as late-type galaxies (Carollo 1999) begin to address the wealth of structure in the central regions of galaxies. Early-type galaxies are crudely distributed into cores which are flat or are steeply rising, perhaps indicative of the effects of massive central black holes (van der Marel 1999). Late-type galaxies, instead, show an extreme diversity of central structures, probably providing the key to bulge and central disk formation. On the whole, galaxy core structures span a surface brightness range of over 10 mag/arcsec^2 (Carollo 1999). GAIA will provide three key elements: high and uniform spatial resolution, a large sample, and multi-color data.

Simultaneous multi-color light curves, albeit sparsely sampled, will naturally be obtained for every galaxy observed. Thus the statistical incidence of active galactic nuclei and related variability will be determined as a function of the photometric structure of the host bulge or inner disk. Other types of variable sources will also be detected, ranging from novae in the Local Group through Cepheids and luminous blue variables in more distant galaxies, to supernovae, and possible gamma-ray bursts. Rapid analysis of the photometric data during the mission will allow the identification of variable sources for dedicated follow-up by other telescopes.

Chapter 4

Statistical Model of Galaxies

In devising a suitable galaxy detection and observation strategy, a necessary first step is the development of a statistical model of external galaxies giving the relevant properties of a typical galaxy as function of a limited set of parameters. Such a model is required to estimate the number of galaxies that could be detected, the angular radius to which the surface brightness profile could be followed and the resulting telemetry rate.

The observations that are needed in order to build the model are the number density, angular size and surface brightness distribution of the galaxies observed on the sky. Observations in the V or I band are preferable because the very broad G band, in which galaxies will be detected, is intermediate between these two bands, and the broad bands that will be implemented in the BBP, and in which galaxy observations will be carried out, will approximately cover this wavelength range. Recent literature, and more specifically the Medium Deep Survey (MDS, Ratnatunga et al. 1999) and Hubble Deep Field North (HDF-N, Williams et al. 1996) databases, offer a substantial amount of data in both bands, extending to large sky regions and faint magnitudes. The model's results, however, are here expressed in the I band, since mostly I-band data were used. A magnitude limit of $I = 24$ mag, much fainter than it was in principle necessary for our purposes, was chosen, so as to provide an estimation of the average disturbance from galaxies to the observation of stars.

It turns out that, to a first approximation, the galaxy statistical properties that are relevant for our purposes can be conveniently expressed as function of two parameters only, namely the galaxy total magnitude and morphological type. It must be emphasized how, under our assumptions, these two parameters completely characterize the photometric properties of a galaxy. The predictions of our model are thus much different in nature from the results of conventional galaxy surface photometry analysis. While in the latter a set of parameters is fitted to galaxy images in order to obtain information about galactic structural properties, in our model the results of this analysis are combined to derive analytical expressions predicting the photometric properties of typical galaxies. While this model obviously cannot do justice to the strong individuality displayed by many galaxies, it is believed to yield sufficiently reliable results when, as in our case, only statistical properties, i.e. properties averaged over large samples, are of interest.

4.1 Morphological Classification

The classification of galaxies according to their shape is a fundamental tool in extragalactic astronomy. It is through classification schemes that astronomers identify how different types of galaxies are interrelated and thus build a deeper understanding of how galaxies form and evolve (van den Bergh 1998). The most widely used galaxy classification scheme was first proposed by Hubble 1926 and later variously refined by Hubble himself and others. In its definitive form, described by Sandage 1961 and visually illustrated by the famous "tuning fork" diagram shown in Figure 4.1, Hubble's scheme consists of four main morphological classes:

- Ellipticals (E) : elliptical galaxies are seen projected on the sky as more or less flattened ellipses, whose axis ratio roughly varies from 1 to 3. They have no particular substructure, and their surface brightness decreases very regularly from the center to the outer parts. They have no, or very little, interstellar matter, and a population of old stars. The effects of projection hinders us greatly in our attempts to determine the intrinsic shape of these galaxies, and the original long-standing hyphotesis of an axysimmetric ellipsoidal structure has recently been questioned.

- Lenticulars (S0) : lenticular galaxies consist of at least two components, namely a central stellar concentration, or bulge, structurally similar to an elliptical galaxy, and a rather flat stellar disk that shows no sign of spiral structures. In addition, they sometimes contain a bar-shaped stellar component crossing the galactic nucleus. Like E galaxies, they have little interstellar matter and a population of old stars.

- Spirals (S) : spiral galaxies consist of a stellar bulge, sharing the characteristics of an elliptical galaxy, and of a disk containing young stars, significant amounts of interstellar matter and a more or less well-defined spiral pattern. They can also contain a bar-like component as well as more unusual structures like rings and lenses, whose composition is similar, in general, to that of the disk component.

- Irregulars (Irr) : irregular galaxies are galaxies that cannot be classified in the three previous classes, usually owing to their lack of simmetry or of well-defined spiral arms. They frequently display structures like dust lanes or bright knots containing O and B stars.

These four basic classes can be divided into several further subclasses, but these finer distinctions will not be considered here.

As for the relative frequencies of the different morphological types, in recent years they have been extensively investigated via both visual and automated classification procedures. In particular, deep observation campaigns carried out with the HST, namely the Medium Deep Survey (MDS) and the Hubble Deep Field North (HDF-N), have proved that when such frequencies are calculated over magnitude-limited samples of different depths, then they strongly depend on the limiting magnitude, showing a sharp
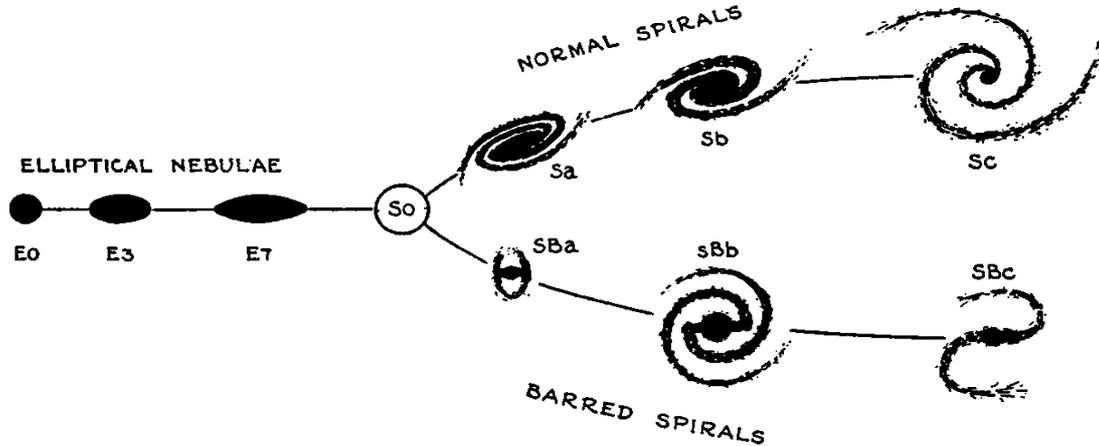
Figure 4.1: An early version of Hubble's galaxy classification scheme of regular galaxies, also known as the "tuning fork" diagram. Reproduced from Hubble 1936.

decrease in the number of spirals and an increase in the number of ellipticals and un-classifiable galaxies at faint magnitudes. Relative frequencies of morphological types in magnitude-limited samples of different limiting magnitudes are given in Table 4.1.

In Section 4.4 regular galaxies are divided into two classes, namely elliptical galaxies (E) and disk galaxies (D), on the basis of their surface brightness distribution. Taken the MDS frequencies from Table 4.1 as representative, it can be concluded that the relative frequencies of these two classes are of about 20% and 80% for E and D galaxies, respectively.

4.2 Number Counts

Galaxy differential number counts, giving the number of galaxies per unit sky area per unit magnitude interval as function of total magnitude, have always been a classical tool of observational cosmology. Consequently, a great effort has always been devoted to the extension of the observations to deeper magnitudes, larger sky regions and a wider range of colors. In particular, in the past few years I-band counts at high Galactic latitudes have been reliably extended down to $I \simeq 24$, as summarized e.g. by Shimasaku and Fukugita 1998. In our model, counts from three different sources were combined in order to cover as large a magnitude range as possible. At bright magnitudes, i.e. for $I \leq 19$, well-established counts were provided by Lattanzi 1997, whereas at fainter magnitudes results from Glazebrook et al. 1995 ($19 < I < 21$) and Abraham et al. 1996b ($21 < I < 24$) were used. A least-square polynomial fit in $\log N$ vs. I was performed on these data, in order to assess the consistency of the three sources and to obtain a functional form $N = N(I)$ for use in the following. It was thus found that a second degree polynomial was sufficient to obtain a good fit to the data. The number counts and the best-fit parabola are shown in Figure 4.2, while the best-fit parameters are given

Table 4.1: Relative frequencies of DDO morphological types in magnitude-limited samples of different limiting magnitude. SAC stands for Shapley-Ames Catalog (Shapley and Ames 1932), MDS for Medium Deep Survey (Ratnatunga et al. 1999) and HDF-N for Hubble Deep Field North (Williams et al. 1996), from Table 2 in van den Bergh et al. 1996. Morphological classifications from van den Bergh 1960, Abraham et al. 1996a and Abraham et al. 1996b, respectively. Wider DDO classification bins (E, S0, S, Ir and Unclassified) are indicated by horizontal lines. Note that the SAC makes no distinction between E, E/S0 ans S0, and that for the MDS and HDF data, only galaxies with I less than 21 and 24, respectively, were considered, in order to obtain a truly magnitude-limited sample and thus more robust estimates.

Type	SAC	MDS	HDF-N
E		16.6	23.9
E/S0	22.2	3.3	0.7
S0		6.9	4.3
S0/Sa	0.0	0.0	0.7
E/Sa	1.3	0.0	1.4
Sa	6.9	7.5	14.6
Sab	0.2	3.1	1.4
Sb	26.9	7.1	4.3
Sbc	0.3	4.0	0.0
Sc	22.9	12.8	1.4
S	10.0	14.6	13.2
Sc/Ir	0.2	0.9	0.0
Ir	2.0	6.4	2.5
Unclassified	7.0	16.8	31.4

in Table 4.2. According to this approximation, the differential number counts take the following functional form

$$N(I) = \text{dex}\left(a_N + b_N\, I + c_N\, I^2\right) \quad [\text{number deg}^{-2}\, \text{mag}^{-1}] \,, \tag{4.1}$$

where "dex" stands for the exponential function in base ten.

Values of the three parameters contained in Equation 4.1 are given in Table 4.2, while counts calculated with this formula are given in Table 4.4.

Table 4.2: Parameters of $\log N$ vs. I least-square second-degree polynomial best-fit. N expressed in number deg^{-2} mag^{-1}.

a_N	b_N	c_N
-9.9942	0.90564	-0.011493

The cumulative galaxy number counts, giving the total number of galaxies per unit sky
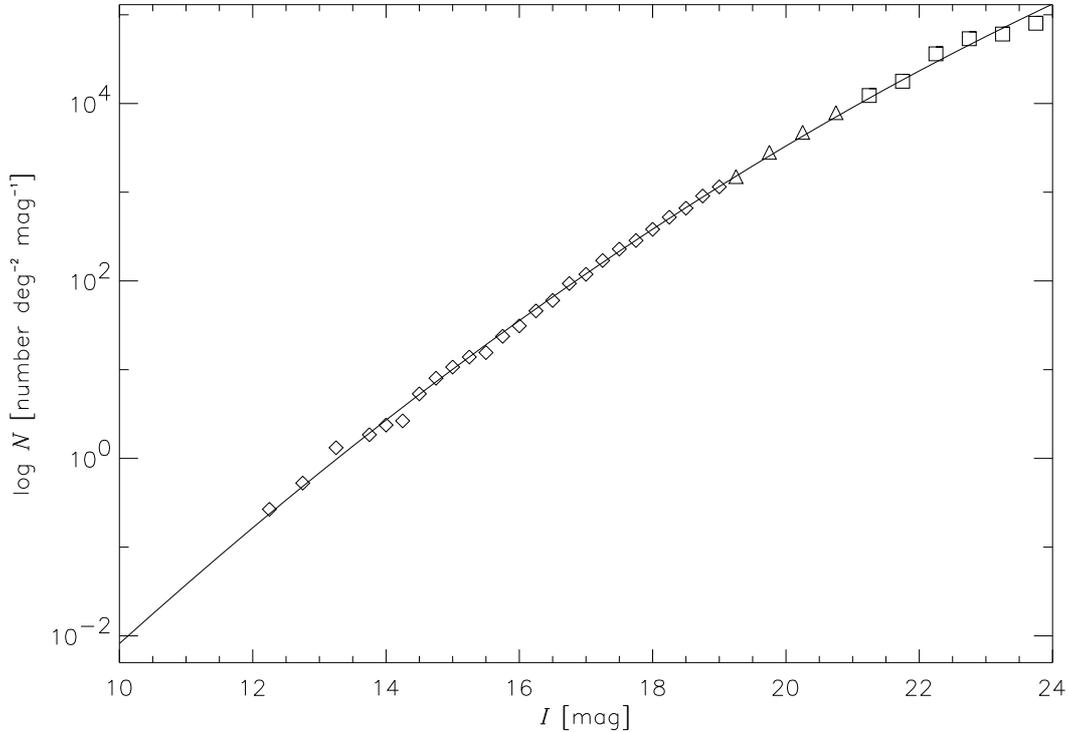
Figure 4.2: Galaxy differential number counts in the *I*-band. Data points from Lattanzi 1997 (diamonds), Glazebrook et al. 1995 (triangles) and Abraham et al. 1996b (squares). The solid line shows the least-square second degree polynomial best-fit.

area brighter than a given I magnitude I_c, are then given by the definite integral

$$N_c(I) = \int_{-\infty}^{I} N \, \mathrm{d}I' \quad [\text{number deg}^{-2}] \, . \tag{4.2}$$

Since the function given by Equation 4.1 does not have an analytic antiderivative, Romberg numerical integration (see Chapter 4 in Press et al. 1996), was performed. Cumulative galaxy number counts that were thus obtained are listed in Table 4.4.

4.3 Angular Size

Since galaxies are not sharp-edged objects, their angular size can be variously defined (see Mihalas and Binney 1981 and Binney and Merrifield 1998). As far as studies of surface brightness distribution are concerned, however, the parameter most widely used to characterize the size of a galaxy is its effective radius. This can be roughly defined as the radius encircling half of the light emitted by the galaxy, but in practice its measurement is usually performed through a more complicated process.

Surface photometry of galaxies (see e.g. Jedrzejewski 1987 for E galaxies and Kent 1985 for D galaxies) is usually analysed by fitting ellipses to the isophotes and by plotting their surface brightness versus their radius, which is defined as the geometric mean of the ellipse's semi-axes a and b, i.e. $r = \sqrt{ab}$. The resulting plot is then called the surface brightness radial profile of the galaxy. In this context, the effective radius of the galaxy is defined as the radius of the isophote encircling half of the light emitted by the galaxy, also called the effective isophote. The effective radius and the effective surface brightness, the latter being the surface brightness of the effective isophote, are usually indicated with r_e and μ_e, respectively.

Until the launch of HST, accurate measurements of the small angular sizes of faint galaxies were made virtually impossible by the phenomenon of seeing. The Medium Deep Survey (Ratnatunga et al. 1999), the first survey project to be carried out with HST superb instrumentation, has recently brought to an end this long-standing lack of meaningful data, while Im et al. 1995 have demonstrated the potential of angular size measurements to discriminate between currently competing cosmological models.

Casertano et al. 1995 have obtained effective radii for about 10,000 galaxies from Wide Field and Planetary Camera (WF/PC) parallel observations of random fields in the I band. As shown in their Figure 6, the observed angular size distribution as function of I magnitude shows a large scatter about the median value, mainly due to the intrinsic scatter in linear size and redshift distribution. The same figure also shows that the observed relation between the median effective radius and I magnitude is well-fit by the theoretically predicted relation for galaxies of constant central surface brightness $\mu_0 = 19.3$ mag/arcsec^2 and absolute magnitude $M_I = -20.5$ in the context of a mild luminosity evolution scenario. This latter relation asymptotically approaches the linear relation in log r_e vs. I that is measured in local samples of bright spiral galaxies following Freeman's law, and was therefore taken as a description of the relation between the galaxy effective radius and magnitude in our model. Least-square polynomial fit showed that its accurate description required a fourth-degree polynomial, which is represented in Figure 4.3, together with the Euclidean extrapolation to faint magnitudes of the local linear relation. The relation that in the following will be used to express r_e as function of I is therefore

$$r_e(I) = \text{dex}(a_r + b_r\,I + c_r\,I^2 + d_r\,I^3 + e_r\,I^4) \quad [\text{arcsec}] . \tag{4.3}$$

The values of the five parameters contained in Equation 4.3 are given in Table 4.3. Note

Table 4.3: Parameters of log r_e vs. I least-square fourth-degree polynomial best-fit. r_e expressed in arcsec.

a_r	b_r	c_r	d_r	e_r
$3.57702 \cdot 10^0$	$-2.12805 \cdot 10^{-1}$	$5.34616 \cdot 10^{-3}$	$-4.62001 \cdot 10^{-4}$	$1.28947 \cdot 10^{-5}$

that it is assumed not only that r_e depends on I only, but also that the same relation holds for all galaxies, irrespective of their morphological types. Note that, in view of the statistical considerations about galaxy detection that will be made in Chapter 5,
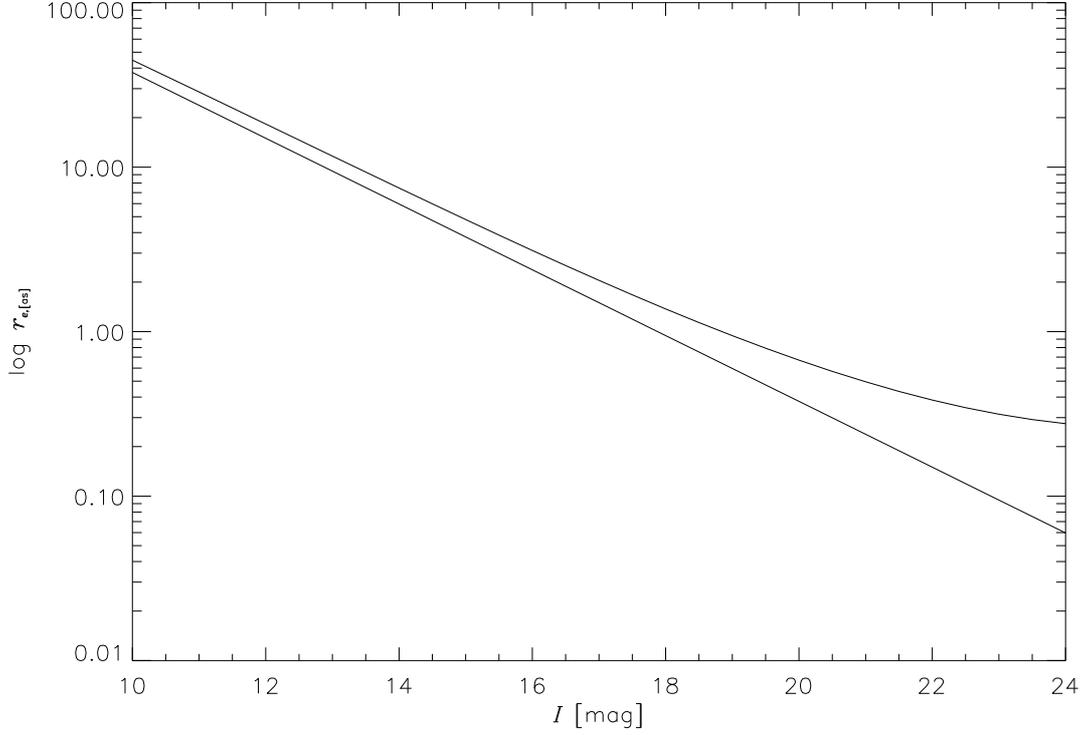
Figure 4.3: Median galaxy effective radius in the *I* band. The straight line represents the Euclidean extrapolation to faint magnitudes of the result valid for local samples of spiral galaxies following Freeman's law, while the curve represents the best fourth-degree polynomial fit to the theoretically predicted relation that best fits the observations at faint magnitudes. Note the pronounced divergence of the two curves for $I \gtrsim 19$. From Casertano et al. 1995.

the assumption of a univariate relation between r_e and I will lead to a galaxy being detected more or less easily than modelled according to its compliance to the average relation expressed by Equation 4.3. From a statistical point of view, however, and as far as Equation 4.3 holds on average, the net effect on the total number of detected galaxies should be negligible. Effective radii calculated from Equation 4.3, are given in Table 4.4. A rough estimation of the typical surface brightness of the central regions of galaxies can be given by the average surface brightness inside the effective radius $<\mu>_e$. Under our assumptions, and from the definition of effective radius, this quantity is equal for E s and D s and can be written as

$$
\begin{aligned}
<\mu>_e &= -2.5 \log \left(\frac{F/2}{\pi \, r_e^2 \, \Sigma_{zp}} \right) = -2.5 \log \left(\frac{F_{zp} \, \text{dex}(-0.4 \, I)}{\Sigma_{zp} \, 2\pi \, r_e^2(I)} \right) = \\
&= 2.5 \log(2\pi) + 5 \log(r_{e,[\text{as}]}(I)) + I_{[\text{mag}]} \quad [\text{mag/arcsec}^2] \ .
\end{aligned}
\tag{4.4}
$$

Values of $<\mu>_e$ are given in Table 4.5. To characterize the total fraction of the sky

occupied by galaxies brighter than a given magnitude, one can define Ω_e as the total solid angle that lies within the effective radius of all galaxies brighter than a given magnitude. Since superposition of different galaxies on the same sky regions is negligible, at least in the magnitude range we are considering, Ω_e can simply be written as

$$\Omega_e(I) = \frac{\Omega_{sky}}{60^4} \int_{-\infty}^{I} \pi\, r_e^2(I')\, N(I')\, \mathrm{d}I' = [\text{Equations 4.1 and 4.3}] =$$

$$= \frac{\pi\,\Omega_{sky}}{60^4} \int_{-\infty}^{I} \mathrm{dex}\left[(2\,a_r + a_N) + (2\,b_r + b_N)\,I' + (2\,c_r + c_N)\,I'^{\,2} + 2\,d_r\,I'^{\,3} + 2\,e_r\,I'^{\,4}\right]\, \mathrm{d}I' \;,$$

$$(4.5)$$

where Ω_{sky} is the solid angle spanned by the whole sky (see Appendix A and the factor 60^4 was introduced to take into account the fact that the coefficients giving r_e and N as function of I are expressed in different angular units. Values of Ω_e/Ω_{sky}, calculated through Romberg integration of Equation 4.5, are given in Table 4.4.

Table 4.4: Number and size of galaxies according to our statistical model. Modelled differential and cumulative number counts, effective radius and fraction of sky inside the effective radius at different I.

I	N	N_c	r_e	Ω_e/Ω_{sky}
mag	$\mathrm{deg}^{-2}\,\mathrm{mag}^{-1}$	deg^{-2}	arcsec	10^{-6} sky
10	0.008183	0.005151	44.72	5.350
11	0.03777	0.02458	28.64	10.93
12	0.1654	0.1114	18.29	21.15
13	0.6867	0.4791	11.68	38.88
14	2.705	1.958	7.468	68.08
15	10.10	7.596	4.801	114.0
16	35.79	27.99	3.115	183.6
17	120.3	98.00	2.049	285.9
18	383.3	325.9	1.374	433.3
19	1159	1030	0.9446	644.0
20	3322	3093	0.6707	946.5
21	9032	8826	0.4954	1389
22	23290	23940	0.3838	2060
23	56970	61760	0.3147	3132
24	132200	151500	0.2758	4969

4.4   Surface Brightness Distribution

As explained in Section 4.3, the two-dimensional surface brightness distribution of a galaxy is usually analysed so as to produce a one-dimensional radial profile. It turns out that the different physical components of galaxies have characteristic radial profiles, so that it is possible to model the radial profiles of different classes of galaxies as sums of different components.

Following Binney and Merrifield 1998, as far as surface brighness radial profiles are concerned, we shall here distinguish only two classes of typical galaxies, namely the elliptical galaxies (E) and disk Galaxies (D), where the latter class include spirals and lenticulars. While elliptical galaxies will be modelled as made of a bulge component only, disk galaxies will be considered as the combination of a bulge and a disk component. In both cases, galaxy images are assumed circularly symmetric. Note that all data and modelled numerical values are given in the I band, but that the subsript I will be here dropped for convenience from most formulae. Note also that the derivation of the mathematical results and the description of the notation used in the following are given in Appendix D.

4.4.1 Elliptical Galaxies

The surface brightness radial profiles of elliptical galaxies are in general reasonably well described by de Vaucouleurs, or $r^{1/4}$, law, first introduced by de Vaucouleurs 1948

$$\Sigma_E(r) = \Sigma_{E,e} \exp\left(-7.6692\left[\left(\frac{r}{r_e}\right)^{1/4} - 1\right]\right) , \tag{4.6}$$

where the effective surface brightness is labelled with an additional "E" because in our model this quantity, unlike the effective radius, will in general be different for E and D galaxies. This law has succeeded in reproducing, with a remarkable accuracy, the profiles of quite a few E galaxies. For instance, Capaccioli et al. 1990 found that the $r^{1/4}$ fit of the surface brightness radial profile of the nearby standard elliptical NGC 3379 give residuals smaller than 0.08 mag over a 10 magnitude range. Makino et al. 1990, however, found from dynamical arguments that the $r^{1/4}$ law bore little physical significance, though it is the best-fitting function, and that $r^{1/n}$ laws with n in the range 3–10 gave almost as good fits for a range of r of about 100. More recently, Caon et al. 1993 showed that the best-fitting n correlates with the galaxy linear effective radius and luminosity, while Andredakis et al. 1995 found that the light profiles of the bulges of disk galaxies, which are also usually modelled with an $r^{1/4}$ law, are in fact best-fitted by $r^{1/n}$ profiles with an n correlating with the galaxy morphological type. Nevertheless, the empirical fitting function given by Equation 4.6 is useful for characterizing the global properties of galaxies, and by that token in this study elliptical galaxies and bulges of disk galaxies will both be modelled with $r^{1/4}$ laws.

On a magnitude scale, Equation 4.6 becomes

$$\mu_E(r) = \mu_{E,e} + 8.3268\left[\left(\frac{r}{r_e}\right)^{1/4} - 1\right] , \tag{4.7}$$

where $\mu_{E,e}$ is the effective surface brightness of E s expressed in mag/arcsec^2. This latter quantity can be expressed as function of r_e and I, and thus, via Equation 4.3, of I only, obtaining

$$\mu_{E,e} = 2.5 \log\left(22.665\right) + 5 \log\left(r_{e,[as]}(I)\right) + I_{[mag]} \quad [\text{number deg}^{-2} \text{ mag}^{-1}] . \tag{4.8}$$

Values of $\mu_{E,e}$ are given in Table 4.5.

4.4.2   Disk Galaxies

As first suggested by de Vaucouleurs 1959, the surface brightness radial profile of disk galaxies can be interpreted as the sum of two components, the so called bulge component following the $r^{1/4}$ law and the so called disk component following the exponential law

$$\Sigma_d(r) = \Sigma_0 \, \exp\left(-\frac{r}{r_s}\right) \; , \tag{4.9}$$

where Σ_0 is the central surface brightness and r_s is the so called disk scale length. Equation 4.9 can be rewritten in a form similar to the one used for the $r^{1/4}$ law as

$$\Sigma_d(r) = \Sigma_e \, \exp\left[-1.6783\left(\frac{r}{r_e} - 1\right)\right] \tag{4.10}$$

where

$$\Sigma_0 = 5.3567 \, \Sigma_e \; , \qquad r_s = \frac{r_e}{1.6783} \; . \tag{4.11}$$

Since the first systematic study of Freeman 1970, this law has been known to fit the profiles of the outer regions of a large class of disk galaxies and has, in fact, come to define the typical surface brightness profile of the intrinsically flat component of disk galaxies, to the extent that deviations from these profile are generally ascribed to the existence of other components or to the effects of dust. Assuming this analytical form for the profile of the disk component, one can then try to disentangle the contributions of the bulge and disk components by means of fitting techniques. The methods for doing this have in time undergone a great development, from the simple one-dimensional fitting procedure along the galaxy major axis first adopted by Freeman 1970 to the bidimensional decomposition techniques currently being developed, which are applied to whole galaxy images (see e.g. Byun and Freeman 1995). In this study, a bulge+disk profile will be considered, combining an $r^{1/4}$ law with an exponential law, thus not considering contributions from components such as spiral arms, bars, rings, lenses, or the photometric effcts of dust. The most general form of such a profile

$$\Sigma_D(r) = \Sigma_b(r) + \Sigma_d(r) =$$
$$= \Sigma_{b,e} \, \exp\left(-7.6692\left[\left(\frac{r}{r_{b,e}}\right)^{1/4} - 1\right]\right) + 5.3567 \, \Sigma_{d,e} \, \exp\left(-\frac{1.6783\,r}{r_{d,e}}\right) \; , \tag{4.12}$$

depends on two pairs of parameters characterizing the bulge and disk components, respectively. The only independent variable we have so far introduced in our model is the total magnitude, which however determines also the effective radius through Equation 4.3. Therefore, the values of two other parameters must be given in order to completely determine the form of Equation 4.12. A convenient choice are two quantities derived from bulge/disk decompositions and frequently reported in the literature, namely the bulge/bulge+disk ratio B/T, or the ratio between the brightness contributed by the bulge component and the total brightness, and the ratio $r_{b,e}/r_{d,e}$ between the effective radii of the bulge and disk components. As shown in Appendix D, these two

parameters completely determine the bulge+disk profile. As for B/T, Kent 1985 found that in intrinsically luminous D galaxies this is tightly correlated with the morphological type, falling from a mean value of 0.65 for S0 to a mean value of 0.15 for Sc and later types. Recently, Ratnatunga et al. 1999 found a mean B/T of 0.4 from the bulge/disk decomposition of the MDS galaxies. The same two references then agree in fixing to about 0.5 the mean value of $r_{b,e}/r_{d,e}$. Such an excellent agreement between parameters obtained from galaxies of largely different magnitudes suggested to consider the two parameters as fixed, without introducing in the model the complications of other free parameters. Values of $B/T = 0.4$, corresponding to a bulge/disk ratio $B/D = 0.666$, and $r_{b,e}/r_{d,e} = 0.5$ were therefore assumed. With our choices for B/T and $r_{b,e}/r_{d,e}$ the bulge+disk profile becomes

$$\Sigma_D(r) = \Sigma_b(r) + \Sigma_d(r) =$$
$$= 0.76931\,\Sigma_{D,e} \exp\left(-7.6692\left[\left(\frac{1.6617\,r}{r_e}\right)^{1/4} - 1\right]\right) + 2.9343\,\Sigma_{D,e} \exp\left(-\frac{1.3945\,r}{r_e}\right)\;.$$
$$(4.13)$$

In general, the bulge and disk components dominate the profile at small and large radii, respectively. Note, however, that due to the analytical form of the two profiles, at very large radii the bulge contribution eventually exceeds that of the disk. In fact, practically all (99%) of the brightness predicted by the disk profile falls within 4 effective radii, but for the bulge profile only 85% of the light is within 4 effective radii, and the model needs to extend out to about 19 effective radii to contain 99% of it. Shifting to a magnitude scale, the analytical expression for μ_D is not as simple as that derived for ellipticals and is

$$\mu_D(r) = \mu_{D,e} - 2.5 \log\left[0.76931 \exp\left(-7.6692\left[\left(\frac{1.6617\,r}{r_e}\right)^{1/4} - 1\right]\right) + 2.9343 \exp\left(-\frac{1.3945\,r}{r_e}\right)\right]\;.$$
$$(4.14)$$

The total brightness emitted by the galaxy and the effective surface brightness can be written as

$$F_{D,tot} = 15.796\,\Sigma_{D,e}\,r_e^2\;, \tag{4.15}$$

and

$$\mu_{D,e} = 2.5 \log(15.796) + 5 \log(r_{e,[\text{as}]}) + I_{[\text{mag}]} \quad [\text{number deg}^{-2}\,\text{mag}^{-1}]\;. \tag{4.16}$$

Table 4.5 reports the values of $<\mu>_e$, $\mu_{E,e}$ and $\mu_{D,e}$ for different total I magnitudes. The values therein listed in the second column will be used in Chapter 5 to estimate the number of galaxies that could be detected by GAIA ASM. On the other hand, the values listed in the third and fourth column will be used to estimate the standard error of GAIA broad-band photometry at the effective radius of a galaxy.

4.5 Model's Validity and Verifications

As it was stressed at various times in this Chapter, a model such as that here described cannot accurately describe the properties of any given galaxy. However, it is expected to

Table 4.5: Reprentative surface brightness levels of galaxies according to Equations 4.4, 4.8 and 4.16. Average inside the effective radius and at that radius for E and D galaxies. As discussed in Section 4.2, D galaxies are four times more frequent than E galaxies.

I	$<\mu>_e$	$\mu_{E,e}$	$\mu_{D,e}$
mag	mag/arcsec^2	mag/arcsec^2	mag/arcsec^2
10	20.2481	21.6410	21.2490
11	20.2800	21.6730	21.2809
12	20.3067	21.6996	21.3076
13	20.3321	21.7250	21.3330
14	20.3616	21.7545	21.3625
15	20.4023	21.7952	21.4032
16	20.4628	21.8557	21.4637
17	20.5531	21.9461	21.5540
18	20.6851	22.0780	21.6860
19	20.8718	22.2648	21.8727
20	21.1281	22.5210	22.1290
21	21.4702	22.8632	22.4711
22	21.9161	23.3090	22.9170
23	22.4851	23.8780	23.4860
24	23.1981	24.5911	24.1991

hold on average, i.e. when the average properties of a representative sample of galaxies are considered. Given the several rough approximations introduced, the question as to which extent the model is quantitatively reliable for the purpose of mission planning cannot be answered without a direct comparison between predicted and observed profiles. Before carrying out such a comparison, we will however make a few, essentially qualitative considerations about the model's general validity.

Roughly speaking, it is expected that our statistical model will reliably describe the surface brightness radial profiles of faint galaxies, while the brightest galaxies will display a stronger individuality and thus will require more realistic surface brightness distribution functions to be considered. This latter class of galaxies may tentatively be estimated to include all the galaxies in the Shapley-Ames Catalog (Shapley and Ames 1932), so about a thousand galaxies. These galaxies can display a very complex structure and be of very large angular extent, e.g. about 10 deg for the Large Magellanic Cloud. Most bright stars or HII regions will be smaller in angular size than the width of GAIA PSF, and thus will be detected as apparent points. Besides, these point-like structures will be superimposed on a complex background, where surface brightness can vary by magnitudes on small scales, depending on bars, spiral arms and dust lanes. Most of these galaxies will therefore require individual consideration, but conversely will allow particularly detailed scientific investigation. At fainter magnitudes, only the overall structure of galaxies will be relevant, and the typical properties predicted by our model will be useful.

As for a quantitative evaluation of model's reliability, a comparison between its predictions and some ground-based surface photometry of bright galaxies taken from the literature was carried out. Even though, owing to seeing, ground-based observations do not allow an accurate determination of the profiles in the galaxy innermost regions, they have the advantages of being available in substantial amounts and of frequently following the brightness profiles to very large radii. Conversely, space observations such as the HST WFPC2 images which in Chapter 6 will be used for the simulation of GAIA observations, cover a small field of view, have mostly low exposure times and are still very limited. In much the same way, the large availability in the literature of B-band profiles extending down to large radii suggested the use of these for model's verification. The conversions between B and I was carried out using the constant color index $B - I = 2.0$, and correspondingly $\mu_B - \mu_I = 2.0$, which is the average value for bright galaxies according to Prugniel and Héraudeau 1998. Thus, in order to obtain the predicted B-band brightness profile against which observations could be compared, the measured total B magnitude of the galaxy is transformed to I through the $I = B - 2.0$. Then the predicted I-band profile can be derived as described in Sections 4.4.1 and 4.4.2, for E s and D s respectively. Finally, the predicted B-band brightnes profile is derived through the $\mu_B = \mu_I + 2.0$.

For elliptical galaxies, the model's predictions were compared with the composite CCD-photographic brightness profiles obtained by Capaccioli et al. 1988. for 9 galaxies in the ranges $10.5 < B < 12.7$ and $18 < \mu_B < 28$ and down to radii of about 250 arcsec. These are typically found to agree with our model within 0.2 mag/arcsec^2 outside an inner circular area of radius about 1 arcsec. Within this area, the observed profiles show a sharp flattening which our model does not describe properly so that the predicted profile is systematically brighter than the observations. This is clearly due to the phenomenon of seeing, whose effects on galaxy surface photometry were described in Subsection 3.2.3, and is compensated by the observed profiles being systematically brighter than predicted at radii just above 1 arcsec.

For disk galaxies, the model's predictions were compared with the photographic surface photometry obtained by Boroson 1981 for 26 galaxies in the ranges $8.5 < B < 12.5$ and $18 < \mu_B < 26$ and down to radii of 120–240 arcsec. In this case, the observations are typically found to agree with the predicted profiles within 0.3 mag/arcsec^2 outside the 1-arcsec radius circular area where seeing flattens the observed profiles as observed in the ellipticals.

On the whole, it can be concluded that our model predicts the galaxy surface brightness radial profiles in the range of radii relevant for our purposes with an accuracy of about 30% for most galaxies. Such an accuracy in the model's predictions is considered satisfactory in view of its application to the planning of galaxy observation.

Chapter 5

Detection and Observation of Galaxies with GAIA

The general purpose of the planning of a scientific undertaking must be maximizing the overall expected results under given constraints. In the case of the GAIA mission, this is a particularly delicate aspect, since the satellite will have a relatively short operational lifetime and the amount of data that it will be possible to transmit to the ground, though very large, is far from what one would hope for such a high-performance instrument.

In this framework, an observing strategy was carefully devised in order to discriminate stars from the sky background, cosmic rays and other uninteresting features and thus to bring the telemetry rate down to manageable levels. Such a strategy needs to be "tuned" to allow the observation of galaxies, since these are diffuse objects that the star observing strategy was devised to ignore.

5.1 Detection and Observation

During the scientific operations, the GAIA satellite will continuously spin about its symmetry axis, and the charges contained in the CCD pixels will correspondingly be shifted along-scan to integrate the image for a sufficiently long exposure time. This observing strategy, while allows the coverage of the whole sky for on average 150 times during the mission, requires the implementation of a dedicated CCD readout process. The CCDs covering the focal planes of the Astros, in fact, contain plenty of data that must be readout approximately every 0.86 s, in order to catch up with the scanning of the satellite and the shifting of the charges along the CCDs. Should every bit of this huge amount of information be readout, this would yield an unbelievably high reading frequency and telemetry rate. Besides, the levels of readnoise[1] following from the high reading frequency would seriously compromise the quality of most data. This called for a

---

[1] The total noise arising from the CCD reading process is usually referred to as *read-out noise*. However, according to the nomenclature adopted by Vannier 1999 in the discussion of instrumental noise in GAIA Astro CCDs, the read-out noise is only one of the contributions to the total noise. For the sake of clarity, hereafter the total noise will simply be referred to as *readnoise*.

strategy to discriminate the sky regions containing scientifically interesting objects from those containing only noise or other uninteresting features in an automated manner, and to restrict the readout to the former.

Two possibilities for defining the interesting sky areas have been considered. The use of an input catalogue of about 100 million stars selected for their astrometric and astrophysical interest, would allow to limit the readout to the areas around these stars. But no survey exists that could be used as basis for a meaningful selection, and the construction of such a catalogue from scratch would be a very time-consuming and expensive undertaking.

The other possibility, the one finally chosen, is to detect stars as they enter the field of view, determine their position, magnitude and signal-to-noise ratio, and, if the latter exceeds a certain limit, to collect data around such stars during the remaining part of the field crossing. It has been shown that the amount of data can thus be reduced by at least a factor thousand. A further advantage of this approach is a clearer characterization of the observational selection effects, which is extremely important in evaluating the completeness and properties of the observed sample.

In this context, it is important to emphasize the distinction between the detection and the observation of an object with GAIA. Whether an object will be observed or not is determined only by its detection as it enters the field of view, not by any prior knowledge of its position, even if it has been previously observed by the satellite. Stars near the detection limit will not be generally detected and therefore observed during all scans. The on-ground database will however be able to instantly access all available observations of any required star or sky area for the purposes of data reduction.

The presently agreed-upon arrangement of the Astros focal plane, which was shown in Figure 2.7, resulted from detailed and extensive simulation of observations, and closely reflects the observing strategy outlined above. The CCD columns can be logically divided into four parts, whose roles can be described as follows:

- **Astrometric Sky Mapper (ASM 0-3)**: the main function of the ASM is object detection by real-time on-board data analysis. ASM 0 and ASM 1 are used for the detection and position measurement of bright and faint stars, respectively. ASM 2 is redundant, i.e. is not used in normal operations but is kept as a replacement if another should fail. ASM 3 is used to confirm the object detection, to refine the measurement of its position and to determine the satellite scan velocity. The position and velocity measurements, in particular, are used to propagate the measurement window through the remaining part of the field of view.

- **Astrometric Field (AF 1-16)**: the AF is used for astrometric and photometric observations. Its 16 CCD columns are used to measure astrometrically and photometrically (in the G band) the detected stars 16 times.

- **Photometric Sky Mapper (PSM)**: The single CCD column of the PSM is used to map the surroundings of the detected stars within a region of radius 1 arcsec, in order to correct the photometric observations carried out in the AF for the effect of disturbing stars.

- **Broad-Band Photometer (BBP 1-4(5))**: each of the 4-5 CCD columns of the BBP is used to measure photometrically the detected stars in a different photometric band. Note that the other parts of the field of view all work in the G band defined by the telescope transmittance and the CCD quantum efficiency.

The general philosophy underlying the CCD readout and the data transmission must be that of maximizing the scientific content per readout/transmitted bit, taking into account that a large CCD binning size implies a reduction in the readnoise, which is the dominant noise source for faint objects, far larger than the sky background. Therefore, over the four different parts of the field of view, and, in the case of the ASM, even over the different columns of the same part, the CCDs are readout with a different binning matched to the specific scientific purpose, which also determines the area of the sky region around each detected object from which data are transmitted to the ground. As far as nomenclature is concerned, the CCD elementary binnning region is called a *sample*[2], while the sky region that is observed around each detected object is called a *patch*.

The optimization of the all-mission astrometric and photometric performance with respect to sampling has lead to the rectangular, slightly elongated shape of ASM samples, and to much more elongated, essentially one-dimensional, samples in the other parts of the focal plane. Clearly, this different choice is due to the need of performing two-dimensional position and velocity measurements at each scan in the ASM, while one-dimensional single-scan measurements in the other CCDs suffice to reconstruct the positions and motions of the observed objects.

The presently planned sampling scheme of GAIA instruments is illustrated in detail in Figure 5.1. Note, in particular, that the sample size chosen for the BBP of the two Astros is different, being 1×8 pixels in Astro 1 and 6×8 pixels in Astro 2. With this choice the Astro 1 yields a better photometric accuracy for bright stars, wheras the Astro 2 is more accurate for faint stars. Simulations have shown that with such an observing strategy stars of,e.g., $I = 20$ can be detected with a probability of 0.9.

Another stringent requirement on the CCD readout process is that, in order to ensure the greatest thermal stability, the reading frequency of all the CCDs must be kept constant. Roughly speaking, the reading frequency (or telemetry rate) can be written as the product of two factors, namely the readout (or transmitted) data per detected object and the number of detected objects per unit time. The first factor depends on the sample and patch sizes, actually on the ratio between patch and sample size, which vary greatly depending on the column of CCDs under consideration. The second factor depends on the number of objects brighter than the detection limit per unit solid angle, which in turn is a strong function of the Galactic coordinates of the instantaneous field of view, being very high near the Galactic plane and relatively low at high Galactic latitudes, with smaller variations on very short space scales. Consequently,

---

[2] Note that in the following *sample* will be used to indicate both a *sample size*, i.e. the area of the sky region corresponding to more electronically binned pixels, and sometimes a *sample value*, i.e. the charge obtained from the readout of the sample area. Thus a sample value is obtained through A/D conversion of the charge accumulated at the serial register of the CCD.
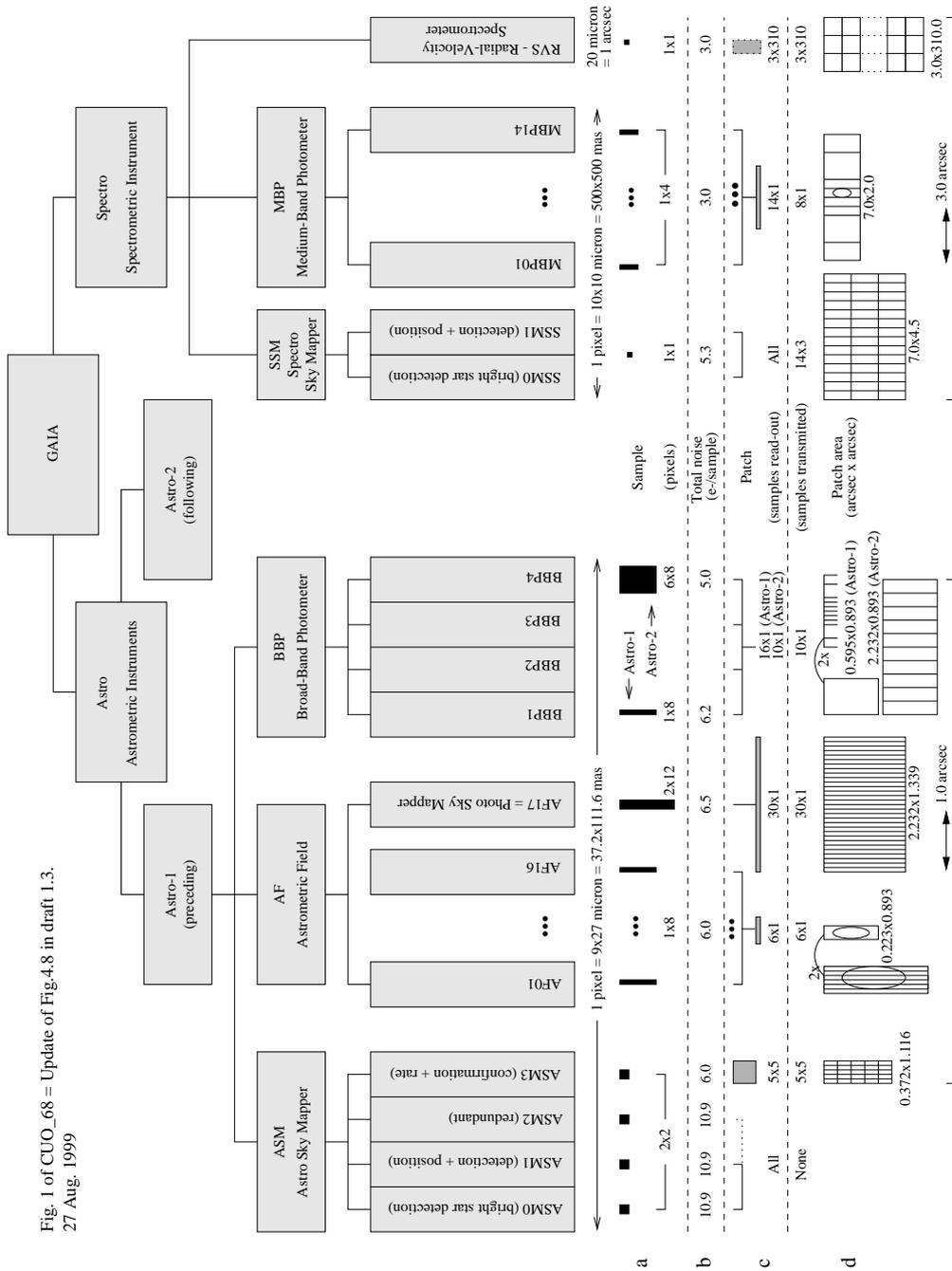
Figure 5.1: The sampling scheme in GAIA instruments. Sample and patch sizes are indicated, together with the expected readnoise levels. The Airy Disk of the Astros is shown as a solid ellipse, while the dashed ellipse shows the elongation due to the maximum value of the across-scan motion of the image during the 0.86 s integration time. From Høg 1999. Courtesy of Erik Høg, Copenhagen University Observatory.

in the course of the mission the reading frequency of useful data vary greatly on short time scales, and therefore most of the time some dummy samples not belonging to any object are readout, but not used further, to ensure that the total reading frequency is kept constant. The presently planned value of the total reading frequency is set by the requirement of observing up to $2\,800\,000$ stars/deg^2. Only a small fraction of the sky has a such a high star density, and it has been suggested that this requirement could be relaxed in order to obtain a lower readnoise per unit area, which would result in a higher accuracy. The readnoise could be very effectively decreased by the use of a total reading frequency matched to the number of samples to be read, but at the cost of complexity in the thermal control.

Once the samples from the Astros have been transmitted to the ground, they can be analyzed in various ways to obtain astrometry and/or photometry[3]. The samples belonging to a patch can, e.g., be analyzed alone to give epoch astrometry and photometry. All the patches belonging to the same sky region may then be analyzed together to get all-mission average measurements of the astrometric parameters. When all-mission averages of the astrometric parameters are known, it is possible to return to the single patches in order to derive more accurate epoch and all-mission photometry. Generally speaking, the derivation of the astrometric parameters will precede the photometric analysis. Thus, the astrometric parameters and the energy flux of the objects in several colors may be derived from all the patches covering the same sky region.

5.2   Detection and Observation of Galaxies

At an advanced stage in the course of the mission feasibility studies, the idea of carrying out galaxy observations with GAIA was first put forward by Høg, Fabricius, Knude and Makarov 1998a and Høg, Fabricius, Knude and Makarov 1998b, who suggested that galaxies could be detected as high-surface-brightness regions in the ASM and observed in the BBP with minimum impact on the expected accuracy for the observation of stars and on the telemetry[4]. According to the ideas expressed in these papers, when an average surface brightness significantly in excess over the local sky background is measured in a square area of a few arcsecond size in the ASM 1, then a galaxy has probably been detected and the samples covering this area and its surroundings in the BBPs should then be transmitted to the ground. Since, in so doing, whenever a galaxy was being observed it would not have been possible to observe stars, it was suggested that detection and observation of galaxies were to be carried out in one of the two Astros only, so as to let the other one to observe stars over the whole mission.

---

[3] Note that in the following it is assumed that the astrometric calibration, i.e. the satellite attitude and the geometric parameters of the focal plane are available from a previous calibration process, which yields the position of each sample with an accuracy better than about 1 mas.

[4] The original proposal actually suggested that the detection of high-surface-brightness regions all over the sky would have naturally brought to the observation of Galactic nebulae as well. This possibility, however, has not been investigated in this study, owing to the suspected serious difficulties in the detection at very low Galactic latitudes originating from the crowding of the focal plane.

Some practical problems have to be solved in order to follow this general idea. One has to define:

- a local sky background with which the average surface brightness measured in the square areas can be compared. This may basically be determined from ASM 1 samples of 2×2 pixels by trimmed median filtering. For instance, it is presently envisaged to transmit to the ground the values thus obtained over 12×12 arcsec^2. The median of these values over several degrees of scan may be used as reference against which comparison is made. However, the exact method used to determine the local sky background is not of interest for our purposes, since the readnoise is by far the dominant noise source.

- a reasonable value for the detection area and level so that useful data are transmitted without being swamped in less interesting data from the Milky Way or the zodiacal light. A trimmed median filtering technique such as that planned for the determination of the local sky background but averaging within a smaller area may be effectively used. The larger the detection area, the fainter the detection limit can be for objects of constant surface brightness, if the error on the sky background is negligible. On the other hand, the detection area should be small enough that a large number of small objects would not be missed.

- a useful sampling scheme for galaxy observations, so as to establish a trade-off between the angular resolution, the readnoise and the telemetry. As discussed in the previous Section in connection with the observations of stars, a larger sample size yields a smaller error on the (average) surface brightness, lower readnoise and telemetry rate but also a lower angular resolution. This aspect is critical for the observations of galaxies, since their potentially very large angular extension will require in some cases the readout of entire CCDs.

The most realistic, but time-consuming, approach to the solution of these problems requires devising and implementation of a suitable detection and observation strategy, followed by numerical simulations based on real fields imaged with an higher depth and resolution than it is achievable by GAIA. This approach was thoroughly and successfully followed in the planning of the observation of stars. As for galaxies, in this Chapter their detection and observation will be discussed from a statistical point of view only, and preliminary results from numerical simulations of galaxy detection will be summarized. The observation strategy outlined here, instead, was tested through numerical simulations described in Chapter 6.

5.3 Statistical Formulae

The problem of the detection/observation of an astronomical object superposed on a smooth sky background and imaged with a CCD detector can be mathematically described as the general problem of the detection/observation of a Poisson signal (photo-electrons originating from the object under consideration) in presence of Poisson noise

(photoelectrons originating from the sky background) and Gaussian noise (readnoise). Following a simple statistical approach, general analytical formulae for the signal-to-noise ratios and standard errors of CCD photometry can be derived, which are convenient to use during the instrument design and mission planning phases because they give very similar errors to those obtained from simulations. The use of analytical formulae has the additional advantage over simulations that the relative importance of the various error sources is more easily seen.

Our goal is to derive general formulae expressing the signal-to-noise ratio produced by an object within a given aperture during a given exposure time, and then to apply them to the cases of detection and observation. As for detection, the estimation of the signal-to-noise ratio leads to estimate the number of galaxies that could be detected under the present assumptions for sampling and readnoise in the ASM 1. As for observation, a comparison between the estimated accuracies in surface photometry achievable with different sample sizes can be given.

The conventions used in the following are as follows:

- t : single-scan exposure time [s]

- aperture : the angular size of the sky area over which the measurement is performed [solid angle]

- n_s : number of samples within the aperture

- F : total electron counts within the aperture during t [e$^-$]

- S : electron counts from the object within the aperture during t [e$^-$]

- b : electron counts from the sky background per sample during t [e$^-$]

- σ_f : standard error of generic estimated flux $f = F, S, b$ [e$^-$]

- r : total readnoise per sample [e$^-$ rms]

- n_{obs} : number of superposed observations

- SNR : signal-to-noise ratio in the measurement of S

- σ_{mag} : relative standard error in the measurement of S [mag]

Under these assumptions, F can be written as

$$F = S + n_s\, b \ . \tag{5.1}$$

The physical process of the emission of photons fron an astronomical object can be statistically described in terms of a Poisson distribution. The standard error in the measurement of F is then due to the intrinsic Poisson noise associated with F and to the readnoise. These two contributions sum quadratically yielding for the variance of F

$$\sigma_F^2 = F + n_s\, r^2 = S + n_s\, b + n_s\, r^2 \ . \tag{5.2}$$

Since the signal S from the object is estimated by subtraction from F of the sky background

$$S = F - n_s\, b \ , \tag{5.3}$$

the variance of S is

$$\sigma_S^2 = \sigma_F^2 + (n_s\, \sigma_b)^2 = S + n_s\, b + n_s\, r^2 + (n_s\, \sigma_b)^2 \ . \tag{5.4}$$

SNR is then

$$SNR = \sqrt{n_{obs}}\ \frac{S}{\sigma_S} = \frac{\sqrt{n_{obs}}\, S}{\sqrt{S + n_s\, b + n_s\, r^2 + (n_s\, \sigma_b)^2}} \ , \tag{5.5}$$

while σ_{mag} is

$$\sigma_{mag} = \frac{2.5 \log e}{\sqrt{n_{obs}}\ SNR} = \frac{1.08574\ \sqrt{S + n_s\, b + n_s\, r^2 + (n_s\, \sigma_b)^2}}{\sqrt{n_{obs}}\ S} \ . \tag{5.6}$$

Even though SNR is given by Equation 5.5 both for detection and for observation, its meaning is very different in the two cases. In the case of detection, an high SNR means a safe detection, i.e. an high chance of having detected a galaxy. As for observation, an high SNR means an accurate observation, i.e. a small error in surface photometry. In order to apply the previous formulae, one needs to estimate the sensitivity, the readnoise and the sky background levels of the Astros.

5.4   Sensitivity of the Astros

In the estimation of an instrument's sensitivity, the transmittance of the telescope, the Quantum Efficiency of the detector and the spectrum of the observed object must be taken into account. On the basis of the data for the baseline mission design provided by Matra Marconi Space, expected photoelectron count rates for stars of different spectral types in different photometric bands were provided by L. Lindegren in a private communication. To determine the stellar spectrum most closely approximating the spectrum of a typical galaxy, a comparison between Kinney template galaxy spectra and Kurucz theoretical stellar spectra was carried out. It was thus found that a good approximation to the Kinney spectra is given by the Kurucz spectrum for a G2V star, as is shown in Figure 5.2, where the Kinney spectrum of a Sb galaxy is used for illustrative purposes. The expected photoelectron count rates for a G2V star in the G band and in the bands of the $fgriz$ photometric system (see Subsection 2.4.1) are listed in Table 5.1 for stars of magnitude $I = 15.0$ and interstellar extinction $A_I = 0.0$.

5.5   Sky Background and Readnoise

The sky background as it is observed from the ground and from space was discussed in Subsection 3.2.2, and it was concluded that for our purposes a conservative value of
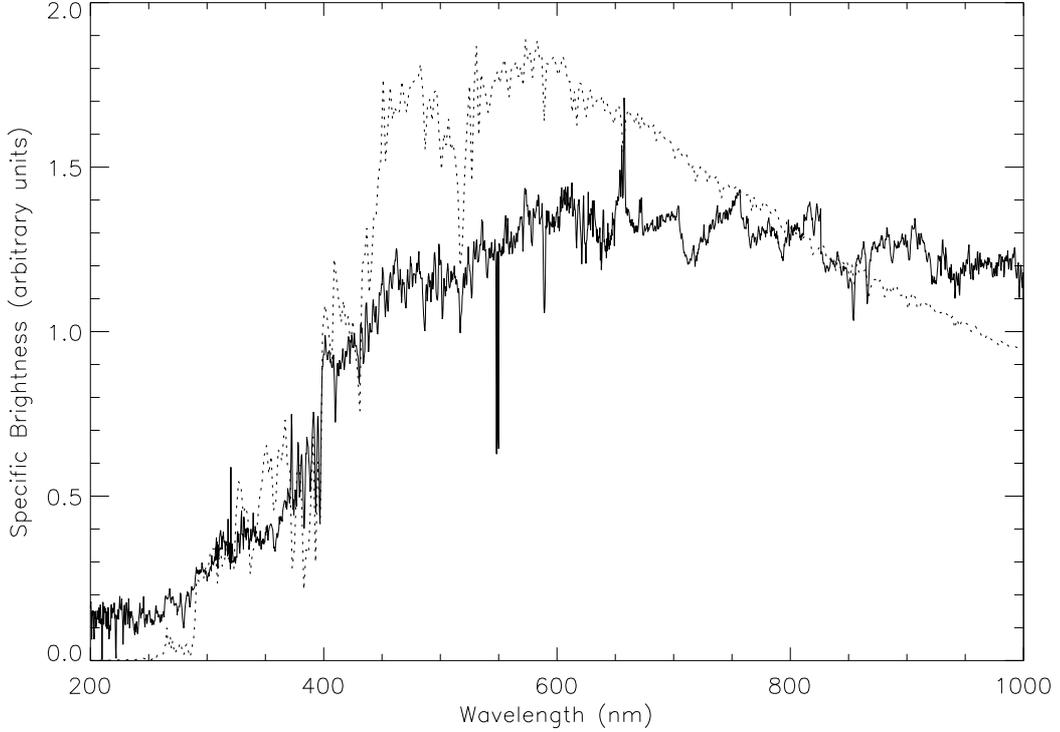
Figure 5.2: Comparison of Kinney Template Galaxy Spectra and Kurucz Theoretical Stellar Spectra. The solid line shows the Kinney spectrum for a Sb galaxy, whereas the dotted line shows the Kurucz spectrum for a G2V star. Galaxy spectrum from Kinney et al. 1996, stellar spectrum from Munari and Castelli 2000.

Table 5.1: GAIA expected photoelectron count rates. Rates of detected photoelectrons in the CCDs of GAIA Astros for a G2V star in the G and $fgriz$ photometric bands. $I = 15.0$ and $A_I = 0.0$ were assumed. Count rates expressed in electrons/s. The corresponding count rates for some spectral types earlier and later than G2V are included for illustrative purposes. Courtesy of Lennart Lindegren, Lund Observatory.

ST	G	f	g	r	i	z
A5V	32552	9705	6780	4894	3065	1463
F6V	23783	5574	4872	4236	2936	1507
G2V	20079	3984	4096	3892	2866	1541
K3V	16104	2416	3208	3558	2766	1564
M0V	11015	844	1640	2470	2545	1632

$\mu_{bg,I} = 21.0$ mag/arcsec^2 can be assumed for the sky background. In the following it will be furtherly assumed that the sky background is unifom within the aperture and has the same G2V spectrum assumed for galaxies in the previous Section. As already

noted, however, the sky background will be negligible in the global error budget of GAIA surface photometry.

The total readnoise levels of GAIA CCDs in the ASM 1 and in the BBPs of the Astros can be estimated following the recipe of Vannier 1999. The values obtained for the presently planned sampling of the ASM 1 are given together with the values obtained for four different sample sizes in the BBPs in Table 5.2. Even though the sample size in the ASM 1 appears fairly well-established, the values obtained for different sample sizes in the ASM 1 are also included to illustrate how a decrease in the required accuracy of two-dimensional position measurements in the ASM would result in a substantial reduction of the readnoise.

Table 5.2: Readnoise levels of GAIA Astro CCDs in the ASM 1 and BBPs. Full readout of the CCDs was assumed both for the ASM 1 and the BBPs. Values corresponding to three and four sample sizes are given for the ASM 1 and the BBPs. Note that 1×8 and 6×8 pixels/sample are presently planned for the observation of stars in the Astro 1 and Astro 2 BBPs, respectively.

Parameter	Unit	ASM 1	ASM 1	ASM 1	BBPs	BBPs	BBPs	BBPs
Sample Size	pixels	2×2	3×3	4×4	6×8	6×4	6×2	1×8
Readnoise	e$^-$ rms	10.63	7.92	6.72	5.44	6.74	8.79	10.44

5.6   Expected Number of Detected Galaxies

Introducing the data given in Sections 5.4 and 5.5 in Equation 5.5, an estimation of the signal-to-noise ratio SNR produced by a given average surface brightness within an aperture of a given size can be given. In particular, we are interested in the range of angular sizes and average surface brightnesses covered by the inner regions of bright galaxies, which will obviously be the easiest to detect. These two quantities can be characterized by the galaxy effective radius and by the average surface brightness within the effective radius, which have been given, for galaxies of different total magnitudes, in Tables 4.4 and 4.5, respectively. Values of SNR for apertures and average surface brightnesses in the relevant ranges are given in Table 5.3.

These values can be used to estimate the number of galaxies that could be detected by GAIA ASM 1 when adopting different aperture sizes. To ensure a safe detection, so as not to be swamped with undesirable data, a SNR of about 4 is required, which is achieved, e.g., for $<\mu>_{ap}= 20.5$ with a 3×3 arcsec^2 aperture. With such an aperture, most galaxies of $I = 16$, which have $r_e = 3.1$ and $<\mu>_e= 20.5$, according to Tables 4.4 and 4.5, will be detected during most scans. On the other hand, fainter and smaller galaxies will only be detected some times, e.g. if the center of the galaxy happens to lie near the center of one of the apertures used for detection. Besides, since the average surface brightness within a radius smaller than the effective radius can be significantly larger than $<\mu>_e$, with a smaller aperture size one could detect an higher number of galaxies, but on the other hand such a choice could yield an higher number of false

Table 5.3: Signal-to-Noise Ratio SNR for Galaxy Detection, according to statistical formulae. SNR is given for different values of aperture size and I-band average surface brightness within the aperture $<\mu>_{ap}$, according to Equation 5.5. Aperture size expressed in arcsec^2, $<\mu>_{ap}$ in mag/arcsec^2.

SNR		Aperture Size						
		4.0×4.0	3.5×3.5	3.0×3.0	2.5×2.5	2.0×2.0	1.5×1.5	1.0×1.0
	20.00	7.8341	6.9344	6.0047	5.0482	4.0683	3.0689	2.0544
	20.25	6.2371	5.5210	4.7811	4.0197	3.2395	2.4438	1.6360
	20.50	4.9633	4.3937	3.8050	3.1992	2.5783	1.9450	1.3021
$<\mu>_{ap}$	20.75	3.9483	3.4952	3.0270	2.5451	2.0512	1.5474	1.0360
	21.00	3.1398	2.7797	2.4074	2.0241	1.6314	1.2307	0.8240
	21.25	2.4964	2.2100	1.9141	1.6094	1.2972	0.9786	0.6552
	21.50	1.9844	1.7568	1.5216	1.2794	1.0312	0.7779	0.5208

detections, resulting in loss of telemetry.

A more detailed understanding of the issue requires a more complete simulation taking into account the surface brightness radial profiles for E and D galaxies as they were modelled in Chapter 4 and the different possible positions of the galaxy center with respect to the aperture center. Numerically integrating the profiles of E and D galaxies of different magnitudes over square areas of different sizes and whose centers are randomly displaced from the galaxy center, one can obtain a clearer picture of which galaxies will be detected and with which probability. The percentages of detected galaxies obtained from these simulations are given as function of total magnitude and aperture size in Tables 5.4 and 5.5 for E and D galaxies, respectively, where a SNR of 4 has been assumed to indicate a detection.

Table 5.4: Detection Probability of Elliptical Galaxies $P_{det,E}$ in the ASM 1 as function of galaxy total I magnitude and aperture size, according to numerical simulations. Detection probability expressed in percentage, aperture size in arcsec^2. See text for details.

$P_{det,E}$		Aperture Size						
		1.0×1.0	1.5×1.5	2.0×2.0	2.5×2.5	3.0×3.0	3.5×3.5	4.0×4.0
	16.00	100	100	100	100	100	100	99
	16.25	100	100	100	98	97	95	91
	16.50	100	99	98	93	95	83	70
	16.75	100	94	90	84	76	58	46
I	17.00	91	87	80	66	37	27	07
	17.25	72	65	52	25	00	00	00
	17.50	45	32	00	00	00	00	00
	17.75	07	00	00	00	00	00	00
	18.00	00	00	00	00	00	00	00

Table 5.5: Detection Probability of Disk Galaxies $P_{det,D}$ in the ASM 1 as function of galaxy total I magnitude and aperture size, according to numerical simulations. Detection probability expressed in percentage, aperture size in arcsec^2. See text for details.

$P_{det,D}$		Aperture Size						
		$1.0{\times}1.0$	$1.5{\times}1.5$	$2.0{\times}2.0$	$2.5{\times}2.5$	$3.0{\times}3.0$	$3.5{\times}3.5$	$4.0{\times}4.0$
	16.00	100	100	100	100	100	100	99
	16.25	100	99	99	97	97	94	91
	16.50	98	94	95	86	92	79	66
I	16.75	81	86	82	76	63	55	46
	17.00	60	62	58	50	26	23	08
	17.25	32	27	20	02	00	00	00
	17.50	00	00	00	00	00	00	00

As expected, the number of detected galaxies increases steadily with the decrease in the aperture size both for E s and D s. Below a certain aperture size, however, this estimation becomes rather uncertain due to the present poor knowledge of brightness profiles in the galaxy innermost regions. Besides, since some kind of median filtering will be required in order to discriminate between bright stars and galaxies, the measured signal will in fact be smaller than estimated, and this effect will become significant as the aperture size decreases. In any case, a lower limit to the aperture size must be set depending on the number of false detections that are deemed acceptable.

The thorough understanding of the problems connected with false detections requires the design, implementation and testing on real fields of a dedicated algorithm for galaxy detection, but this was beyond the scope of the present study. It is however believed that an aperture size of 2×2 arcsec^2 is large enough to be safely used in the following considerations. With such a choice, E and D galaxies of, e.g., $I = 17$ are detected with a probability of about 80% and 58% respectively, whereas for $I \gtrsim 17$ the detection probability quickly falls to zero. With an average number of scans of 75 per astrometric instrument (see Figure 2.4), should galaxies be observed for the whole mission in one Astro, an average of 60 and 45 scans would be obtained for E s and D s, respectively, which, as we shall see in Chapter 7, are largely sufficient to reconstruct a high-resolution two-dimensional image. It can therefore be concluded that galaxies brighter than $I_{det} = 17$ would be detected during the 60% of the scans with a $SNR = 4$ in the ASM 1 using an area of 2×2 arcsec^2 for detection. According to Table 4.4, there are about 4 million galaxies brighter than this limit on the whole sky. At low Galactic latitudes, though, galaxy detection becomes increasingly tricky due to the presence of Galactic nebulae and lots of stars. While it would be desirable to observe galaxies as well as Galactic nebulae down to very low Galactic latitudes, it is suspected that this could yield a large amount of false detections and thus loss of telemetry. Very conservatively, the galaxy detection could be carried out only when $|b| > 15$, i.e. over 75% of the sky, thus leaving a total of 3 million observable galaxies. It must also be noted that the readnoise appears to dominate the total error budget, and that therefore the adoption of a larger sample

size in the ASM 1 could result in a much higher number of detected galaxies.

A typical, intrinsically bright, galaxy from the "Third Reference Catalogue of Bright Galaxies" (de Vaucouleurs et al. 1991, RC3 in the following) has an absolute magnitude of $M_B = -19$, according to Figure 2 in Impey and Bothun 1997, which using the average color index $B-I = 2.0$ obtained for bright galaxies by Prugniel and Héraudeau 1998 gives $M_I = -21$. Under this conservative assumption, for $I_{det} = 17$ mag we obtain a distance modulus of $(m-M)_{det} = 38$ mag and therefore a distance of $d_{det} = 400$ Mpc or a redshift of $z_{det} \simeq 0.1$, using for the Hubble constant the value of $H_0 = 71$ Km/s Mpc recently obtained by Mould et al. 2000. Clearly, since the RC3 only contains galaxies brighter than $B \simeq 15.5$, i.e. on average $I \simeq 13.5$, most detected galaxies will be intrinsically fainter, and therefore lie correspondingly farther, than assumed above, thus increasing the horizon of galaxy observations.

These numbers were derived under a number of assumptions, both optimistic and pessimistic. On the whole this gives a rather large uncertainty on the final numbers, but probably not more than a factor of two in each direction, i.e. from 1.5 to 6 million galaxies. Note, however, that following a different line of reasoning based on the analysis of several HST MDS fields, Lindegren 2000 obtained a total number of 6 million detected galaxies, with an estimated uncertainty of about three in each direction. This remarkable agreement between estimations obtained with different methods confirms the reliability of the combination of statistical modelling and numerical siulation in mission planning.

5.7 Expected Accuracy in Surface Photometry

Whenever a significant signal is detected in a sky region in the ASM 1, this should be observed in the BBPs with a suitable sample size and the corresponding data should be sent to the ground for data analysis. A possible way to combine the observations obtained during different scans of the same sky region into a two-dimensional image will be described in Chapter 6. Here, proceeding much like it was done in the previous Section for detection, only an estimation of the accuracy achievable in surface photometry at different surface brightness levels will be derived as function of the adopted sample size.

The baseline sample size for the observation of stars in the Astro 1 and Astro 2 BBPs is of 1×8 and 6×8 pixels, respectively. These must be considered as starting points for the choice of the sample size for galaxy observation, since it would be desirable to use the same size to observe both stars and galaxies. These two sample sizes, however, are very elongated across-scan, and this could result in problems when trying to reconstruct the two-dimensional morphology of galaxies. Besides, the sample size can be reduced in the across-scan, but not in the along-scan, direction without upsetting the TDI process. Accordingly, four sample sizes of 6×8, 6×4, 6×2, and 1×8 pixels were considered. Note that the same sample sizes will be used in Chapters 6 and 7 to numerically simulate galaxy observations as they could be obtained by GAIA.

The expected all-mission accuracy in surface photometry in the g band $\sigma_{mag,g}$ for these sample sizes and for different levels of surface brightness is given in Table 5.6, where a total number of 75 scans was assumed. Note that the g band is very similar to the V

Table 5.6: All-Mission Accuracy in Galaxy Surface Photometry. Expected all-mission standard error in magnitudes $\sigma_{mag,g}$ in galaxy surface photometry in the g band for different values of sample size and I-band average surface brightness within the sample $<\mu>_{sam}$, according to Equation 5.6 and assuming a total number of 75 scans. $\sigma_{mag,g}$ expressed in magnitudes, sample size in pixels, $<\mu>_{sam}$ in mag/arcsec^2.

$\sigma_{mag,g}$		Sample Size			
		6×8	6×4	6×2	1×8
	18.00	0.024769	0.046959	0.10659	0.18314
	19.00	0.050259	0.105942	0.25750	0.45118
$<\mu>_{sam}$	20.00	0.112068	0.253102	0.63627	1.12433
	21.00	0.266003	0.622273	1.58759	2.81517
	22.00	0.652025	1.54938	3.97714	7.06232
	23.00	1.62138	3.87809	9.97940	17.7307

band (see Table 2.1) and that an average number of 75 scans is expected for each Astro from a 5-year mission (see Figure 2.4). From the tabulated values it appears that the surface brightness limit for surface photometry accurate at a given level increases with the sample size by about one magnitude per different sample size. For instance, the limit for surface photometry accurate to within 0.2 mag/arcsec^2 is about 21.0 mag/arcsec^2 for 6×8 pixels/sample, 20.0 mag/arcsec^2 for 6×4 pixels/sample and so on.

The surface brightness at the effective radius of a galaxy of $I_{det} = 17$ is typically about $\mu_I = 22.0$ mag/arcsec^2 for E galaxies and $\mu_I = 21.5$ mag/arcsec^2 for D galaxies, according to Table 4.5. Comparing these values with those in Table 5.6, it appears that a sample size of 6×8 or 6×4 pixels/sample is preferable in order to obtain multi-color surface photometry in the innermost regions, i.e. down to the effective radius, of most galaxies brighter than $I_{det} = 17$. This in turn suggests to carry out galaxy observations in the Astro 2, where both a sample size of 6×8 and 6×4 pixels could be adopted without upsetting the TDI process for star observations. Note, however, that while an increase in the sample size obviously increases the photometric accuracy, on the other hand this leads to a decrease in the achievable angular resolution. The previous considerations will therefore be combined with those developed in Chapters 6 and 7 to establish the best trade-off between photometric accuracy and angular resolution.

5.8 Expected Telemetry Rate

As it was mentioned at various times, the amount of data one would ideally like the GAIA satellite to transmit to the ground is far larger than the available telemetry rate. Any observing proposal must therefore provide an estimate of the necessary effort in terms of telemetry rate which is implied by the suggested observations.

Generally speaking, we would like to observe galaxies in all sky areas that trigger the detection and from a suitable surrounding area, and to send the corresponding data to the ground. Such a surrounding area could be defined as composed by all the square

areas of a given side that are adjacent to the areas where an excess surface brightness has been detected, as it is shown in Figure 5.3, where a side of 2 arcsec was chosen for illustrative purposes.
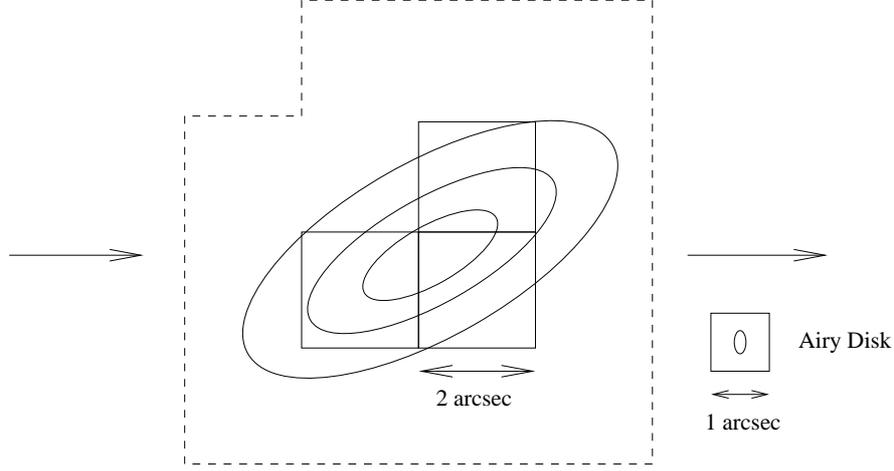
Figure 5.3: Galaxy Data Transmission. The solid squares indicate the sky areas where an excess surface brightness has been detected, while the dashed line delimits the sky area from which galaxy data are transmitted to the ground. Right arrows indicate the satellite scan direction. The GAIA Astro Airy Disk is also shown to illustrate the high resolution achievable in galaxy observations.

The outlined observation strategy appears to satisfactorily cover the galaxy regions whose surface brightness is just below the detection limit, thus allowing to study the galaxy morphology in greater detail. In the following, however, in order to estimate the telemetry rate required for galaxy observations, a few simplifying assumptions will be made. It is assumed that data are transmitted from circular areas centered on the galaxy center, and that the radius r_t of this areas can be written as

$$r_t = r_e + \Delta r \; , \tag{5.7}$$

where Δr is a positive constant. The overall sky area Ω_t within a radius r_t for all galaxies brighter than I could then be used as a rough estimate of the overall sky area from which data should be transmitted to the ground in order to observe all galaxies down to this magnitude. Neglecting the possible superposition on the sky between different galaxies, which is correct as far as the sky area in consideration is reasonably small, Ω_t can be written as

$$\Omega_t(I) = \Omega_{sky} \int_{-\infty}^{I} \pi \, r_t^2 \, N \, dI' = \pi \, \Omega_{sky} \int_{-\infty}^{I} r_e^2 \, N \, dI' + 2\pi \, \Delta r \, \Omega_{sky} \int_{-\infty}^{I} r_e \, N \, dI' +$$

$$+ \pi \, (\Delta r)^2 \, \Omega_{sky} \int_{-\infty}^{I} N \, dI' = \Omega_e(I) + 2\pi \, \Delta r \, \Omega_{sky} \int_{-\infty}^{I} r_e \, N \, dI' + \pi \, (\Delta r)^2 \, \Omega_{sky} \, N_c(I) \; , \tag{5.8}$$

Numerical values of Ω_t / Ω_{sky} for different values of I and Δr are given in Table 5.7.

Table 5.7: Fraction of sky Ω_t/Ω_{sky} within a radius $r_t = r_e + \Delta r$ for all galaxies brighter than I for some values of I and Δr. Ω_t/Ω_{sky} in 10^{-6} sky, Δr in arcsec and I in magnitudes. Values calculated via Newton integration (see Section 9.7 in Press et al. 1996) of Equation 5.8.

$\frac{\Omega_t}{\Omega_{sky}}$		Δr				
		2	4	6	8	10
	10	5.9559699	6.4369017	6.9178336	7.3987655	7.8796973
	11	13.015628	14.507042	15.998455	17.489869	18.981282
	12	28.234900	32.617360	36.999820	41.382281	45.764741
	13	62.711973	74.930181	87.148388	99.366598	111.58480
	14	147.90940	180.29082	212.67225	245.05368	277.43510
I	15	379.93125	461.71573	543.50020	625.28469	707.06916
	16	1059.6399	1257.0964	1454.5528	1652.0093	1849.4657
	17	3118.8339	3576.2198	4033.6057	4490.9917	4948.3775
	18	9354.6744	10375.459	11396.243	12417.028	13437.812
	19	27814.818	30020.274	32225.728	34431.184	36636.639
	20	80550.210	85187.870	89825.529	94463.189	99100.849

From these it can be concluded that, with $\Delta r = 6$ arcsec, all galaxies brighter than the detection limit $I_{det} = 17$ would cover about 0.4% of the sky. The telemetry rate required to cover such a sky area can be derived as function of the adopted sample size under the assumptions that each sample value is coded into 16 bits and that a loss-less compression factor of 16/5 can be applied before transmission. The assumption of such a relatively high compression factor is deemed realistic, since most sample values will be low, thus allowing a very efficient compression.

Under these assumptions, the required telemetry rate after compression TR for galaxy observations can be estimated as

$$TR = \sin\phi_{lim}\, B\, \frac{\Omega_t}{\Omega_{sky}}\, \frac{v_s\, h_{fov}}{A_{sam}}\, BPS \;, \tag{5.9}$$

where ϕ_{lim} is the chosen lower limit in Galactic latitude for galaxy observation ($\sin\phi_{lim}$ is the fraction of sky where the absolute value of the Galactic latitude b is greater than ϕ), B the number of photometric bands in which observations will be carried out, v_s the scan velocity of the satellite, h_{fov} the height of the field of view, A_{sam} the sample size and BPS indicated the number of bits per sample after compression. Values of TR are given in Table 5.8 for the presently assumed values of the relevant parameters.

Table 5.8: Telemetry rate after compression required for galaxy observations as function of the sample size. Values calculated from Equation 5.9, where $\phi_{lim} = 15$ deg, $B = 5$, $\Omega_t/\Omega_{sky} = 0.004$ and 5 bits/sample after compression have been assumed. Sample size expressed in pixels, telemetry rate in kbits/s.

6×8	6×4	6×2	1×8
108	217	433	650

As mentioned in Section 2.6, a total telemetry rate of about 1 Mbit/s after compression is presently foreseen for GAIA. From Table 5.8, it appears that the observation of galaxies, carried out with 6×8 or 6×4 pixels/sample, as suggested in Section 5.7, would require a significant, but probably not unreasonable, part of the total telemetry. On the other hand, observing the assumed fraction of the sky with a smaller sample size would require a prohibitively high telemetry rate.

Chapter 6

Simulation and Stacking of GAIA Observations

The simulation of observations and the testing of data analysis procedures on simulated observations is a necessary step in the feasibility studies of a scientific space mission. This is because in most cases the economic effort required by a space mission can only be justified if unprecedented measurement capabilities are to be expected, and as a consequence one usually cannot use real images obtained with different instrumentation for these purposes. This is the case, e.g., for the detection and observation of stars in GAIA Astros, in which case a great effort has been devoted to the generation of synthetic images for use in numerical simulations. Basically, synthetic images are considered useful for testing because a wide variety of conditions can be simulated that could be difficult to obtain from real images, and because images of a given field in several photometric bands can be generated, thus providing simultaneous multi-band photometry, as it will be the case for GAIA.

In the case of galaxy observations, however, the wide range of morphologies, structures and surface brightnesses displayed by galaxies makes synthetic objects, e.g. galaxies from IRAF, not realistic, and the use of suitable real fields are preferable. In this Chapter procedures for the simulation of GAIA galaxy observations and for their superposition into an all-mission "flux map" are described. The simulation of observations is based on HST WFPC2 images and on realistic assumptions about GAIA BBP performance with respect to electron count rate, PSF and noise. The superposition, or stacking, of simulated observations into a flux map is then carried out through a procedure that mirrors the one used in the simulation of observations.

6.1   HST WFPC2 images

The fundamental requirements real images must meet in order to be useful for the purpose of simulation of GAIA observations are those of being optical, high-exposure-time, high-angular-resolution, large-field-of-view images. The need for optical images is easily understood, and the large field of view is required to simulate the observation

of a reasonable portion of a galaxy. On the other hand, the need for high, specifically higher than GAIA's, angular resolution and exposure time originates from the desire of having at disposal ideal images, i.e. images that for our purposes may be assumed to represent the "real sky". These stringent requirements presently leave little choice but to use images obtained with the Wide Field and Planetary Camera 2 (WFPC2) onboard the Hubble Space Telescope (HST).

The WFPC2 (see Holtzman et al. 1995a, Voit 1997 and Biretta et al. 1996) is a two-dimensional imaging device covering a wavelength range from Lyman-α to about 1 μm. Built as a replacement for the original Wide Field and Planetary Camera (WF/PC), it includes built-in correction for the spherical aberration of the HST Optical Telescope Assembly (OTA), and was installed during the first HST servicing mission in December 1993.
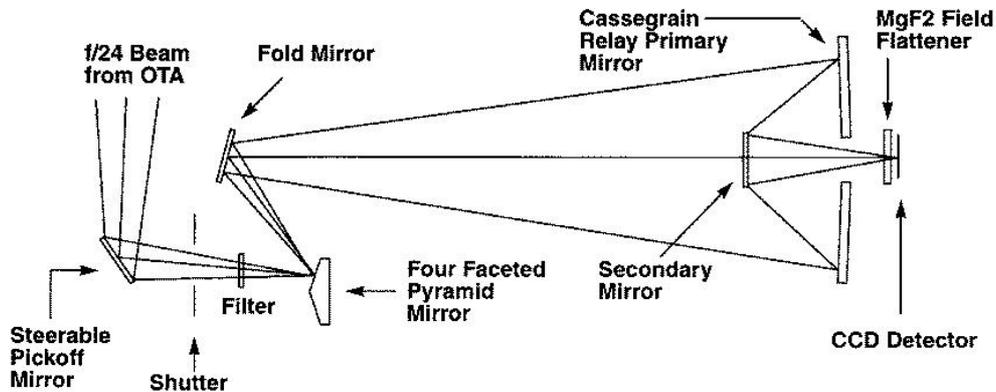
Figure 6.1: Optical Arrangement of HST WFPC2. From Voit 1997.

A schematic of WFPC2 optical arrangement is shown in Figure 6.1. The WFPC2 field of view is located at the center of HST focal plane. The central portion of the $f/24$ beam coming from the OTA is intercepted by a steerable pick-off mirror and is diverted into the WFPC2 proper. The beam then passes through a shutter and the filter assembly to fall onto a four-faceted pyramid mirror located at the aberrated OTA focus, which divides the image into four parts. After leaving the pyramid mirror, each quarter of the full field of view is relayed by an optical flat to a Cassegrain relay that forms a second image on a 800×800 pixel CCD. Each detector is housed in a cell sealed by a MgF$_2$ window, serving as a field flattener. The wavefront aberrations introduced by the OTA are thus corrected by introducing an equal but opposite error in each of the four Cassegrain relays. The resulting PSF is quite close to that originally expected for WF/PC. The four cameras have essentially identical optics, but one of these works at a smaller image scale. The Planetary Camera (PC) has a focal ratio of $f/12.9$ and operates at an image scale of 45.5 mas/pixel, whereas the three Wide Field Cameras (WFCs) have a focal ratio of $f/28.3$ and operate at 96.6 mas/pixel. The field of view is thus 36.4 and 77.28 arcsec in side for PC and WFCs respectively.

The HST WFPC2 data used in the simulations were retrieved from the Hubble Data

Archive (HDA) (`http://archive.stsci.edu`) of the Space Telescope Science Institute (STScI). Only the HDA calibrated data, i.e. the data processed through the so called calibration pipeline carried out at the STScI, were used. These are affected by problems common to any astronomical instrument, e.g. limited throughput, not point-like PSF, cosmic ray hits and noise, as well as by the instrument's peculiar problems, described by Holtzman et al. 1995a and Biretta et al. 1996. It must be emphasized that no correction for these effects was applied on the HDA calibrated data before carrying out the simulations. As already noted, it was thus assumed that the calibrated data faithfully represented the "real sky". In other words the WFPC2 images were taken to be ideal. Accordingly, in Chapter 7 the goodness of the results expected from GAIA galaxy observations will be evaluated on the basis of a comparison between HST real data and GAIA simulated data. The reason for this simplified approach was that we were mainly interested in simulating how GAIA would reproduce a given realistic sky image containing lots of subarcsec details, rather than in deriving with the highest accuracy the real properties a field imaged by WFPC2. Note, however, that in Subsections 6.2.2 and 6.2.3 it is shown that the assumption of ideal WFPC2 images is essentially correct as far as PSF and noise are concerned.

6.2 GAIA BBP vs HST WFPC2

As a first step a comparison between HST WFPC2 on-orbit performance and GAIA Astro BBP specifications as they are presently foreseen was carried out. This comparison mainly focused on the two instruments' sensitivity, angular resolution and noise level.

6.2.1 Photoelectron Count Rate

The sensitivity of an instrument employing a CCD as a detector can be conveniently defined as the number of detected electrons per second, or electron count rate, generated by a given reference source.

As far as WFPC2 is concerned, the photometric calibration obtained by Holtzman et al. 1995b and the A/D gains given by Biretta et al. 1996 can be combined to estimate the photoelectron count rates in different WFPC2 bands generated by a source of given standard magnitude and color indices. Values thus calculated for WFPC2 bands approximately corresponding to the $BVRI$ bands are given in Table 6.1 for a source of $I = 15$ and typical galaxy color indices given by Prugniel and Héraudeau 1998.

As for the BBP, expected photoelectron count rates for stars of different spectral types and in different photometric bands were provided by Lennart Lindegren in a private communication. The rates expected in the $fgriz$ bands (see Subsection 2.4.1) from a G2V star of $I = 15$, whose spectrum was found to satisfactorily approximate the spectrum of a typical galaxy in Section 5.4, are listed in Table 6.1.

From Table 6.1 it appears that the sensitivity of GAIA BBP is generally slightly higher that that of HST WFPC2, notwithstanding the much bigger aperture of HST, but this can be explained by the seven reflections taking place in HST OTA (2) and WFPC2 (5), and to a minor extent by the higher quantum efficiency of GAIA CCDs.

Table 6.1: HST WFPC2 and GAIA BBP Electron Count Rates. Rates generated by an $I = 15$ star are given for WFPC2 and BBP bands approximately corresponding to the $BVRI$ bands, and are grouped accordingly. Rates expressed in e^-/s. .

B		V		R		I	
F439W	F450W	F555W	F606W	F675W	F702W	F814W	
236	851	2396	4712	2713	4085	3249	
f		g		r		i	z
3984		4096		3892		2866	1541

Specifically, the two instruments are of nearly equal sensitivity in the V, R and I bands, even if in the case of GAIA BBP the latter band is divided into two bands of smaller bandwidth, whereas GAIA BBP is substantially more sensitive in the B band. The correspondences between HST WFPC2 and GAIA BBP bands outlined in Table 6.1 could in principle be used in the simulation of GAIA observations to convert WFPC2 electron counts into the correspondent electron counts for the BBP, but in practice a different approach is followed, assuming equal sensitivity for the two instruments. Such a very conservative assumption is believed to reinforce the validity of the obtained results in case the presently assumed specifications for the GAIA payload should change resulting in lower electron count rates than it is now foreseen.

6.2.2   Point Spread Function

The combined effects of the aberrations introduced in the wavefront by the instrumentation and by environmental effects such as, for ground-based observations, the atmospheric turbulence, are conveniently described in terms of the global *Point Spread Function* (PSF) $P(\mathbf{d})$, giving the probability density that a photon will hit the imaging device at a point that is displaced by a vector $\mathbf{d}$ from where it would have hit it in the absence of aberrations. If the true surface brightness distribution of an object is $\Sigma_t(\mathbf{r})$, then the observed surface brightness distribution will be

$$\Sigma_{obs}(\mathbf{r}) = \int P(\mathbf{r} - \mathbf{r}') \, \Sigma_t(\mathbf{r}') \, \mathrm{d}^2\mathbf{r}' = [P \otimes \Sigma_t] \, (\mathbf{r}) \qquad (6.1)$$

where $\otimes$ indicates the convolution operator. This latter notation is convenient e.g. when simulating the blurring of a "true" image due to a given PSF, as it will be done in the simulation of GAIA observations in Section 6.3, since one can then exploit the fact that the Fourier transform of the convolution of two functions equals the product of the Fourier transforms of the two functions. Roughly speaking, the "width" of the PSF, characterized e.g. by its FWHM or by the diameter enclosing a given percentage of the total brighness, thus describes the angular resolution achieved in an observation.

As mentioned in Subsection 3.2.3, in ground-based observations obtained with telescopes of moderately large apertures, the PSF is dominated by the phenomenon of seeing, described in 1.1. Conversely, in space observations the PSF is essentially due to instrumental aberrations only, and the careful polishing of the telescope optics may

therefore in principle yield nearly diffraction-limited images. This is almost the case for HST WFPC2, where however the image undersampling due to the large pixel area on the sky have sensible effects, but not for GAIA, where the continuous scanning of the satellite and the adopted CCD binning strategy substantially widens the purely optical PSF.

The PSF of HST WFPC2 is accurately described by Holtzman et al. 1995a and Biretta et al. 1996. In particular, it is therein shown that when observations with the broad-band, *UBVRI*-like WFPC2 filters are made, the 50%-light diameter, i.e. the diameter of the circle enclosing 50% of the light coming from a point-like source, is about 80 and 130 mas for the PC and the WFCs respectively.

The PSF of GAIA BBP, which will be needed in the simulation of observations, was modelled and numerically calculated under realistic assumptions about the instrumental performance following Lindegren 1998a. An adaptation of a program by Lennart Lindegren written by Anthony Brown was used to calculate the PSF and output it as a fits file.

As a first step, the monochromatic optical PSF is derived, taking into account the diffraction from the telescope rectangular aperture and the aberrations of the wavefront introduced by the optical defects of the mirrors. For the latter, the Matra Marconi Space baseline assumption of primary and tertiary mirrors polished to $\lambda/30$ rms and secondary mirror polished to $\lambda/50$ rms was used. Then the monochromatic global PSF is derived by considering the pixel and sample binning, the efficiency of the charge transfer and of the Time Delay Integration, and finally the across-scan motion of the image during the scan. Here, the four sample sizes of 6×8, 6×4, 6×2 and 1×8 pixels were separately considered. Finally, the polychromatic global PSF, or PSF proper, is computed by adding up the contributions to the PSF due to light of different wavelengths, taking into account the true spectrum of the source, the telescope transmittance and the CCD response curve. Thus, the PSF for any stellar spectral type can be obtained. For our purposes, as explained in Section 5.4, the spectrum of a G2V star can be chosen as representative of the spectrum of a typical galaxy. The PSF thus obtained is also referred to as the one-scan PSF, indicating that it is the true PSF of each GAIA BBP observation. In order to model the all-mission effective PSF, i.e. the PSF of an image obtained from superposition of many observations, a set of 50 randomly distributed scan directions was generated, the one-scan PSF was accordingly rotated using bilinear interpolation and the rotated PSFs were finally summed. The result of this procedure is believed to reliably represent the all-mission effective PSF, provided that an efficient stacking strategy is devised.

The properties of the resulting PSFs are illustrated in Figures 6.2 and 6.3, showing the one-scan and 50-scan PSFs for the four sample sizes, respectively. The first plot of each row is a a contour plot of the two-dimensional PSF, with the brightest contour drawn at a surface brightness level 0.5 mag fainter than the maximum and altogether seven contours drawn at intervals of one magnitude. In the second one, the encircled energy curve of the PSF is given, whereas in the third and fourth ones the one-dimensional PSF profiles in the along-scan and across-scan direction are drawn.

Several features are easily noted in these two Figures. Generally speaking, the width
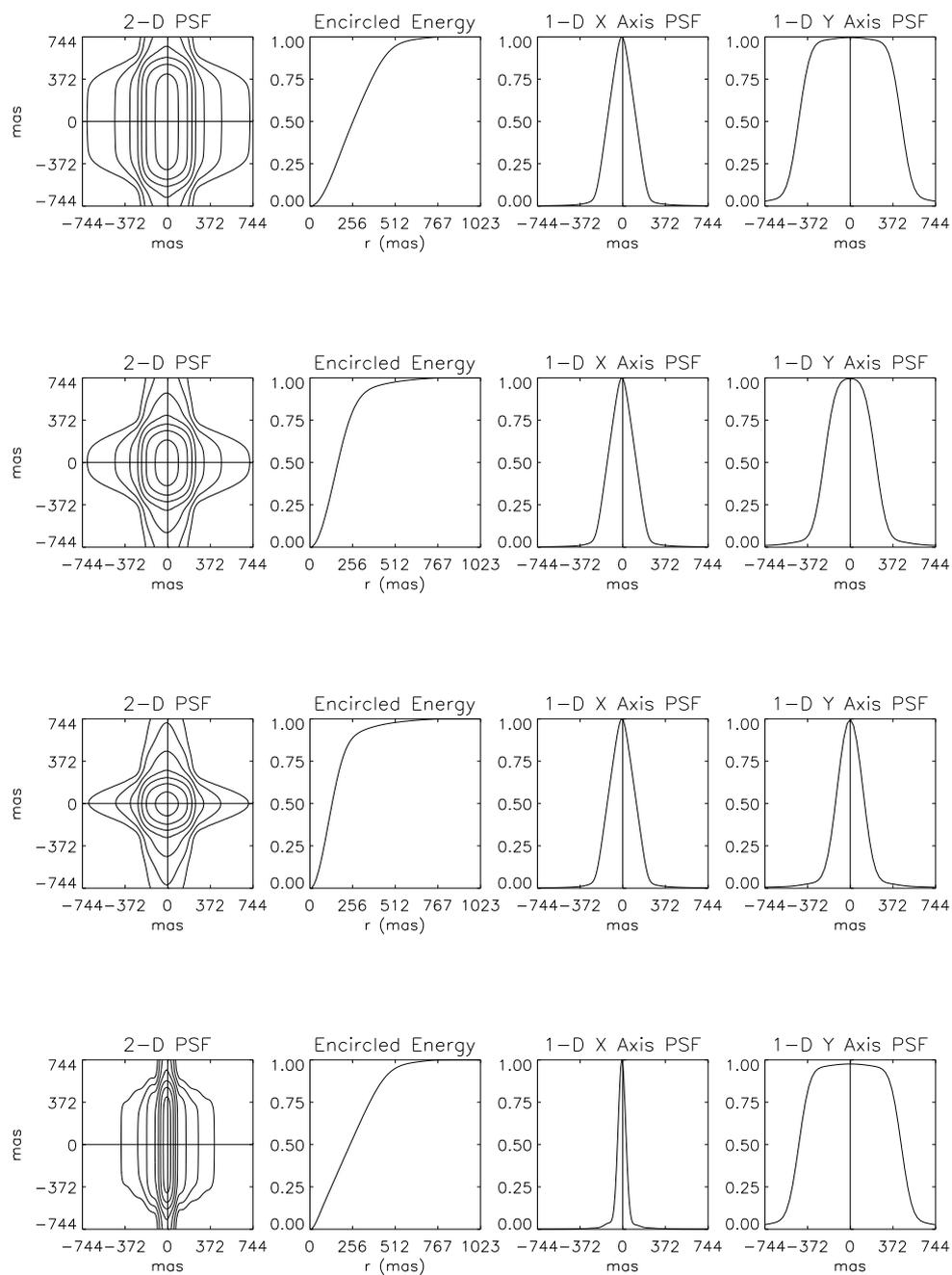
Figure 6.2: GAIA one-scan PSFs. From the top: (a) 6×8 pixels/sample, (b) 6×4, (c) 6×2, (d) 1×8. See text for details.
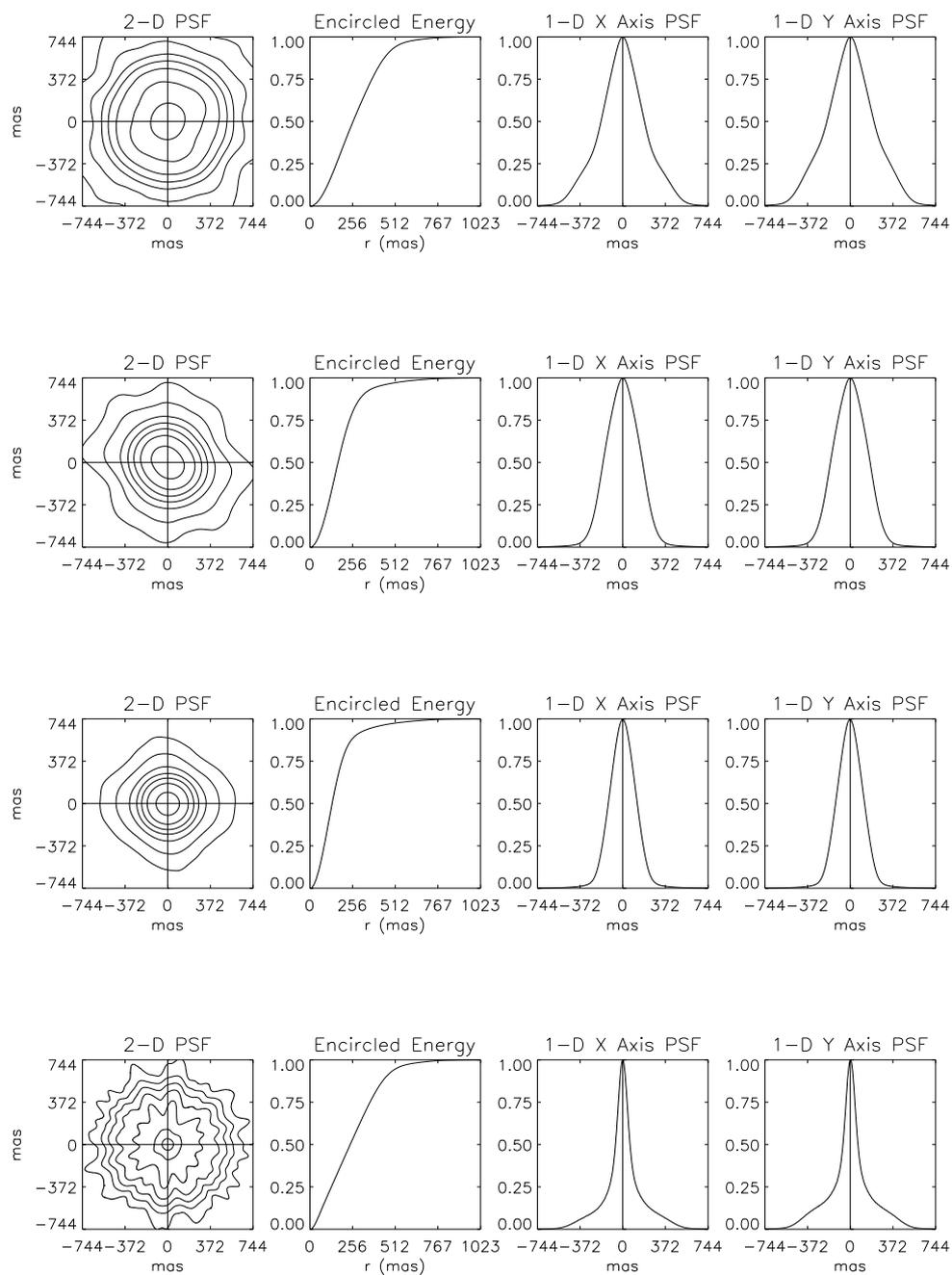
Figure 6.3: GAIA 50-scan PSFs. From the top: (a) 6×8 pixels/sample, (b) 6×4, (c) 6×2, (d) 1×8. See text for details.

of the PSFs is dominated by the sample size, and even the one-scan PSF obtained with the square sample of 6×2 pixels appears almost perfectly circular, notwithstanding the elliptical Airy Disk delivered by the telescope optics. It also appears that, owing to wave-front errors, the one-scan PSFs are not exactly centered at the point (0,0), and that the 50-scan PSFs show significant deviations from a circular shape, mostly due to random fluctuations in the scan directions. Besides, in general the encircled energy curve does not appear to depend on the number of scans.

The 50%-light diameter d_{50} and the 90%-light diameter d_{90} (i.e. the diameters of the circles enclosing 50% and 90% of the energy, respectively) of the 50-scan PSFs are given by Table 6.2 together with the FWHM, the latter given by the average of the FWHMs along the two directions.

Table 6.2: Values of d_{50}, d_{90} and FWHM for GAIA all-mission PSFs. 50%-light diameter, 90%-light diameter and FWHM of GAIA 50-scan PSFs for different sample sizes.

	d_{50}	d_{90}	FWHM
6×8	520	940	400
6×4	340	640	345
6×2	270	560	255
1×8	480	900	145

It should be noted that d_{50} and d_{90} depend significantly on the length of the sample major side but not much on the sample minor side, suggesting to use a nearly square sample to optimize the observations with respect to angular resolution. It also appears that d_{50} and the FWHM can be very different, d_{50} usually being larger than the FWHM, and it can be observed that the difference increases with the PSF asymmetry, which in turn increases with the y/x ratio of the sample size. The PSF obtained with 1×8 pixels/sample has e.g. a much smaller FWHM but not a substantially smaller d_{50} if compared with that obtained with 6×8 pixels/sample. This was to be expected, since an asymmetric PSF has relatively wider wings. However, this effect is not particularly significant for the two smaller and more symmetric sample sizes of 6×4 and 6×2 pixels.

The all-mission effective PSF obtained from simulations will most likely be slightly wider than given above, since the HST and GAIA PSFs both contribute to smear the true sky. Taking this into account, the 50%-light diameter can be estimated by means of the quadratic formula

$$d_{50,sim} = \sqrt{d_{50,HST}^2 + d_{50,GAIA}^2} \ , \tag{6.2}$$

which however gives values that do not differ much from those given in Table 6.2 for any combination of WFPC2 camera and BBP sample size.

6.2.3   Noise

Any astronomical observation is affected by different "noise" sources. These can be roughly divided into natural and artificial sources. Natural sources essentially are the

signal noise connected with the quantum nature of light, to the background noise due to the radiation coming from natural sources different from the observed object, and including in particular the sky background and the cosmic ray hits. Artificial sources include the dark noise that a detector may generate even in absence of any signal, the readnoise originating from the reading process and the non-optimal CCD performance over the focal plane.

For the purpose of our simulations, most of these sources can be neglected. For instance, due to GAIA short one-scan exposure time, the rate of cosmic ray hits will be very low, and moreover the superposition of many scans of the same sky region will average over these unlikely events. Likewise, the superposition of different scans will average over possible space or time variations in the CCD response. The effects of the sky background and of the CCD dark current will be order of magnitudes lower than the signal noise and the readnoise. On the whole, the signal noise and readnoise appear to dominate the noise budget. Accordingly, only signal noise and readnoise heve been considered in the simulations.

The signal noise is usually assumed to follow a Poisson distribution and the relative standard error in surface photometry is thus proportional to $1/\sqrt{N}$, where N is the total number of detected electrons per unit area. Since the exposure time of the WFPC2 images used in the simulations is much bigger than the one-scan GAIA exposure time, and since in Subsection 6.2.1 the electron count rate of the two instruments was found to be almost the same, it is concluded that the total number of detected electrons per unit area is much bigger in WFPC2 images than in GAIA observations, and thus that the signal noise present in WFPC2 images is negligible with respect to that introduced by GAIA.

On the other hand, the readnoise is usually assumed to follow a Gaussian distribution with zero mean and standard deviation independent from the total number of detected electrons per unit area. Accordingly, the relative standard error in surface photometry is proportional to N^{-1}. Measurements of HST WFPC2 readnoise yielded average values of about 5 e$^-$/pixel rms and 7 e$^-$/pixel rms, depending on the chosen analog-to-digital conversion gain (see Biretta et al. 1996). The readnoise levels expected in GAIA Astro CCDs for different choices of the sample size and full CCD readout was discussed in Section 5.5, and results were given in Table 5.2. The readnoise levels per pixel appear to be similar in the two cases. As discussed with reference to the signal noise, however, the important figure in comparing the two instruments' performance is the relative standard error, and for the same reasons discussed above one can conclude that the readnoise present in WFPC2 images is negligible with respect to that introduced by GAIA.

Note that all readnoise values estimated for GAIA BBP and reported in Table 5.2 were calculated assuming full CCD readout. Obviously, if this requirement is relaxed, a smaller readnoise would yield an higher accuracy in surface photometry, while still allowing to fully image most detected galaxies. For instance, according to Table 4.4, the effective radius of a typical galaxy of $I = 11$ is about 25 arcsec, meaning that under the assumption of circular symmetry the circle enclosing half its light is well within a diameter of 2 arcmin. The across-scan size of a BBP CCD is about 4 arcmin, so that for a

galaxy of this magnitude only half the CCD may be readout, thus giving a lower reading frequency and therefore a lower readnoise than that expected for full CCD readout with the same sample size. Alternatively, the sample size could be reduced giving equal reading frequency but smaller sample size, and thus higher angular resolution. Since only some 2000 galaxies out of the 3 million we expect to observe are brighter than $I = 11$, most of the time we could even readout the CCD more slowly than suggested above in order to further reduce readnoise or increase angular resolution. In so doing, during a single scan we would be able to observe only some parts (e.g. those near the center of each CCD) of brighter galaxies, which could lead to a low number of total scans for certain sky regions and as a consequence to problems in their stacking, but this could be acceptable in view of an higher accuracy in surface photometry or an higher angular resolution. Although very interesting, this possibility is however not considered in the following.

6.3   Simulation of GAIA BBP Observations

Under our assumptions, the simulation of a GAIA BBP observation on the basis of an HST WFPC2 image essentially involves translation and rotation of the original image, scaling to GAIA exposure time and rebinning into GAIA samples of HST WFPC2 electron counts, image smearing due to GAIA PSF and noise. Step by step, the procedure for the generation of a single simulated observation consists of the following steps:

1. Retrieval of HST electron counts: HST data number counts are retrieved from the fits file provided by the HDA and then converted to HST electron counts using the analog-to-digital conversion gain taken from Biretta et al. 1996.

2. Subpixeling of HST image: in order to partly recover the resolution of the HST image which would otherwise be lost due to the undersampling of the PSF, each HST pixel is considered as consisting of a mosaic of four square subpixels, "containing" one fourth of the pixel's electron counts each and whose centers are displaced from the pixel's center as shown in Figure 6.4.

3. Conversion to GAIA electron counts: GAIA electron counts for a single scan are calculated from HST electron counts by taking into account the different exposure time, and assuming the same electron count rate for the two instruments (see Subsection 6.2.1).

4. Translation and rotation of HST subpixels: since GAIA observation will in general be obtained at a different position and position angle with respect to the original HST image, once the desired observation center and scan direction have been determined the HST subpixels are translated and rotated accordingly.

5. Rebinning of HST subpixels into GAIA samples: each HST subpixel electron count is assigned to the sample containing its center.
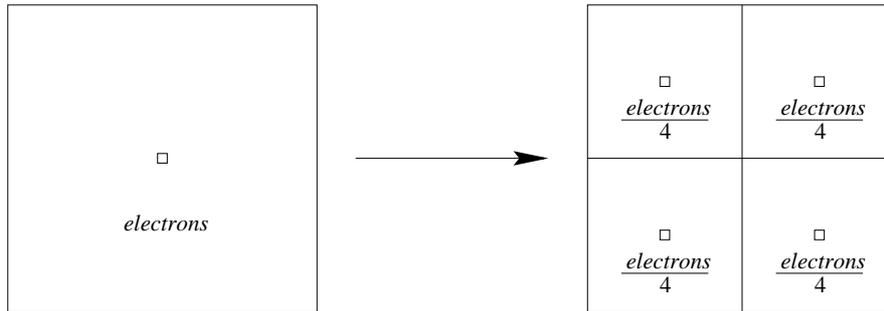
Figure 6.4: Subpixeling of HST image. The central square on the left marks the pixel's center, whereas the four squares on the right mark the subpixels' centers.

6. Convolution with GAIA PSF: the observation is convolved with the PSF described in Subsection 6.2.2. The convolution is computed using a Fourier transform technique, namely calculating the product of the Fourier transforms of the observation and the PSF and then calculating the inverse Fourier transform of the result. Note that the PSFs obtained in Subsection 6.2.2 are sampled with a step of 1/4 pixel along both directions, and therefore need to be resampled and renormalized before convolution.

7. Noise addition: to simulate signal noise we calculated a Poisson deviate of the observation, whereas to simulate readnoise we added to it a Gaussian distribution with zero mean and standard deviation equal to GAIA rms readnoise as calculated in Section 5.5.

Following this procedure, a single GAIA BBP observation is simulated. When generating a realistic all-mission set of simulated observations of a given sky region, however, one has to take into account that in general the different observations will have different centers as well as different scan directions. A set of observation centers, with coordinates in general in the range $[-\frac{ss}{2}, +\frac{ss}{2}]$, where ss is the adopted sample size along one of the two axes, and the corresponding set of scan directions, with position angles in general in the range $[0°, 360°]$, must therefore be generated. The procedure described above can then be applied to each desired combination of center and scan direction. In the simulations presented in Chapter 7 and in Appendix E, a conservative number of 50 scans was assumed. Note that this is the minimum number of times an Astro will scan any sky region during a 5-year mission, according to Figure 2.3. To a first approximation, the observation centers and scan directions can be taken as randomly distributed, but note that while the first assumption is likely to be verified fairly strictly, this may not always be the case for the second one. The consequences of possible preferred scan directions are therefore described in Section 7.5.

6.4   Stacking of GAIA BBP Observations

The general problem of the superposition, or stacking, of different images of the same sky region into a global image can be referred to as *mapping.* In the context of the GAIA mission, where the observations will generally be essentially one-dimensional, this problem is of interest not only in connection with galaxy observations, but also whenever a two-dimensional study may be required. This is the case e.g. for the observation of stars in the PSM, where a two-dimensional map of the sky region near each detected star will be needed in order to correct the brightness of the detected star for nearby, fainter disturbing stars, but also for the study of resolved binary systems. The latter issue, in particular, was already discussed by Høg et al. 1998b in the context of the construction of the Tycho 2 catalogue. In the following, *observation* will indicate the image of a given sky region obtained at a given epoch, whereas *flux map* will indicate the image resulting from the stacking of a given number of observations of the same sky region taken at different epochs.

   The stacking of a single simulated observation into a one-scan flux map was carried out through the following steps:

1. Subsampling of GAIA observation: in order to partly recover some of the resolution lost in the wide CCD binning of GAIA observation, each sample is considered as consisting of a mosaic of square subsamples of 37.2 mas side, each containing the same fraction of the sample electron count, much like it is done in Section 6.3 and shown in Figure 6.4 for the subpixeling. The value of 37.2 mas, i.e. the Astro CCD pixel size in the along scan direction, was chosen so as to be smaller than the side of the flux map elements and to be an integer submultiple of the sample size along both directions, so that each sample can be divided into an integer number of subsamples.

2. Translation and rotation of GAIA subsamples: the mosaic of subsamples is counter-translated and counter-rotated to superpose it onto the flux map, which is a mosaic of step equal to HST pixel size and half HST pixel size for PC and WFCs respectively, having the same orientation and the same center as the original HST image. Note that, due to the extremely accurate astrometric calibration that will be available at the end of the mission, the errors in the determination of the center and scan direction of the observations are negligible with respect to the sample size and the expected angular resolution.

3. Rebinning of GAIA subsamples into GAIA flux map: each GAIA subsample electron count is assigned to the flux map element containing its center.

This procedure returns a one-scan flux map. The all-mission flux map is then simply obtained by adding up all the one-scan flux maps from observations of a given sky region.

   This stacking technique, accurately preserves the total number of electrons of the original image, thus allowing an easy photometric calibration of the flux map on the basis of the HST WFPC2 photometric calibration obtained by Holtzman et al. 1995b.

A second stacking method, slightly different but much more efficient than the baseline technique described above, was also developed, consisting in assigning to a given flux map element the electron counts corresponding to the subsample nearest to its center. On the basis of visual inspection, this stacking method appears to deliver much the same results as the baseline method described above. Since the subsamples are smaller than the flux map elements, some subsamples happen not to be assigned to any flux map element, thus reducing the total number of electrons in the flux map. On average, this effect can be taken into account by multiplying the electron counts in the flux map by the ratio between the sizes of the flux map elements and the subsamples. Owing to its recent development this method has not been thoroughly tested yet, but owing to its efficiency is metioned here as a suggestion as to how the data reduction of galaxy observations could be carried out in practice. Note also that, although the possible use of drizzling, a stacking technique developed for use in the superposition of HST WFPC2 images in the Hubble Deep Field North campaign (Williams et al. 1996), was considered for use in the stacking of GAIA galaxy observations, it was finally discarded for reasons described in Appendix F. The simulated images presented in Chapter 7 and in Appendix B have therefore been derived using the previously described baseline stacking method.

Chapter 7

A Case Study: The M100 Spiral Galaxy

7.1 HST WFPC2 Image

The HST WFPC2 image on which the simulations presented in this Chapter are based is a Planetary Camera (PC, see Section 6.1) image of the central regions of the M100 spiral galaxy, obtained with a 900 s exposure with the F555W filter. This image was chosen because it contains most interesting features one would like to observe in bright galaxies: a conspicuous core, large surface brightness variations on short space scales, spiral arms and HII regions[1]. The central part of this image, namely a square of about 16 arcsec side whose flux map was reconstructed from the simulated observations, is shown in Figure 7.1.

The median surface brightness in V inside the eight circles marked by letters is given in Table 7.1. These values were calculated following the WFPC2 photometric calibration obtained by Holtzman et al. 1995b, and indicate the surface brightness range spanned by the image. Note that the median surface brightness of the whole image is $\mu_V = 19.42$ mag/arcsec^2.

Table 7.1: Characteristic values of V-band surface brightness of the HST image of M100. Median V-band surface brightness within the zones indicated in Figure 7.1, expressed in mag/arcsec^2.

Zone	a	b	c	d	e	f	g	h
Median μ_V	19.10	20.65	20.71	18.96	17.83	18.35	17.59	16.80

M100 is classified as Sc(s)I in Sandage and Bedke 1994 and the de Vaucouleurs et al. 1991 report a photoelectric total magnitude $B_T = 10.05$ and an effective radius of about

---

[1] Simulated flux maps based on HST WFPC2 PC images of three other galaxies chosen following the same criterion are presented in Appendix E, together with a bigger version of the HST image and the simulated GAIA flux map of M100 presented here.
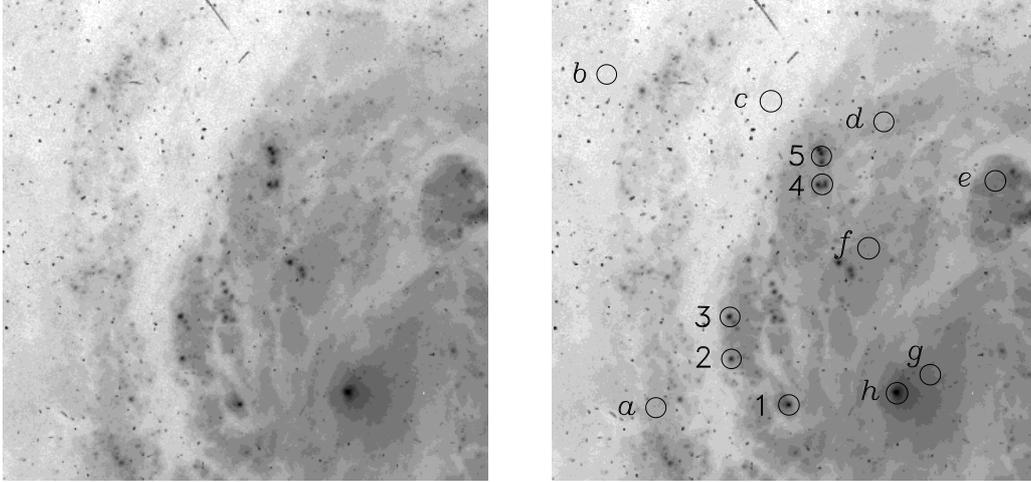
Figure 7.1: HST WFPC2 PC image of M100. Central part of a WFPC2 PC image of the spiral galaxy M100, obtained with a 900 s exposure with the F555W filter, similar to V. Encircled on the right image is the position of the eight zones used to calculate the median surface brightness in Table 7.1 (letters *a-h*) and of the five HII regions of which aperture photometry is carried out in Section 7.7 (numbers 1-5). The image side is about 16 arcsec and the circles have a diameter of about 0.7 arcsec.

104 arcsec, meaning that the sky region shown in Figure 7.1 covers its very central parts only.

7.2   GAIA BBP Flux Maps

The flux maps obtained with different sample sizes from stacking of 50 simulated observations, i.e. with an effective total exposure time of 43.09 s, are shown in Figure 7.2. Not surprisingly, flux maps obtained with bigger sample sizes are smoother, whereas those obtained with smaller sample sizes show a conspicuous lumpiness. The increasing lumpiness is to be ascribed both to the improvement of the angular resolution resulting from the "thinning" of the PSF and to the increase of the readnoise due to the higher reading frequency which is required in order to read the CCD with a smaller sample size. As a matter of fact, even if, as far as bright structures are concerned, the angular resolution appears to improve as the sample size decreases, with a sample of 1×8 pixels faint features almost disappear, swamped into the readnoise. As already noted in Chapter 5, a trade-off between the angular resolution and the accuracy in surface photometry must be established.
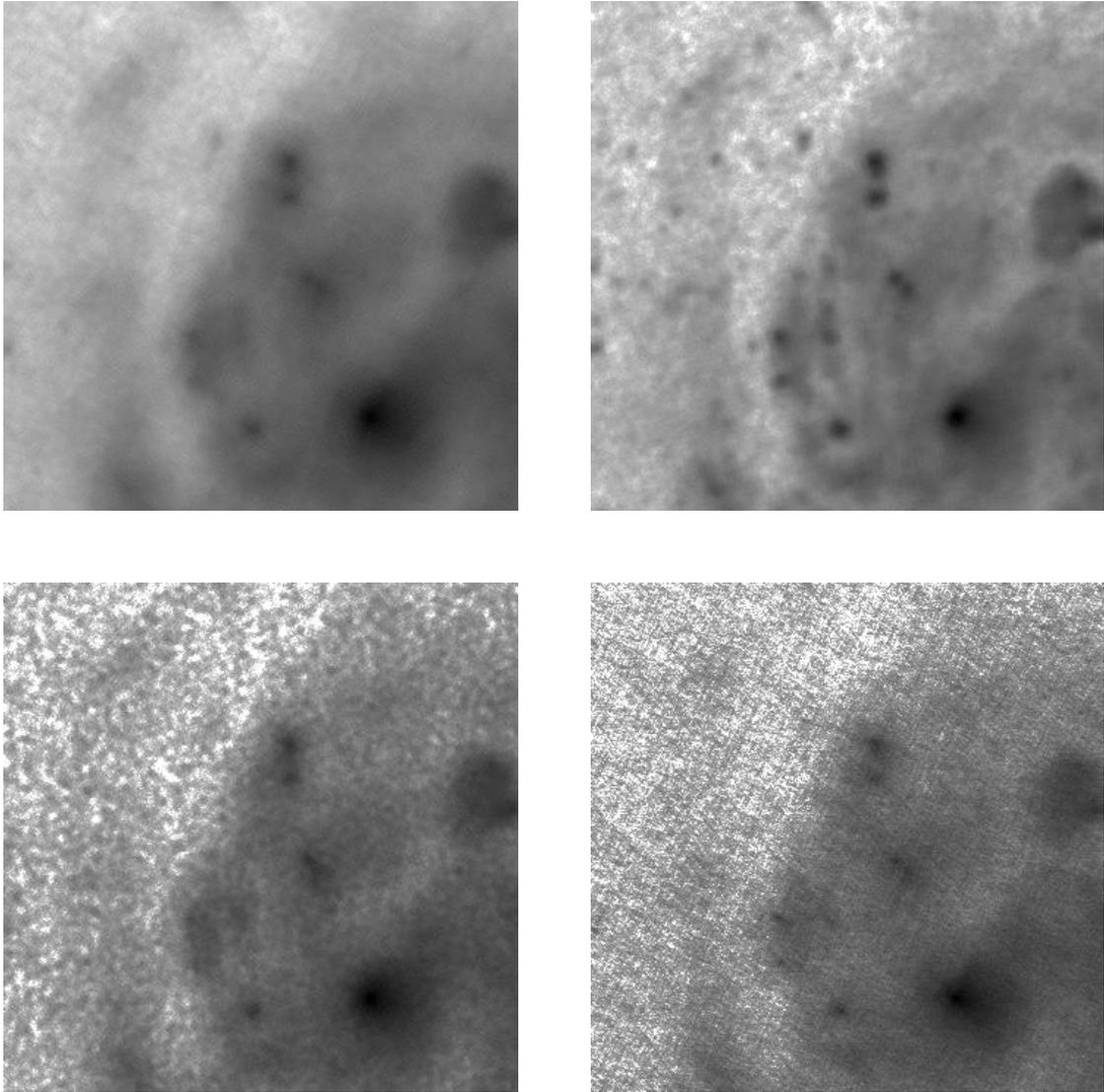
Figure 7.2: GAIA BBP flux maps of M100. BBP flux maps reconstructed from 50 simulated observations, i.e. with an effective total exposure time of 43.09 s, for different sample sizes. Upper row: 6×8 and 6×4 pixels/sample. Lower row: 6×2 and 1×8 pixels/sample. The side of each flux map is about 16 arcsec.

7.3 Angular Resolution of GAIA BBP Flux Maps

The angular resolution achievable in flux maps obtained with different sample sizes is better illustrated in Figure 7.3, where two HII regions with a separation of about 0.5 arcsec near the center of the flux maps are shown. The increase of angular resolution with the decrease in the sample size can now be clearly seen, just as the increase in the
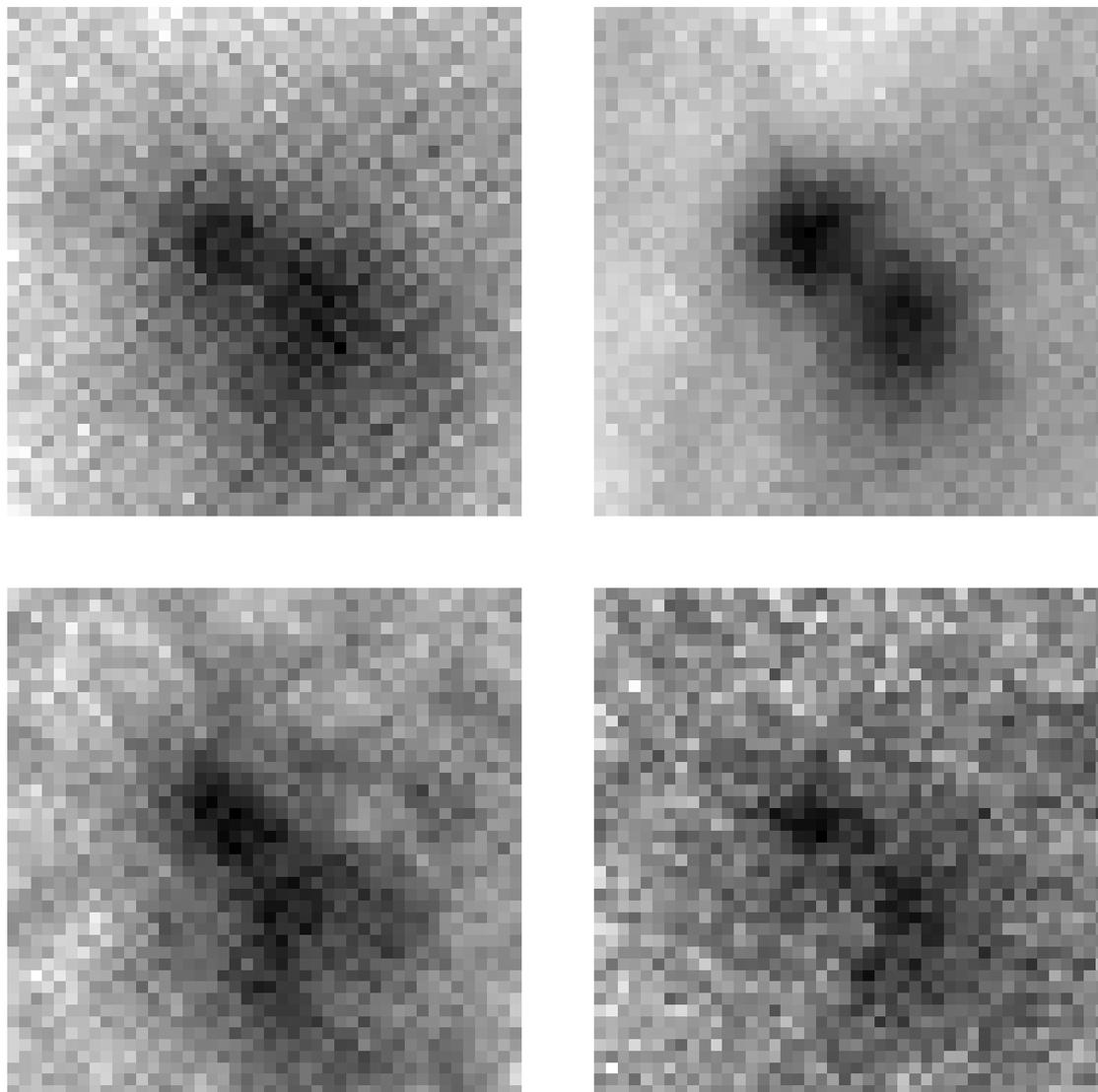
Figure 7.3: Angular resolution of GAIA BBP flux maps of M100. A part near the center of GAIA BBP flux maps of M100 shown in Figure 7.2, showing two HII regions with a separation of about 0.5 arcsec. Upper row: 6×8 and 6×4 pixels/sample. Lower row: 6×2 and 1×8 pixels/sample. The side of each image is about 2 arcsec.

noise in the fainter surroundings of the HII regions. It appears that an overall resolution of about 0.4 arcsec would be obtained with a sample size of 6×4 pixels. Such an angular resolution corresponds to that of an image obtained with an excellent large ground-based telescope during the short times of superb seeing. The best images obtained by the ESO Very Large Telescope have just about this small stellar image size. Since the advantage of observing with such a sample size has been already variously demonstrated in Chapter 5, this is the only sample size considered in the following.

7.4   Angular Resolution and Number of Scans

The number of observations stacked into a flux map, or number of scans for short, is clearly a critical factor for the quality of the resulting flux map. The improvement of angular resolution due to the increase in the number of scans is illustrated in Figure 7.4, showing the same part of the flux maps as in Figure 7.3 as it is seen in a single observation and as it is reconstructed from 10, 20 and 50 simulated observations.
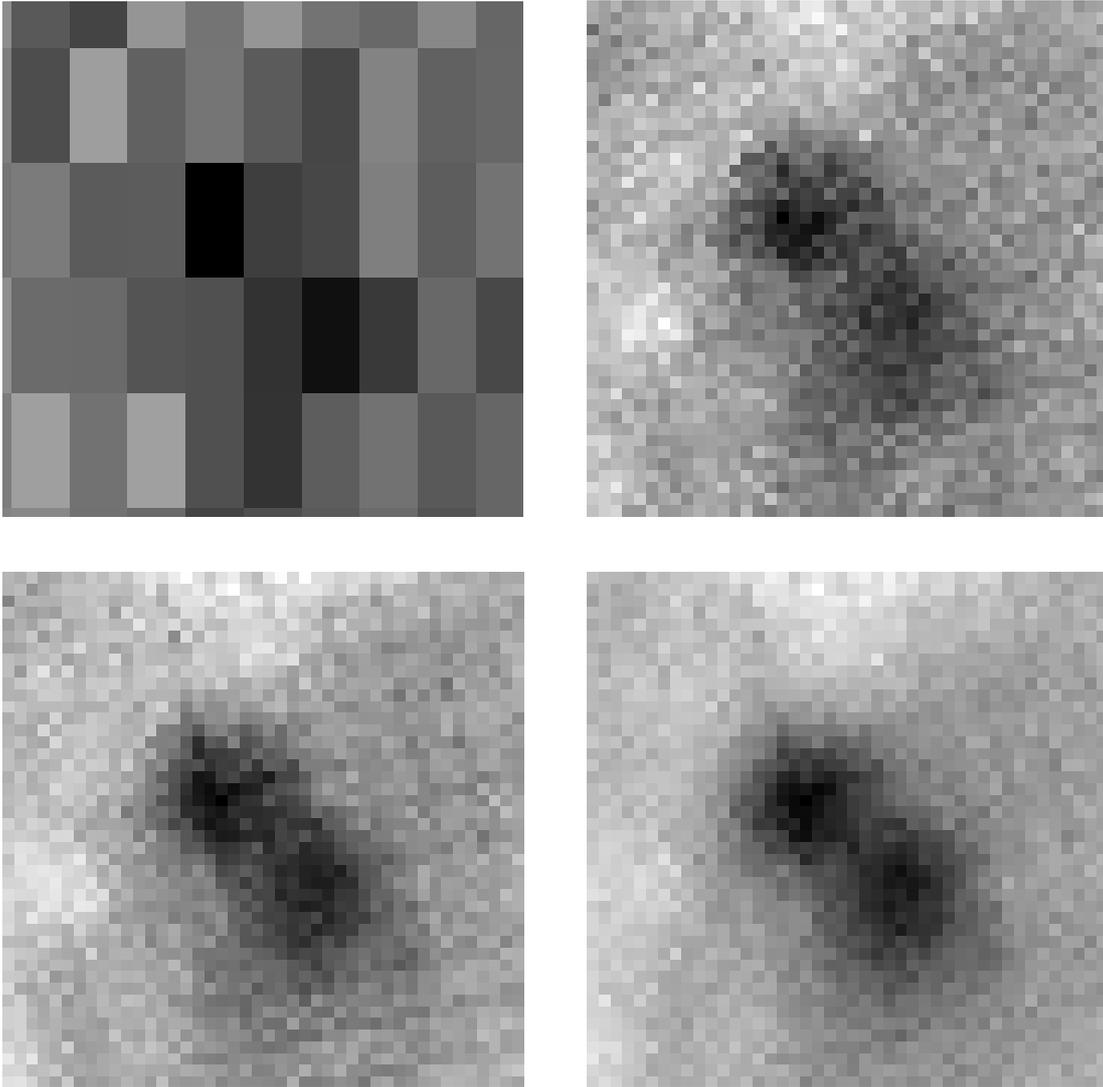
Figure 7.4: Number of scans and angular resolution of GAIA BBP flux maps. The four images show the same sky region as in Figure 7.3. The upper left image shows a single observation obtained with 6×4 pixels/sample, whereas the upper right, lower left and lower right images show a flux map reconstructed from 10, 20 and 50 simulated observations, respectively, with the same sample size. The side of each image is about 2 arcsec.

Even if the two HII regions are better resolved in the 50-scan flux map, on the whole, these images show that, at least as far as bright structures are concerned, the highest resolution allowed by GAIA PSF could be achieved with a number of scans substantially smaller than the 50 presently assumed. On the other hand, the decrease in the number of scans would obviously have a stronger impact on fainter features.

7.5   Angular Resolution and Non-Random Scan Directions

An important issue is also how a non-random set of scan directions, in which some position angles appear much more frequently than others, could affect the general appearance, and particularly the angular resolution, of flux maps. In particular, since a sample of 6×4 pixels is rectangular with major side in the across-scan direction, the presence of a preferred scan direction in principle implies the elongation of the effective PSF, and therefore the loss of resolution, perpendicularly to this direction. Obviously the problem increases in size with the PSF asymmetry, and Figure 7.5 shows that for a sample size of 6×4 pixels its effects are essentially negligible in the case of scan directions randomly distributed in the intervals $[0°, 45°] \cup [90°, 135°]$ or $[0°, 90°]$, but not so when the interval is reduced to $[0°, 45°]$, in which case the two HII regions show an increased elongation. This latter case is however an extreme one, which is not likely to occur in practice.

7.6   Accuracy in Surface Photometry

As a verification of the simulation procedure, and to roughly estimate the accuracy in surface photmetry of the flux maps, a comparison between the surface brightness values in HST original image and in GAIA simulated flux map was carried out. In order to do so, the median value of the residuals between HST WFPC2 electron counts and simulated GAIA BBP electron counts were computed taking into account the different exposure time of the two images. The value thus obtained can then be compared with the accuracy in surface photometry expected *a priori* from flux maps, as it was derived in Section 5.7 on the basis of statistical considerations.

Following this idea, a median error of 0.15 mag/arcsec^2 is derived from the comparison of HST data with GAIA simulated data. Now, remembering that the median V-band surface brightness of the HST image is 19.42 mag/arcsec^2, the expected standard error in surface photometry at this surface brightness level can be calculated as indicated in Section 5.7, thus obtaining 0.17 mag/arcsec^2, very close to the value obtained from simulations. This good agreement further demonstrates the convenience of statistical formulae for use in the preliminary instrument design and mission planning, while it validates the results of simulations. Note that in this simple treatment the error originating from the subtraction of the sky background was not considered, but it is believed (see Section 5.5 that this would yield an error much lower than that introduced by readnoise, so that the calculation is essentially correct. Note also how the *a posteriori* accuracy in surface photometry obtained with 6×4 pixels/sample compares favourably
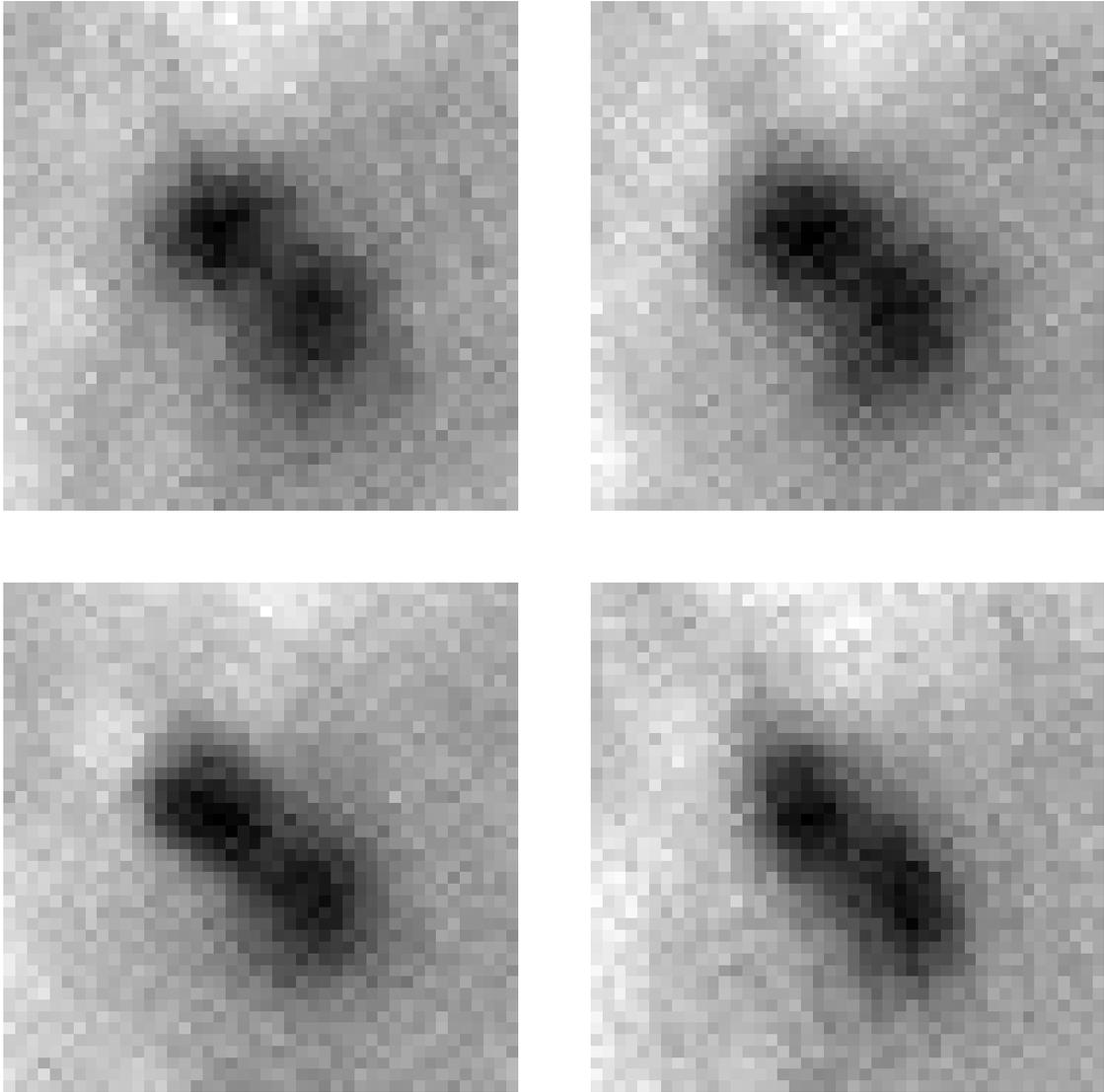
Figure 7.5: Non-random scan directions and angular resolution of GAIA BBP flux maps. The two images show the same sky region as in Figures 7.3 and 7.4, but the flux maps are here reconstructed from 50 simulated observations with non-random scan directions. The sample size is 6×4 pixels in all cases but the scan directions are randomly distributed in the intervals: $[0°, 360°]$ and $[0°, 45°] \cup [90°, 135°]$ for the upper row; $[0°, 90°]$ and $[0°, 45°]$ for the lower row. Only in the last case the image distortion with respect to the upper left image is not negligible. The side of each image is about 2 arcsec.

with that obtained with other sample sizes, as shown by Table 7.2. The apparently contradictory lower accuracy obtained with 6×8 pixels/sample can be understood as

originating from the smearing of bright features due to the wider PSF, whereas the decrease in accuracy for sample sizes smaller than 6×4 pixels is due to the increase in the readnoise.

Table 7.2: Accuracy in surface photometry estimated from simulations. Median error in V-band surface photometry of GAIA simulated flux map data with respect to HST data for different sample sizes. Sample size expressed in pixels, median error in mag/arcsec^2.

6×8	6×4	6×2	1×8
0.190	0.149	0.249	0.311

7.7 Accuracy in Aperture Photometry

As a further verification, aperture photometry of the five HII regions shown in Figure 7.1 was carried out on the HST data as well as on GAIA simulated flux map data obtained by stacking of 50 simulated observations with 6×4 pixels/sample. The center of the HII regions was determined by visual inspection, the signal counts inside a radius of 0.5 arcsec were summed and a median background calculated inside an annulus of radii 0.5 arcsec and 2 arcsec was subtracted. In order to take into account the different exposure time of the two images, the electron counts obtained from GAIA flux maps were multiplied by the ratio between the exposure time of the HST original image (900 s) and the effective total exposure time of a flux map reconstructed from 50 observations (43.09 s).

Table 7.3: Aperture photometry of five HII regions in HST original image and GAIA simulated flux map. HST electron counts, GAIA electron counts scaled to HST exposure time, error in magnitudes of GAIA aperture photometry with respect to HST aperture photometry and V magnitude of the HII regions in HST original image. A flux map obtained from 50 observations with 6×4 pixels/sample was used. The position of the HII regions on HST original image is given in the left image of Figure 7.1.

HII region	E_{HST}	E_{GAIA}	$\frac{E_{GAIA} - E_{HST}}{E_{HST}}$	V_{HST}
	e$^-$	e$^-$	mag	mag
1	192 769	159 549	-0.172	18.8492
2	147 170	115 019	-0.218	19.1423
3	178 634	137 214	-0.232	18.9319
4	222 181	198 978	-0.104	18.6950
5	361 727	304 130	-0.159	18.1659

The results are given in Table 7.3. The second column gives HST electron counts corrected for the background, the third one gives GAIA electron counts corrected for the background and scaled to HST exposure time, the fourth one gives the error in magnitudes of GAIA aperture photometry with respect to HST aperture photometry

and the fifth one gives the total V magnitude of the HII region according to HST data and to WFPC2 photometric calibration obtained by Holtzman et al. 1995b, adopting the color index of $V - I = 1.2$ from Prugniel and Héraudeau 1998.

A bias of about 0.2 mag towards faint magnitudes is clearly seen, together with a standard error of the result from 50 observations of about 0.05 mag, estimated from the agreement between the five values in the fourth column. A more careful inspection of the data shows that this bias is due to an underestimation of the signal counts of about 0.1 mag as well as to an overestimation of the background counts of about 0.3 mag. Both biases are easily understood as due to the relatively wide wings of GAIA PSF, which cause some energy to fall out of the 0.5 arcsec radius and thus in the outer annulus. A smaller contribution to the systematic error affecting the background determination seems to originate from the smearing of almost point-like features like faint stars and cosmic ray hits present in the HST image. Their smearing cause their electron counts, which as far as possible should not be considered in the background calculation, to spread over a fairly large area and thus to "escape" the median filtering used to reject them in the calculation of the background. These results could undoubtedly be improved, especially by application of PSF photometry instead of aperture photometry, as described e.g. by Høg, Fabricius, Knude and Makarov 1999, but this was beyond the scope of the present study.

Conclusions

The GAIA Galaxy Survey is a nearly all-sky, magnitude-limited, multi-color astrometric and photometric galaxy survey, to be carried out with the GAIA satellite, proposed to ESA for launch in 2009 as Cornerstone 5 of its Horizons 2000 scientific programme. In the framework of the present mission design, in this study the feasibility, scientific case and optimization of the GAIA Galaxy Survey were discussed.

From both statistical considerations and numerical simulations it appears that galaxies would best be detected in the ASM 1 within square areas of 2×2 arcsec^2 and observed in the BBPs with a sample size of 6×4 pixels. The first choice should yield the highest number of detected galaxies without too may false detections, whereas the second one yields the best trade-off between angular resolution and accuracy in surface photometry.

Galaxy observations could therefore be carried out in Astro 2, where a sample size of 6×4 pixels is not in conflict with the baseline sample size of 6×8 pixels adopted for the observation of stars, with only a small effort in terms of mission design and telemetry.

Under present assumptions about the instrumental performance of the satellite payload, the following measurement capabilities are expected from a 5-year mission:

- About 3 million galaxies brighter than $I \simeq 17$ will be detected.

- All detected galaxies will be observed with a 0.4 arcsec angular resolution and an all-mission accuracy in surface photometry of 0.15 mag/arcsec^2 at 19.5 mag/arcsec^2 in the V band.

- Multi-color (4–5 broad bands) and multi-epoch ($\simeq 50$ epochs) information will be available for all observed objects.

These outstanding measurement capabilities will result in unique datasets about galaxy spatial distribution and surface photometry over a nearly magnitude-limited sample extending down to low Galactic latitudes. In turn, these data are expected to yield significant scientific results concerning the large-scale structure of the Local Universe and the multi-color photometric structure of galaxy innermost regions.

The project being in its infancy, several developments are desirable in the near future in order to further demonstrate its feasibility, including:

- The design, implementation and testing of a dedicated galaxy detection algorithm is required in order to discuss the efficiency of galaxy detection and the issues related to star-galaxy discrimination, which could result in too many false detections.

- The refinement of the adopted stacking technique so as to fully recover GAIA optical resolution, e.g. through a drizzling-like technique.

- The discussion of galaxy observation in the PSM, where the much higher sensitivity with respect to the BBPs would result in a much higher accuracy in surface photometry.

- The statistical modeling of the properties of astrophysical objects whose existence could be induced on the basis of GAIA galaxy observations, such as massive black holes at the center of galaxies.

In its present form already, however, the GAIA Galaxy Survey promises to yield fundamental contributions to the study of external galaxies, thus complementing the core scientific case of the GAIA mission.

Appendix A

Units of Measure, Conversion Factors and Formulae

The units of measure used for angular and photometric quantities, the adopted conventions about their abbreviations, some useful conversion factors and formulae are here given.

A.1 Angular Quantities

In astronomy, angular quantities are generally expressed in sexagesimal units. The main units of measure of plane and solid angles are the following:

$$1 \text{ degree} = 1 \text{ deg}$$

$$1 \text{ second of arc} = 1 \text{ arcsec} = 1 \text{ as} = \frac{1}{3600} \text{ deg} = 10^3 \text{ mas} = 10^6 \ \mu\text{as}$$

$$1 \text{ radian} = 1 \text{ rad} = \frac{180}{\pi} \text{ deg} = \frac{648000}{\pi} \text{ arcsec}$$

$$1 \text{ square degree} = 1 \text{ deg}^2$$

$$1 \text{ steradian} = 1 \text{ sterad} = \frac{32400}{\pi^2} \text{ deg}^2$$

The whole sky spans a solid angle

$$\Omega_{sky} = 4\,\pi \text{ sterad} = \frac{129600}{\pi} \text{ deg}^2 \ ,$$

while the sky region where the absolute value of the Galactic latitude b is greater than a given value ϕ measures

$$\Omega\left(|b| > \phi\right) = 4\,\pi\,\sin\phi \quad [\text{sterad}] \ .$$

A.2   Photometric Quantities

The nomenclature of photometric quantitities in use in astronomical literature is far from standard and sometimes ambiguous. Here we therefore give a brief summary of the definitions and units of measure of these quantities as they are used in this study.

- The *Luminosity L* of a source is the energy radiated by the whole surface of the source per unit time, that is

$$L = \frac{\mathrm{d}E}{\mathrm{d}t} \ [\mathrm{J/s}] \ . \tag{A.1}$$

- The *Brightness F* of a source is the energy radiated by the whole surface of the source per unit time per unit area (of the receiver), that is

$$F = \frac{\mathrm{d}L}{\mathrm{d}A} = \frac{\mathrm{d}E}{\mathrm{d}A\,\mathrm{d}t} \ [\mathrm{J/m^2\,s}] \ . \tag{A.2}$$

- Most galaxies, unlike most stars, are resolved objects, so that in addition to measuring their total energy flux, we can in principle measure the energy flux per unit solid angle of the source coming from different regions. The *Surface Brightness* of a region of a diffuse source is the energy radiated by the region per unit time, per unit area (of the receiver) and per unit solid angle (of the source), that is

$$\Sigma = \frac{\mathrm{d}F}{\mathrm{d}\Omega} = \frac{\mathrm{d}L}{\mathrm{d}\Omega\,\mathrm{d}A} = \frac{\mathrm{d}E}{\mathrm{d}\Omega\,\mathrm{d}A\,\mathrm{d}t} \ [\mathrm{J/sterad\,m^2\,s}] \ . \tag{A.3}$$

Astronomers, however, generally express brightness and surface brightness in logarithmic units, i.e. in magnitudes (mag) and magnitudes per square second of arc (mag/arcsec^2), respectively. To define a magnitude scale, one has to arbitrarily choose a reference brightness F_{zp}, and the corresponding reference surface brightness Σ_{zp} of F_{zp} per square second of arc. The brightness of a source expressed in magnitudes is then

$$m = -2.5 \log \frac{F}{F_{zp}} \ [\mathrm{mag}] \ , \tag{A.4}$$

while the surface brightness of a region of a diffuse source in magnitudes per square second of arc is

$$\mu = -2.5 \log \frac{\Sigma}{\Sigma_{zp}} \ [\mathrm{mag/arcsec^2}] \ . \tag{A.5}$$

F_{zp} is called the zero-point of the adopted magnitude scale since $m = 0$ for $F = F_{zp}$ (and thus $\mu = 0$ for $\Sigma = \Sigma_{zp}$).

Note that these definitions equally apply to bolometric measurements and to measurements in a given photometric band.

Note also that the sky background is often expressed in different units, such as those described by Leinert et al. 1998.

Appendix B

The Historical Development of Astrometry

According to a strict definition, *astrometry* is the branch of astronomy devoted to the detemination of the positions of celestial bodies, and is therefore also known as *positional astronomy*. Position measurements, however, naturally lead to the direct determination of quantities such as the motions, distances and dimensions of the observed objects, which are needed for many astrophysical investigations. In particular, distance measurements are useful in calibrating the extragalactic distance scale and can be used in conjunction with photometric measurements to estimate luminosities. For this reason, astrometry has in time also come to indicate the measurement of these quantities. In very general terms, anything in the universe which is somehow distributed, moves or has a dimension or shape accessible to measurement is within the domain of astrometry. Thanks to its fundamental nature, throughout human history astrometry has repeatedly led to significant changes in our perception of the world (Hoskin 1999), and thanks to recent technological advances is likely to continue to do so is the future (Kovalevsky 1995). Without any claim to completeness, and considering that GAIA is chiefly an astrometric mission, it is therefore interesting and useful to briefly review the most significant phases of the development of this discipline up until the birth of contemporary astronomy.

In its original form astrometry certainly was the first science practised by man. Long before the invention of writing, archeological records show how the recognition of a pattern in the Sun's, the other stars' and the Moon's apparent motions deeply impressed our ancestors, who used to keep track of time by systematically observing the sky. Even greater must have been the sensation and the interest caused by the seemingly irregular apparent motions of the planets, to which some religious meaning was generally ascribed.

Although sophisticated astronomies also developed elsewhere, e.g. in China and in the Americas, historically astronomy as we know it today emerged in the Near East and in Europe, at the time of the Babylonians and the Greeks, respectively. The approach to astronomy by these two peoples was remarkably different, in that while the Babylonians

attached great importance to the accurate determination and prediction of the motions of the planets, the Greek tradition, a result of an intense mathematical and philosophical activity, was particularly committed to develop a geometrical model of the universe describing these motions. The achievements of Greek astronomy include e.g. the proof of Earth's sphericity by the Pythagorean philosophers and the accurate determination of Earth's radius by Eratosthenes.

Later, the conquests of Alexander the Great and the beginning of the Hellenistic era caused these two complementary approaches to merge, giving rise to an astronomy in which the models' predictions were routinely compared with observations, much like in the modern scientific method. Around the middle of the the second century BC Hipparchus, arguably the greatest of ancient astronomers, determined the Earth-Moon distance by measuring the Moon's parallax, discovered the precession of the equinoxes and compiled the first star catalogue of which we have an historical record, containing about 1 000 stars divided in six classes of brightness, or magnitudes. However, since the original written materials by these civilizations are very limited, most of what we know about Hellenistic astronomy, including Hipparchus' results, has come down to us thanks to Ptolemy's Almagest, a remarkable work of synthesis written in the second century AD and profoundly influenced by the Aristotelean view of the world.

Notwithstanding these accomplishments, the complicated models of Hellenistic astronomers could not predict the long-term motions of planets with an acceptable accuracy, and as a matter of fact the goal of a model capable to do so was not attained until the seventeenth century. Several factors led to this long standstill. From an observational vantage point, the poor accuracy of the available instruments did not allow observers to measure what was then considered, provided that the stars were at a finite distance, the only possible direct proof of the Earth's motion around the Sun, namely the stars' parallaxes. Crucial was then the abiding influence on western thought throughout the Middle Ages of the Aristotelian-Ptolemaic Weltanschauung, which was summarized in the Almagest and supported by the Catholic Church. According to this view, the Earth was a spherical body at rest at the center of the universe, the "fixed stars" described uniform circular motions around it, and the seven "wandering stars" (the Sun, the Moon and the five then-known planets) followed combinations of uniform circular motions. Since the true non-uniform elliptical motions taking place in the Solar System cannot be described in these terms, in order to improve the accuracy of their predictions, the geometric models started to get unbelievably complicated. Furthermore, these models also predicted some phenomena, such as a strong variation in the Moon's apparent size, which were not observed.

Despite these inconsistencies, the first heliocentric mathematical model of the Solar System was only developed in the first half of the sixteenth century by Nicolaus Copernicus. Although it did not significantly improve the accuracy of predictions, nor abandoned the assumption of uniform circular motions, his model was fundamental in casting doubt on the geocentric prejudice.

In the second half of the sixteenth century, in order to provide the first observational test between the two cosmologies, Tycho Brahe constructed a whole new range of instruments and carried out a long and intense programme of observations of stellar and

planetary positions, achieving an accuracy of about 1 arcmin, close to the resolution limit of the naked eye. Even with the aid of this superb instrumentation, however, he could not detect the stars' parallaxes, the apparent annual movements that were to be expected if they were being observed from a moving Earth, and thus concluded that the Earth was actually at rest.

On the contrary, through a careful analysis of Tycho's very data, Johannes Kepler was soon able to derive the three laws that now bear his name, which described the planetary orbits in terms of non-uniform elliptical motions in the framework of an heliocentric cosmology. Still, such sophisticated mathematical relationships were difficult to verify on the basis of the available observations, nor they were strictly valid owing to planetary perturbations, so that at first their strength was more in their formal elegance than in the accuracy of their predictions.

At the same time, the introduction of the spyglass for use in astronomical observations by Galileo Galilei greatly expanded the range of celestial phenomena that could be object of quantitative study. Thanks to a substantial increase in both resolution and sensitivity with respect to the naked eye, Galileo was able to observe for the first time the Moon's maria, Venus' phases, the sunspots, Jupiter's Medicean satellites and Saturn's rings and to resolve the Milky Way into a swarm of faint stars.

As further evidence of the universality of orbital motions throughout the Solar System and beyond was being gathered, a shift from a kynematical to a dynamical interpretation of the observations gradually took place. Towards the end on the seventeenth century, Isaac Newton finally managed to put observational evidence and Kepler's laws together in a coherent fully-general picture, in so doing laying the foundations of differential calculus as well as modern physics. The development of the mathematical techniques that were necessary to calculate in detail the predictions of his fundamental principles of dymanics and law of universal gravitation gave rise to celestial mechanics, which through the eighteenth and nineteenth century would have been the central problem in theoretical astronomy.

As for the observations, now that the Earth was firmly believed to orbit the Sun, the main problem was the determination of the stars' parallaxes, which was particularly difficult owing to the poorly understood atmospheric refraction as well as to other as yet unknown phenomena. In the course of this long-standing struggle, astronomers discovered most optical effects affecting the observations and inaugurated several research fields which now are the astrometrists' main objects of study. In the 1670s, by observing the eclipses of Jupiter's satellites, Ole Rømer showed that the speed of light was finite. In 1718, Edmond Halley measured for the first time the proper motions of three of the brightest stars in the sky, by comparing modern positions with those measured by Hipparchus. Around 1730, while he was trying to determine a star's parallax, James Bradley discovered the aberration of starlight and the nutation of Earth's rotation axis. The first effect, in particular, given the finite speed of light, provided an independent proof of the Earth's motion around the Sun. In 1783 William Herschel found indications that the Solar System as a whole is travelling in the direction of the Hercules constellation. In 1802 William Herschel discovered that several of the couples of stars that are observed to lie near to each other in the sky (double stars) are in fact orbiting a common center,

and thus are pairs of physically connected companions (binary stars), bound together by gravitational force[1]. Finally, in 1838 Friedrich Wilhelm Bessel, followed a few weeks later by Thomas Anderson, managed to measure the parallax of a star.

In summary, until the end of the nineteenth century, all astronomical observations were directed towards obtaining positions and brightnesses of as many celestial bodies as accurately as possible, and thus were astrometric in nature. In the last century, however, the development of *physical astronomy*, or *astrophysics*, which has its characteristic tool in spectroscopic measurements, attracted more interest and generated more excitement, so that sometimes one has the mistaken impression that astrometry is old-fashioned or even unimportant. Such an opinion is remarkably wrong not only because positions, parallaxes, proper motions, masses and radii of stars, which can only be obtained through astrometric techniques, are fundamental quantities in many domains of astrophysics, but also because the whole subject, thanks to the development of new techniques, has recently undergone a renaissance. In particular, the advent of astronomical satellites has significantly extended the observable wavelength region and increased the resolution of several orders of magnitude, bringing to the clarification of long-standing problems as well as to the discovery of numerous phenomena that now characterize contemporary astronomy. Even so, due to budgetary reasons most astrometric observations will still be carried out from the ground, and great care must therefore be given to the improvement of existing techniques for ground-based observations as well as to the development of new ones.

---

[1] Actually, the detailed evidence necessary to show that this force was of gravitational nature would not be available for another generation.

Appendix C

ESA and Space Science

The idea of an independent European space organization was born in the early 1960's, when the keen competition between the American and Soviet space agencies urged the western European countries to join their efforts in the scientific and technological space research. As a result of this process, in 1962 ELDO and ESRO were formed in order to develop fully European launchers and satellites, respectively. The European Space Agency (ESA) replaced ELDO and ESRO in 1973, and since then its mission has been to promote space science, research and technology for exclusively peaceful purposes. For over 30 years ESA space science projects have shown the scientific benefits of European as well as international cooperation. At the same time, ESA's industrial policy, with about 90% of the budget spent on contratcts with European industries, ensures a return on contributions for member states, both in financial and in technological terms.

Between 1968 and 1983 some 13 spacecraft were built and launched by ESA on scientific missions to study a vast array of disciplines. In 1984, in order to guarantee coherence, balance and continuity to its space science policy, and following the example of NASA, ESA established its first long-term scientific programme which was given the name Horizon 2000 and covered the 1995-2007 timeframe. In 1992, at the request of the ESA Council, a survey committee was established with the purpose of identifying the main scientific objectives and technological challenges of future space missions and to design a new long-term scientific programme for the 2007-2016 timeframe. In 1995 the programme elaborated following the committee's recommendations was approved and was given the name Horizon 2000+. It was also decided to refer to the Horizon 2000 and the Horizon 2000+ plans as to the Horizons 2000 plan. In its present implementation plan, which is shown in Figure C.1, the Horizons 2000 plan comprehends 8 so called cornerstone missions (approximately one every four years) and a larger number of smaller missions, covering most key space science fields.

In addition to its all-European projects, and following the evolution towards "Big Science" which has made worldwide cooperation a fundamental requirement to carry out state-of the-art scientific research, ESA is currently participating in most major international space science projects and is planning to do the same in the future.

In particular, since excellence in scientific research can only be achieved by devel-

oping and having easy access to state-of-the-art instruments, the success of a scientific community strongly depends on the effectiveness of the policy of the correspondent space agency.

Figure C.1: The current implementation plan of ESA Horizons 2000 scientific programme.

Appendix D

Galaxy Surface Brightness Radial Profiles

D.1 Sersic Law

The properties of galaxy surface brightness radial profiles can be derived in a general form using Sersic law, first introduced by Sersic 1968 and also known as $r^{1/n}$ law or generalized de Vaucouleurs law. This can be written as

$$\Sigma(r) = \Sigma_e \exp\left(-b_n \left[\left(\frac{r}{r_e}\right)^{1/n} - 1\right]\right) \ . \tag{D.1}$$

where r_e is the effective radius, or the radius within which the galaxy emits half its brightness, Σ_e is the surface brightness at r_e and b_n is a positive parameter that, for a given n, can be determined from the definition of r_e and Σ_e. The value of n determines the degree of concentration of the profile, quantified e.g. by the fraction of energy emitted within a given number of effective radii, the profile being steeper or less concentrated for higher n and conversely flatter or less concentrated for lower n. Particularly interesting special cases are the bulge-like $r^{1/4}$ profile for $n = 4$ and the disk-like exponential profile for $n = 1$, which will be discussed in greater detail in Sections D.2 and D.3.

According to Equation D.1, the brightness integrated within a given radius r is given

by

$$F(r) = \int_0^r 2\pi \, r' \, \Sigma(r') \, \mathrm{d}r' = 2\pi \, \Sigma_e \int_0^r r' \, \exp\left(-b_n \left[\left(\frac{r'}{r_e}\right)^{1/n} - 1\right]\right) \mathrm{d}r' =$$

$$= 2\pi \, \exp(b_n) \, \Sigma_e \int_0^r r' \, \exp\left[-b_n \left(\frac{r'}{r_e}\right)^{1/n}\right] \mathrm{d}r' = \left[r'' \equiv b_n \left(\frac{r'}{r_e}\right)^{1/n}\right] =$$

$$= 2\pi \, \exp(b_n) \, \Sigma_e \int_0^{b_n \left(\frac{r}{r_e}\right)^{1/n}} \frac{r_e}{b_n^n} \, r'' \, \exp(-r'') \, \frac{n \, r_e}{b_n^n} \, r''^{(n-1)} \, \mathrm{d}r'' = \tag{D.2}$$

$$= 2\pi \, \frac{n \exp(b_n)}{b_n^{2n}} \, \Sigma_e \, r_e^2 \int_0^{b_n \left(\frac{r}{r_e}\right)^{1/n}} r''^{(2n-1)} \, \exp(-r'') \, \mathrm{d}r'' =$$

$$= 2\pi \, \frac{n \exp(b_n)}{b_n^{2n}} \, \Sigma_e \, r_e^2 \, \gamma\left(2n \, , \, b_n \left(\frac{r}{r_e}\right)^{1/n}\right)$$

where γ is the incomplete gamma function. The total brightness predicted by the profile is

$$F_{tot} = \lim_{r \to \infty} F(r) = 2\pi \, \frac{n \exp(b_n)}{b_n^{2n}} \, \Sigma_e \, r_e^2 \, \lim_{x \to \infty} \gamma\left(2n \, , \, x\right) =$$
$$= 2\pi \, \frac{n \exp(b_n)}{b_n^{2n}} \, \Sigma_e \, r_e^2 \, \Gamma(2n) \equiv k_n \, \Sigma_e \, r_e^2 \tag{D.3}$$

where Γ is the gamma function. This relation, remembering that, by definition of effective radius, it is $F(r_e) = F_{tot}/2$, can be used to obtain an equation linking b_n and n. After cancellation of common terms, one obtains

$$\Gamma(2n) - 2\gamma(2n \, , \, b_n) = 0 \, , \tag{D.4}$$

a non-linear equation which can only be solved numerically, e.g. via the Newton Method (see Section 9.7 in Press et al. 1996). Values of b_n and k_n corresponding to integer values of n from 1 to 10 are given in Table D.1.

D.2   Bulge Profile

For $n = 4$, Equation D.1 becomes de Vaucouleurs, or $r^{1/4}$, law

$$\Sigma_b(r) = \Sigma_e \, \exp\left(-7.6692 \left[\left(\frac{r}{r_e}\right)^{1/4} - 1\right]\right) \, , \tag{D.5}$$

which characterizes the profiles of elliptical galaxies and bulge components of disk galaxies. According to this profile, the total brightness can be written as

$$F_{b,tot} = 22.665 \, \Sigma_e \, r_e^2 \, , \tag{D.6}$$

Table D.1: Values of b_n and k_n for different values of n.

n	b_n	k_n
1	1.6783470	11.948495
2	3.6720608	16.310881
3	5.6701554	19.743758
4	7.6692495	22.665234
5	9.6687149	25.251949
6	11.668363	27.597728
7	13.667757	29.759676
8	15.667704	31.774676
9	17.667636	33.669429
10	19.667567	35.463170

while the central surface brightness Σ_0 and the average surface brightness inside the effective radius $< \Sigma >_e$ are related to Σ_e by

$$\Sigma_0 = 2141.4\,\Sigma_e\ , \qquad < \Sigma >_e = \frac{F_{b,tot}/2}{\pi\,r_e^2} = 3.6072\,\Sigma_e\ . \tag{D.7}$$

Remembering Equation A.5, the bulge profile given by Equation D.5 can be put on a magnitude scale

$$\mu_b(r) = -2.5\,\log\left(\frac{\Sigma_b(r)}{\Sigma_{zp}}\right) = -2.5\,\log\left(\frac{\Sigma_e}{\Sigma_{zp}}\right) - \frac{2.5}{\ln 10}\left(-7.6692\left[\left(\frac{r}{r_e}\right)^{1/4} - 1\right]\right) =$$

$$= \mu_e + 8.3268\left[\left(\frac{r}{r_e}\right)^{1/4} - 1\right]\ [\mathrm{mag\ arcsec}^{-2}]\ , \tag{D.8}$$

while equalling Equations A.4 and D.6, one can express Σ_e as function of r_e and I, obtaining

$$\mu_e = -2.5\,\log\left(\frac{\Sigma_e}{\Sigma_{zp}}\right) = -2.5\,\log\left(\frac{F_{zp}\,\mathrm{dex}(0.4\,I)}{k_4\,\Sigma_{zp}\,r_e^2}\right) =$$

$$= 2.5\,\log(k_4) + 5\,\log\left(r_{e,[\mathrm{as}]}\right) + I_{[\mathrm{mag}]}\quad [\mathrm{mag\ arcsec}^{-2}]\ . \tag{D.9}$$

D.3 Disk Profile

For $n = 1$, Equation D.1 can be rewritten as the exponential law

$$\Sigma_d(r) = \Sigma_e\,\exp\left[-1.6783\left(\frac{r}{r_e} - 1\right)\right] = \exp(1.6783)\,\Sigma_e\,\exp\left(-\frac{1.6783}{r_e}\,r\right)$$

$$= 5.3567\,\Sigma_e\,\exp\left(-\frac{r}{r_e/1.6783}\right) = \Sigma_0\,\exp\left(-\frac{r}{r_s}\right)\ , \tag{D.10}$$

which characterizes the profile of disk components of disk galaxies, where Σ_0 is the central surface brightness and r_s is referred to as the disk scale length. The relations between these two quantities and Σ_e and r_e are respectively

$$\Sigma_0 = 5.3567\,\Sigma_e \,, \qquad r_s = \frac{r_e}{1.6783} \,. \tag{D.11}$$

According to this profile, the total brightness of the galaxy can be written as

$$F_{d,tot} = 11.948\,\Sigma_e\,r_e^2 \,. \tag{D.12}$$

while the average surface brightness inside the effective radius $<\Sigma>_e$ is related to Σ_e by

$$<\Sigma>_e = \frac{F_{d,tot}/2}{\pi\,r_e^2} = 1.9016\,\Sigma_e \,. \tag{D.13}$$

When put on a magnitude scale, the disk profile given by Equation D.10 becomes

$$
\begin{aligned}
\mu_d(r) &= -2.5\,\log\left(\frac{\Sigma_d(r)}{\Sigma_{zp}}\right) = -2.5\,\log\left(\frac{\Sigma_e}{\Sigma_{zp}}\right) - \frac{2.5}{\ln 10}\left[1.6783\left(\frac{r}{r_e}-1\right)\right] = \\
&= \mu_e + 1.8224\left(\frac{r}{r_e}-1\right)\ \text{[mag arcsec}^{-2}]\,,
\end{aligned}
\tag{D.14}
$$

while equalling Equations A.4 and D.12, one obtain for Σ_e the expression

$$
\begin{aligned}
\mu_e &= -2.5\,\log\left(\frac{\Sigma_e}{\Sigma_{zp}}\right) = -2.5\,\log\left(\frac{F_{zp}\,\mathrm{dex}(0.4\,I)}{k_1\,\Sigma_{zp}\,r_e^2}\right) = \\
&= 2.5\,\log\left(k_1\right) + 5\,\log\left(r_{e,[as]}\right) + I_{[\mathrm{mag}]}\quad\text{[mag arcsec}^{-2}]\,,
\end{aligned}
\tag{D.15}
$$

D.4   Bulge+Disk Profile

The surface brightness radial profiles of disk galaxies are usually modelled as the sum of a bulge and a disk component. The resulting bulge+disk profile can in general be written as

$$
\begin{aligned}
\Sigma_{b+d}(r) &= \Sigma_b(r) + \Sigma_d(r) = \\
&= \Sigma_{b,e}\,\exp\left(-7.6692\left[\left(\frac{r}{r_{b,e}}\right)^{1/4}-1\right]\right) + 5.3567\,\Sigma_{d,e}\,\exp\left(-1.6783\,\frac{r}{r_{d,e}}\right)\,,
\end{aligned}
\tag{D.16}
$$

where quantities subscripted with b and d refer to the bulge and disk component, respectively. The total brightness predicted by this profile is

$$F_{b+d,tot} = F_{b,tot} + F_{d,tot} = 22.665\,\Sigma_{b,e}\,r_{b,e}^2 + 11.948\,\Sigma_{d,e}\,r_{d,e}^2 \,. \tag{D.17}$$

The relative importance of the bulge and disk component in terms of the brightness they contribute to the overall profile can be quantified by the bulge/disk ratio B/D,

which, from Equations D.6 and D.12, can be expressed in terms of the bulge and disk parameters as

$$\frac{B}{D} = \frac{k_4 \, \Sigma_{b,e} \, r_{b,e}^2}{k_1 \, \Sigma_{d,e} \, r_{d,e}^2} = \frac{k_4}{k_1} \, \frac{\Sigma_{b,e}}{\Sigma_{d,e}} \, \frac{r_{b,e}^2}{r_{d,e}^2} = 1.8969 \, \rho_\Sigma \, \rho_r^2 \, , \tag{D.18}$$

where

$$\rho_\Sigma = \frac{\Sigma_{b,e}}{\Sigma_{d_e}} \, , \qquad \rho_r = \frac{r_{b,e}}{r_{d,e}} \, . \tag{D.19}$$

B/D is related to the more frequently used bulge/bulge+disk ratio B/T by the

$$\frac{B}{D} = \frac{B/T}{1 - B/T} \, . \tag{D.20}$$

The relation between the radii $r_{b,e}$ and $r_{d,e}$ and the effective radius of the bulge+disk profile $r_{b+d,e}$, can be determined using Equations D.2 and D.3, whose combination yields

$$\frac{k_4}{\Gamma(8)} \, \Sigma_{b,e} \, r_{b,e}^2 \, \gamma\left(8, b_4 \left(\frac{r_{b+d,e}}{r_{b,e}}\right)^{1/4}\right) + \frac{k_1}{\Gamma(2)} \, \Sigma_{d,e} \, r_{d,e}^2 \, \gamma\left(2, b_1 \frac{r_{b+d,e}}{r_{d,e}}\right) = \frac{k_4}{2} \, \Sigma_{b,e} \, r_{b,e}^2 + \frac{k_1}{2} \, \Sigma_{d,e} \, r_{d,e}^2 \, , \tag{D.21}$$

which, after trivial modifications, becomes

$$\frac{B}{D} \left[\frac{1}{\Gamma(8)} \, \gamma\left(8, b_4 \left(\frac{r_{b+d,e}}{r_{b,e}}\right)^{1/4}\right) - \frac{1}{2}\right] + \frac{k_1}{k_4} \left[\frac{1}{\Gamma(2)} \, \gamma\left(2, b_1 \, \rho_r \, \frac{r_{b+d,e}}{r_{b,e}}\right) - \frac{1}{2}\right] = 0 \, . \tag{D.22}$$

When values for the ratios B/D and ρ_r are assumed, Equation D.22 can be solved numerically to obtain the corresponding values of the ratios $r_{b,e}/r_{b+d,e}$ and $r_{d,e}/r_{b+d,e}$. Numerical values of the latter two ratios are given in Table D.2 for some values of the former two. Now, the general bulge+disk profile can be written as

$$\begin{aligned}\Sigma_{b+d}(r) = {} & \frac{\Sigma_{b,e}}{\Sigma_{b+d,e}} \, \Sigma_{b+d,e} \, \exp\left(-7.6692 \left[\left(\frac{r_{b+d,e}}{r_{b,e}} \, \frac{r}{r_{b+d,e}}\right)^{1/4} - 1\right]\right) + \\ & + 5.3567 \, \frac{\Sigma_{d,e}}{\Sigma_{b+d,e}} \, \Sigma_{b+d,e} \, \exp\left(-1.6783 \, \frac{r_{b+d,e}}{r_{d,e}} \, \frac{r}{r_{b+d,e}}\right) \, . \end{aligned} \tag{D.23}$$

In much the same way as Equation D.22, Equation D.23 can be numerically solved with respect to the ratios $\Sigma_{b,e}/\Sigma_{b+d,e}$ and $\Sigma_{d,e}/\Sigma_{b+d,e}$ if values of the ratios B/D and ρ_r are assumed. Numerical values of the two former ratios are given in Table D.3 for the same values of the latter two as in Table D.2. Tables D.2 and D.3, combined with Equation D.23, allows to write the appropriate bulge+disk profile for different values of B/D and ρ_r. The total brightness predicted by the law can then be written in terms of the bulge+disk quantities $r_{b+d,e}$ and $\Sigma_{b+d,e}$ as

$$F_{D,tot} = \left[k_4 \, \frac{\Sigma_{b,e}}{\Sigma_{b+d,e}} \left(\frac{r_{b,e}}{r_{b+d,e}}\right)^2 + k_1 \, \frac{\Sigma_{d,e}}{\Sigma_{b+d,e}} \left(\frac{r_{d,e}}{r_{b+d,e}}\right)^2\right] \Sigma_{b+d,e} \, r_{b+d,e}^2 \equiv k_{b+d} \, \Sigma_{b+d,e} \, r_{b+d,e}^2 \, , \tag{D.24}$$

Table D.2: Values of $r_{b,e}/r_{b+d,e}$ and $r_{d,e}/r_{b+d,e}$ for some values of B/D and ρ_r. Values calculated via Newton integration (see Section 9.7 in Press et al. 1996) of Equation D.22.

$\dfrac{r_{b,e}}{r_{b+d,e}}$		B/D				
		0.333	0.444	0.555	0.666	0.777
	0.3	0.37776903	0.39659331	0.41501285	0.43296121	0.45038387
	0.4	0.47738606	0.49489417	0.51165418	0.52767183	0.54296003
ρ_r	0.5	0.57169562	0.58717625	0.60178337	0.61556793	0.62857967
	0.6	0.66216968	0.67514232	0.68725805	0.69858888	0.70920016
	0.7	0.74977666	0.75987986	0.76924321	0.77794075	0.78603748
$\dfrac{r_{d,e}}{r_{b+d,e}}$		B/D				
		0.333	0.444	0.555	0.666	0.777
	0.3	1.2592301	1.3219777	1.3833761	1.4432040	1.5012795
	0.4	1.1934651	1.2372354	1.2791355	1.3191796	1.3574001
ρ_r	0.5	1.1433912	1.1743525	1.2035667	1.2311359	1.2571593
	0.6	1.1036161	1.1252372	1.1454301	1.1643148	1.1820002
	0.7	1.0711095	1.0855427	1.0989189	1.1113440	1.1229107

Table D.3: Values of $\Sigma_{b,e}/\Sigma_{b+d,e}$ and $\Sigma_{d,e}/\Sigma_{b+d,e}$ for the same values of B/D and ρ_r as in Table D.2. Values calculated from Equations D.16 and D.18, and from Table D.2.

$\dfrac{\Sigma_{b,e}}{\Sigma_{b+d,e}}$		B/D				
		0.333	0.444	0.555	0.666	0.777
	0.3	1.5059000	1.6695642	1.7862309	1.8669555	1.9202392
	0.4	0.90250402	1.0169289	1.1059437	1.1750876	1.2286100
ρ_r	0.5	0.61171687	0.69840479	0.76930751	0.82759966	0.87573973
	0.6	0.44733235	0.51643686	0.57490397	0.62470279	0.66737834
	0.7	0.34431760	0.40137789	0.45089086	0.49413744	0.53213802
$\dfrac{\Sigma_{d,e}}{\Sigma_{b+d,e}}$		B/D				
		0.333	0.444	0.555	0.666	0.777
	0.3	0.57903215	0.51357003	0.45788132	0.41020644	0.36917465
	0.4	0.61692617	0.55611501	0.50399454	0.45900376	0.41992150
ρ_r	0.5	0.65336297	0.59676211	0.54778829	0.50511037	0.46768035
	0.6	0.68801330	0.63543886	0.58948209	0.54903740	0.51322600
	0.7	0.72080756	0.67220776	0.62927470	0.59111205	0.55699899

and, proceeding like for the pure bulge and disk profiles, $\mu_{b+d,e}$ can be written as

$$\mu_{b+d,e} = 2.5 \log(k_{b+d}) + 5 \log(r_{e,[\mathrm{as}]}) + I_{[\mathrm{mag}]} \quad [\mathrm{mag\ arcsec}^{-2}] . \qquad (\mathrm{D.25})$$

Values of $k_{b,d}$ are given in Table D.4.

Table D.4: Values of k_{b+d} for the same values of B/D and ρ_r as in Tables D.2 and D.3. Values calculated from Equation D.24 and from Tables D.1, D.2 and D.3.

k_{b+d}		B/D				
		0.333	0.444	0.555	0.666	0.777
	0.3	15.841388	16.675985	17.443019	18.140889	18.770256
	0.4	15.161182	15.816591	16.415234	16.959955	17.454163
ρ_r	0.5	14.737528	15.291208	15.795789	16.255446	16.674198
	0.6	14.458169	14.948771	15.395577	15.803140	16.175547
	0.7	14.268144	14.717733	15.127242	15.501275	15.843825

Appendix E

HST Images and GAIA Simulated Flux Maps

Since only flux maps of a single galaxy were presented on a small scale in Chapter 7, here a small gallery of GAIA simulated flux maps is presented on a larger scale together with HST original images. The selection of the galaxies of this small sample was guided by the requirement that these must show conspicuous structure in order to illustrate the angular resolution achievabe in the flux maps. In so doing, PC images were always chosen because in WFPC2 images the galaxy cores are mostly imaged with this camera working at a smaller image scale on the focal plane with respect to the WFCs (see Section 6.1). All flux maps were obtained through stacking of 50 simulated observations obtained with 6×4 pixels/sample. Simulated observations were generated as described in Section 6.3, whereas stacking of observations was performed following the baseline stacking technique described in Section 6.4.

E.1   M100
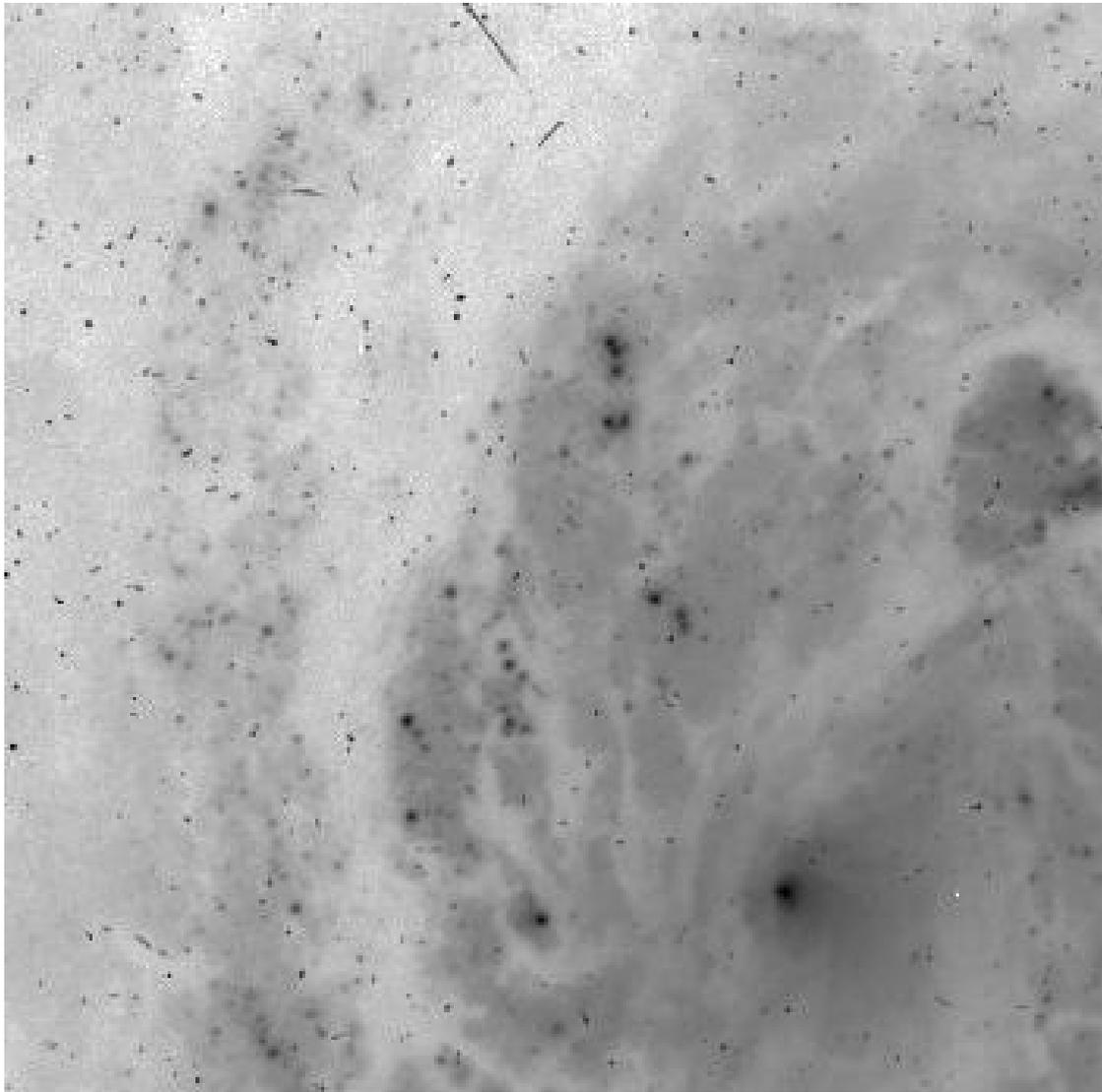
Figure E.1: HST WFPC2 PC image of M100. Central part of a WFPC2 PC image of M100, obtained with a 900 s exposure with the F555W filter, similar to V. The image side is about 16 arcsec.
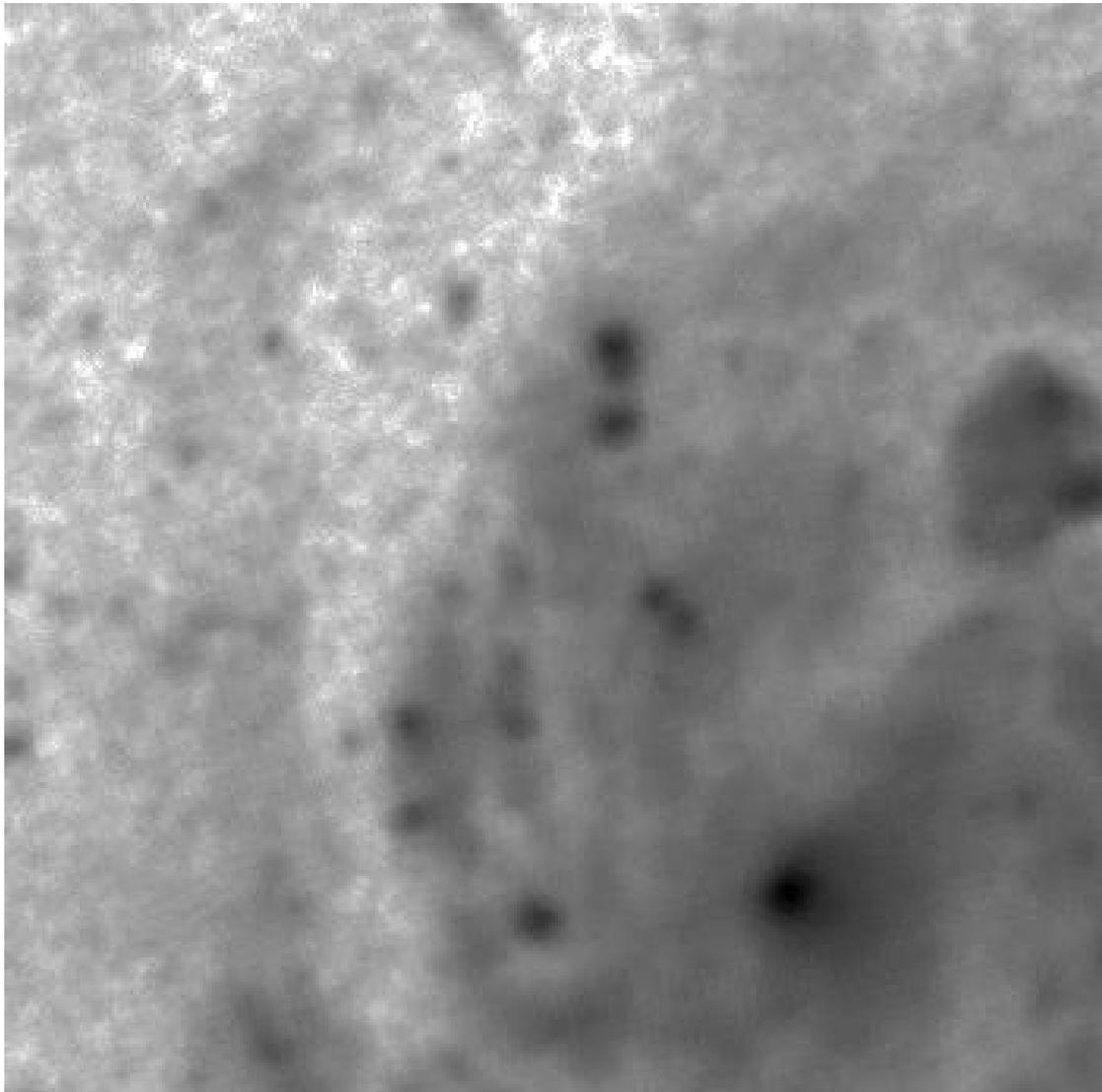
Figure E.2: GAIA simulated flux map of M100. BBP flux map reconstructed from 50 simulated observations, i.e. with an effective total exposure time of 43.09 s, obtained with 6×4 pixels/sample. The side of the flux map is about 16 arcsec.

E.2   NGC3177
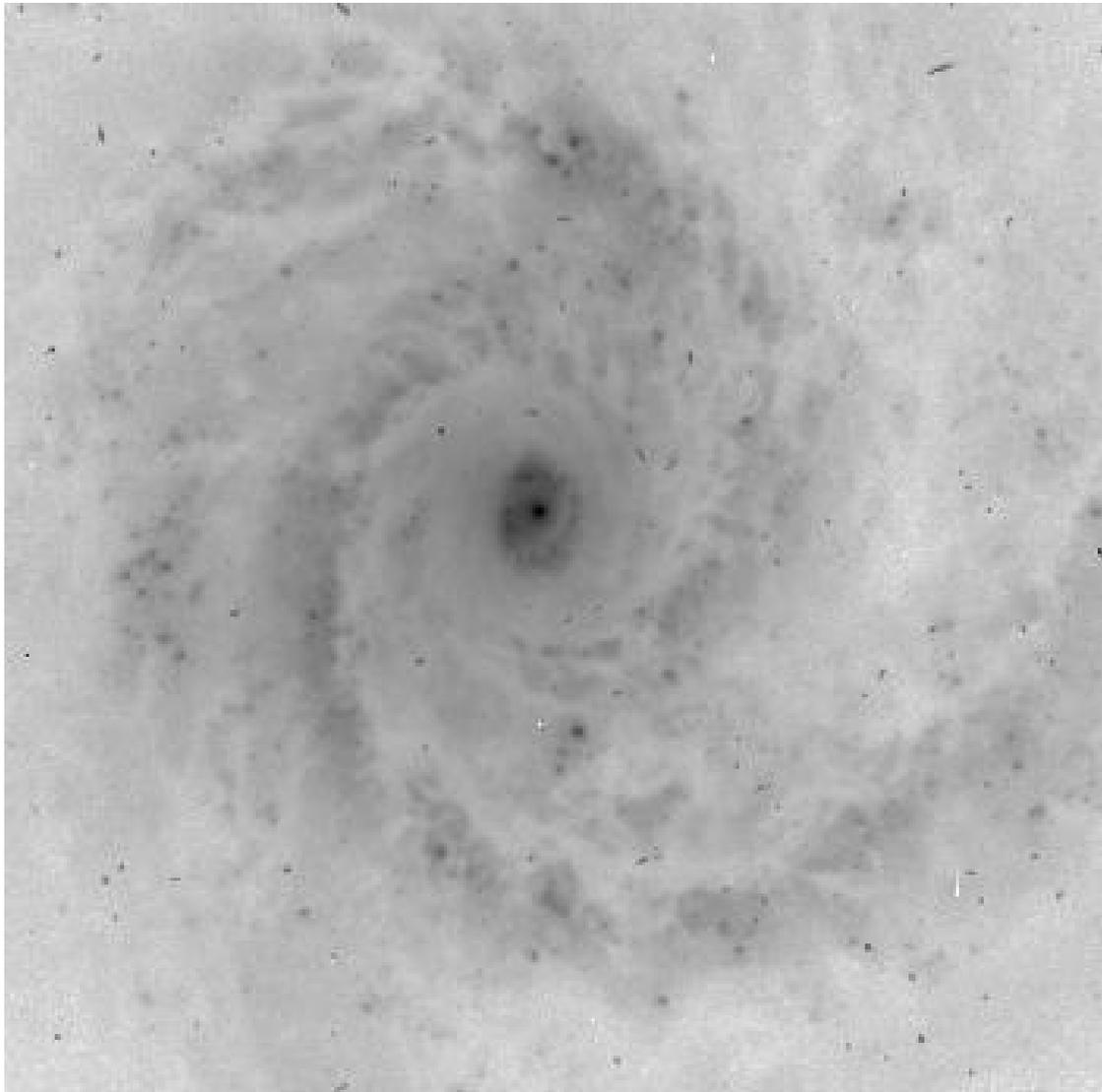
Figure E.3: HST WFPC2 PC image of NGC3177. Central part of a WFPC2 PC image of NGC3177, obtained with a 400 s exposure with the F606W filter, similar to V. The image side is about 16 arcsec.
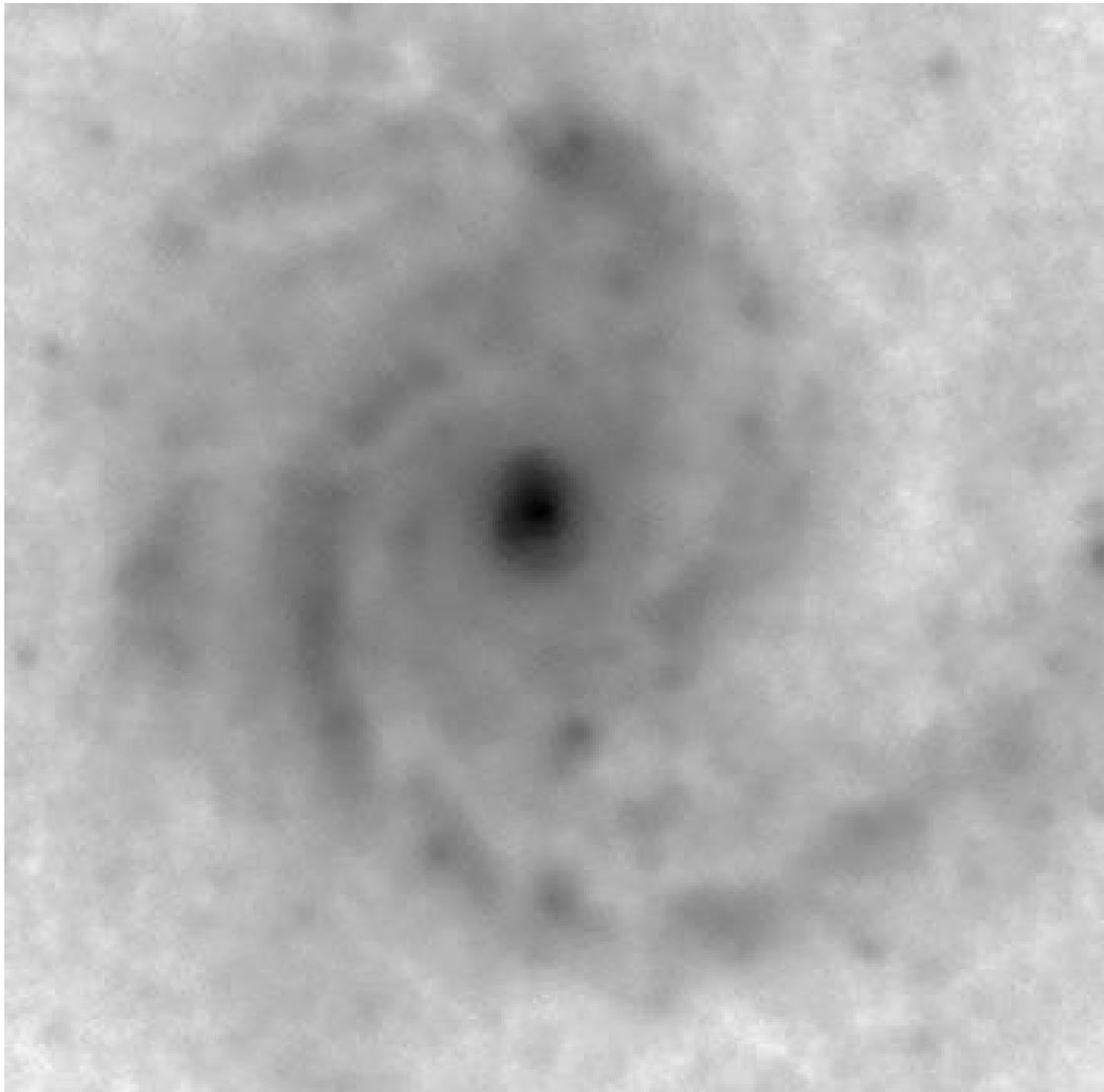
Figure E.4: GAIA simulated flux map of NGC3177. BBP flux map reconstructed from 50 simulated observations, i.e. with an effective total exposure time of 43.09 s, obtained with 6×4 pixels/sample. The side of the flux map is about 16 arcsec.

E.3   NGC3597
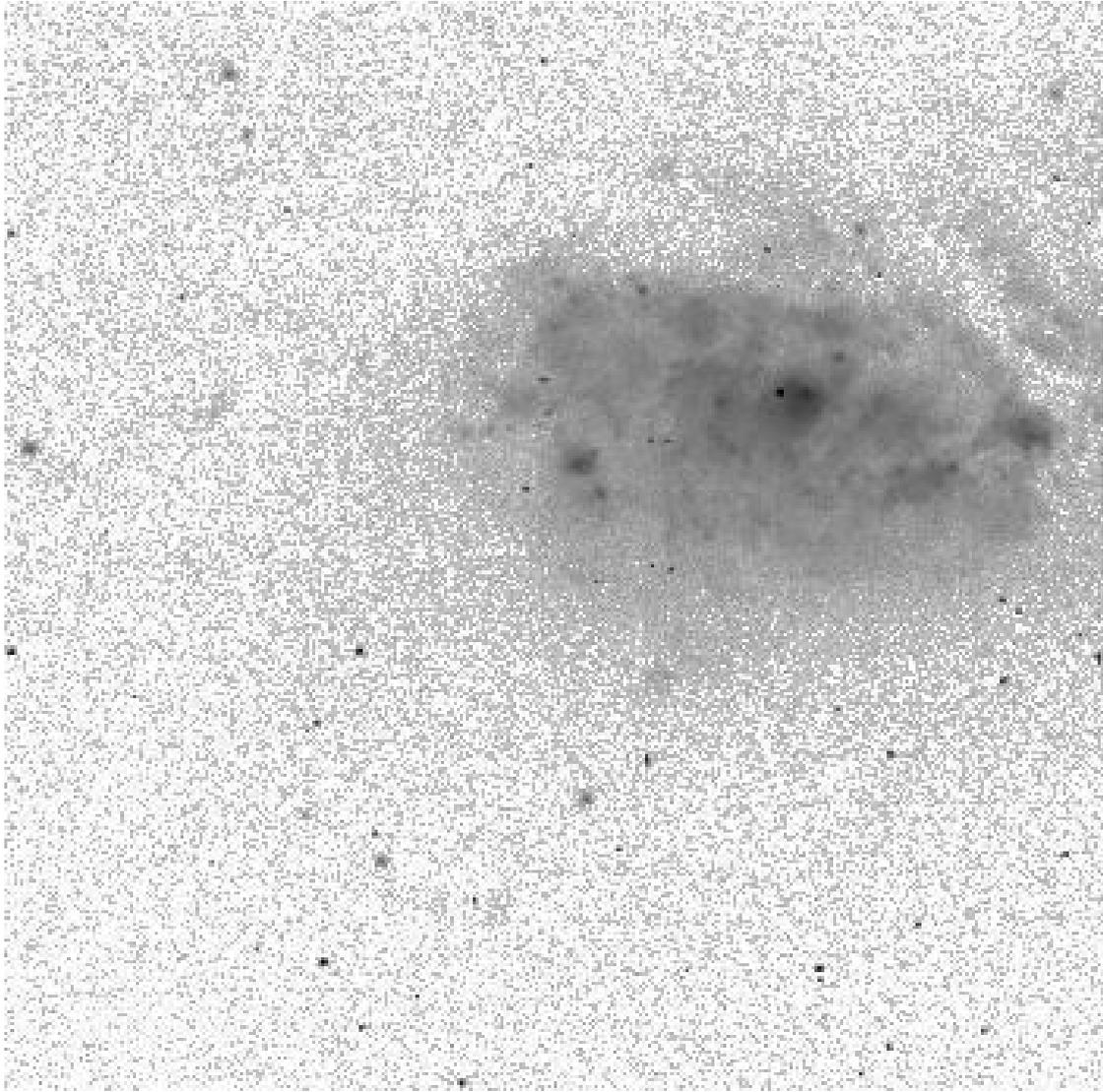
Figure E.5: HST WFPC2 PC image of NGC3597. Central part of a WFPC2 PC image of NGC3597, obtained with a 100 s exposure with the F555W filter, similar to V. The image side is about 16 arcsec.
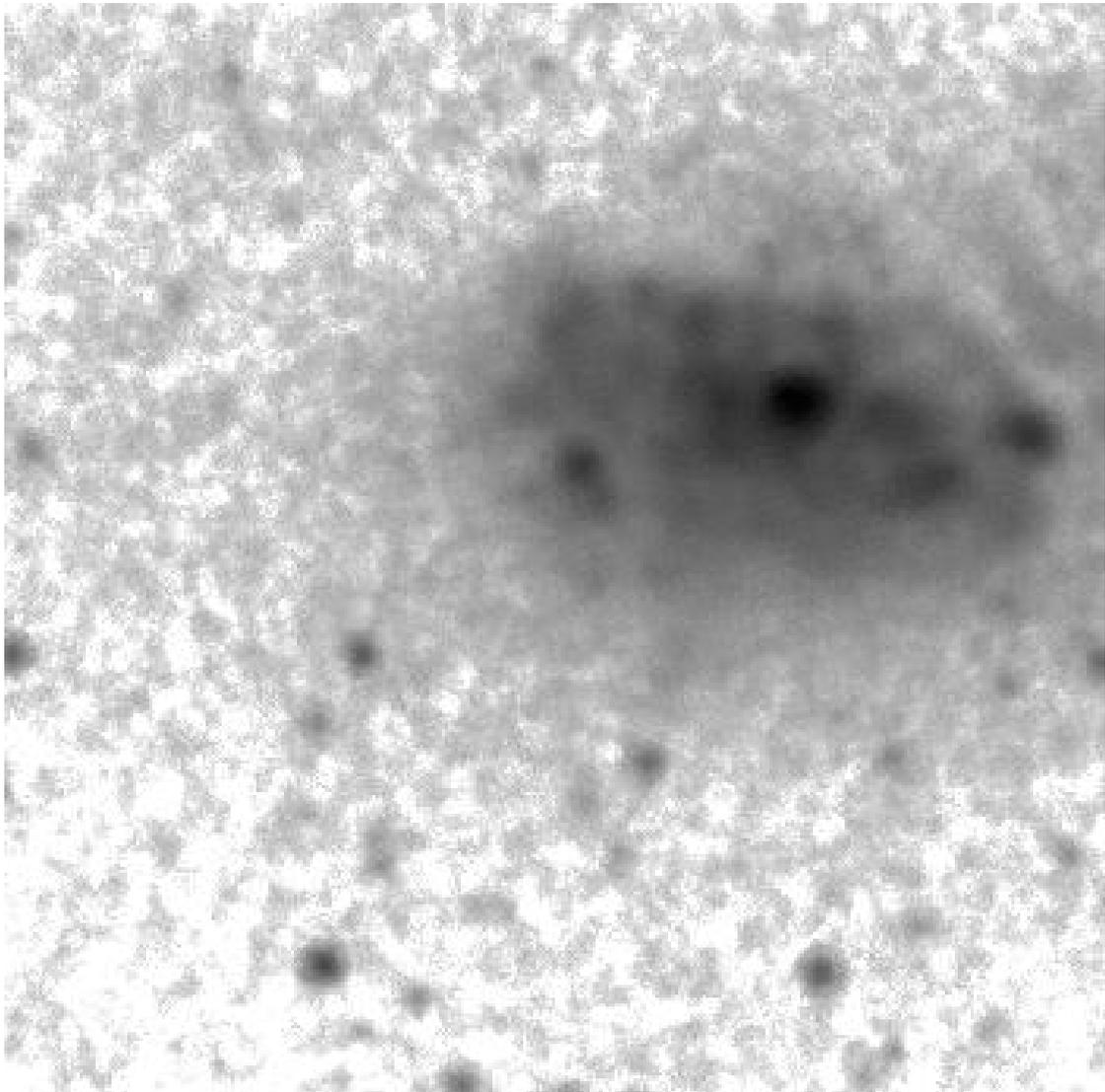
Figure E.6: GAIA simulated flux map of NGC3597. BBP flux map reconstructed from 50 simulated observations, i.e. with an effective total exposure time of 43.09 s, obtained with 6×4 pixels/sample. The side of the flux map is about 16 arcsec.

E.4   NGC6239
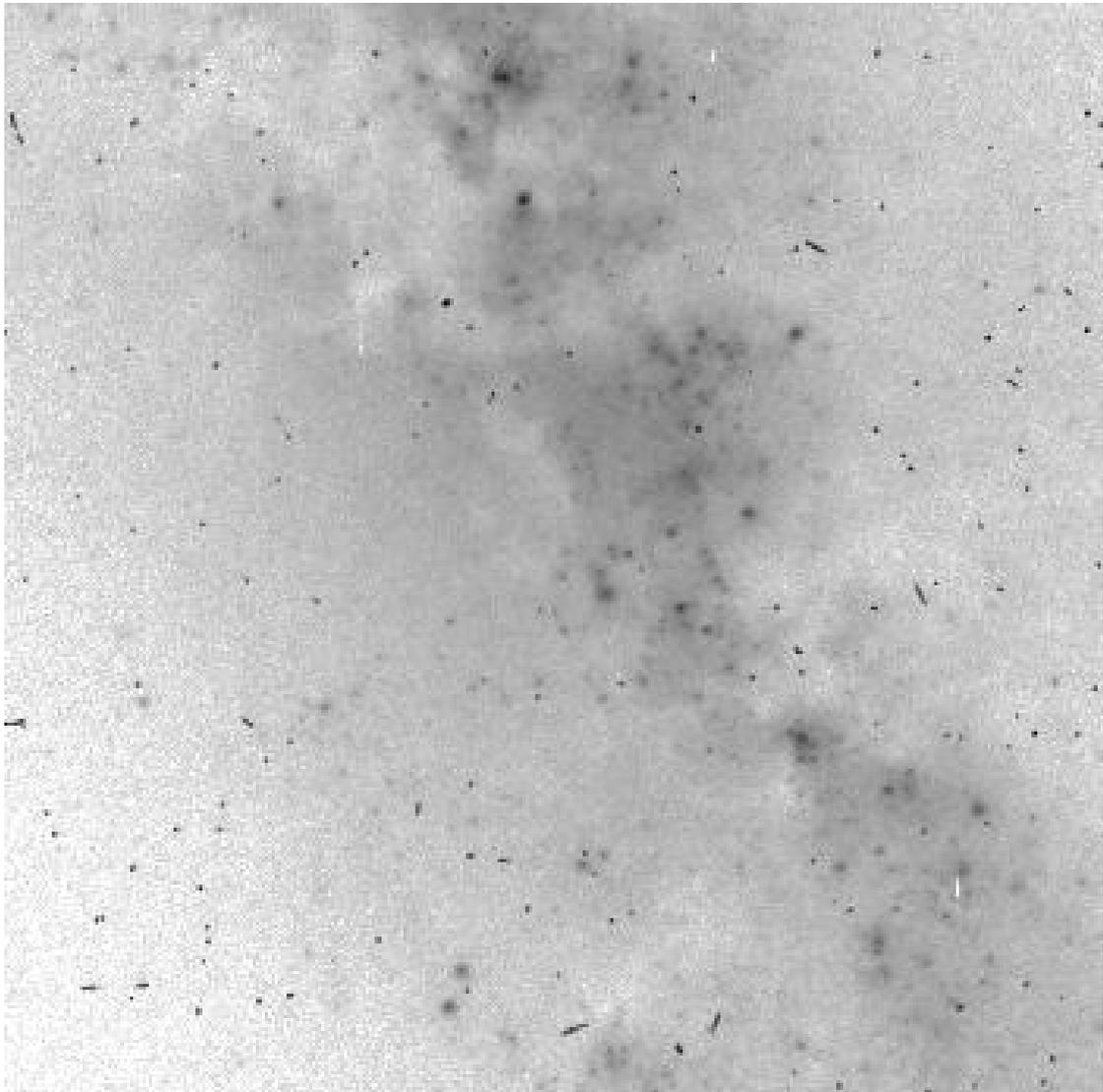
Figure E.7: HST WFPC2 PC image of NGC6239. Central part of a WFPC2 PC image of NGC6239, obtained with a 400 s exposure with the F606W filter, similar to V. The image side is about 16 arcsec.
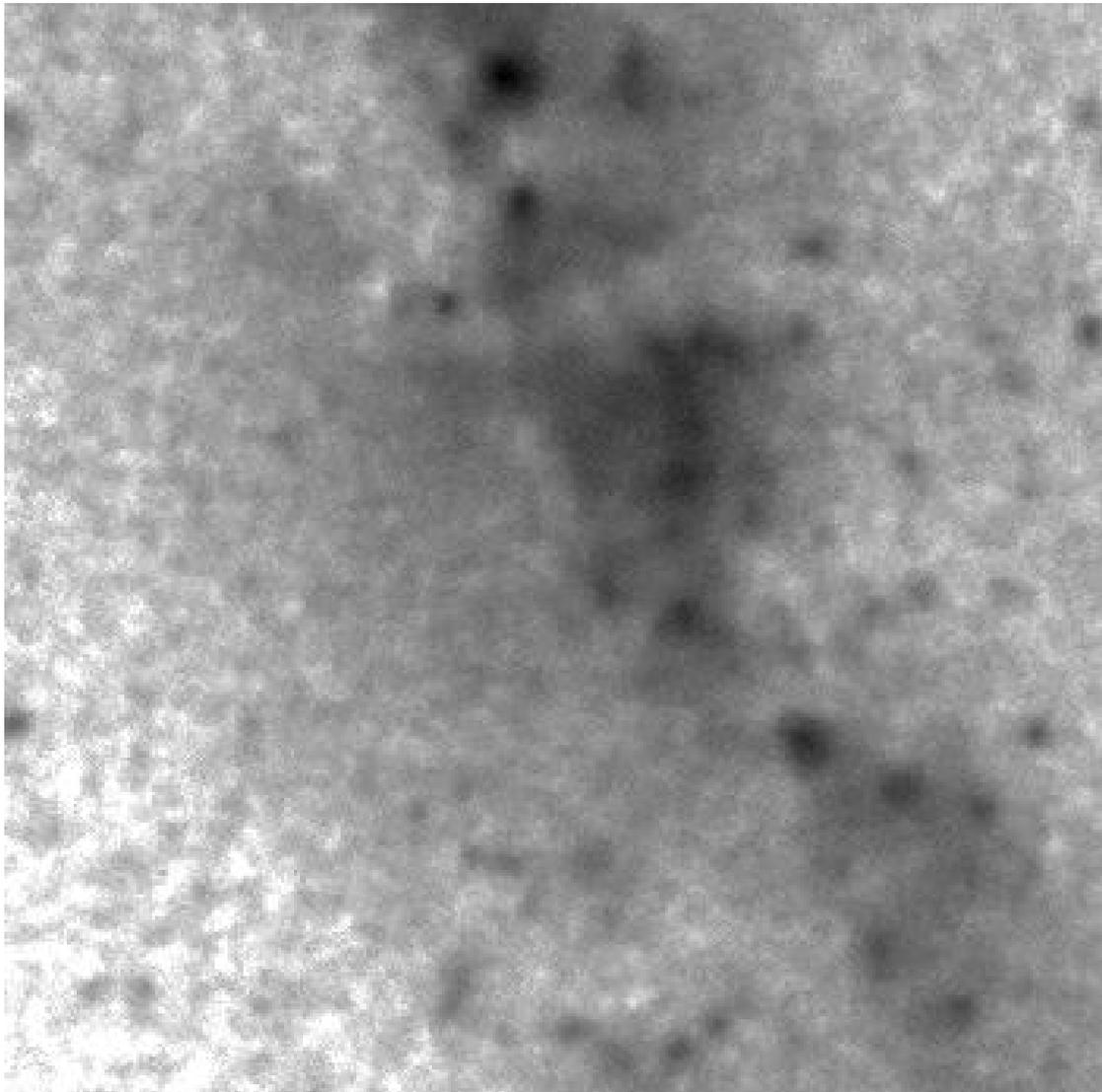
Figure E.8: GAIA simulated flux map of NGC6239. BBP flux map reconstructed from 50 simulated observations, i.e. with an effective total exposure time of 43.09 s, obtained with 6×4 pixels/sample. The side of the flux map is about 16 arcsec.

Appendix F

Drizzling

The problems related to mapping were recently studied in detail to fully exploit the possibilities offered by HST WFPC2 images. Due to the large size on the sky of the CCD pixels with respect to the width of the PSF delivered by the telescope optics, in these images the optical PSF is severely undersampled, leading to a decrease in the angular resolution achievable by the instrument. The techniques that have been developed in the HST community in order to recover the optical resolution are invariably based on *dithering*, i.e. on the superposition of several images of the same sky region displaced of a fraction of a pixel with respect to each other. In particular, a technique for the stacking of dithered images was developed for use in the Hubble Deep Field North (HDF-N) project (Williams et al. 1996, and called *drizzling*. Since all BBP sample sizes adopted in the simulation of GAIA galaxy observations severely undersample GAIA Astro optical PSF, and since the centers of different GAIA observations of the same sky region are displaced with respect to each other, it is interesting to try and apply this technique to our case.

The drizzling algorithm, which is also more formally known as variable-pixel linear reconstruction, is conceptually simple and similar to the stacking algorithm described in Section 6.4. In practice, the only difference is that each sample of each observation is shrinked of a factor of two along both directions before carrying out the subsampling[1]. Drizzling, however, is known to produce artifacts in the output image, and this effect, negligible in the HDF-N, increases in size with the ratio between the sample and flux map element sizes. Since in our case this ratio is particularly high, e.g. 24 for a sample size of 6×4 pixels against a ratio of about 4 used in the HDF-N, the artifacts may become unmanageably frequent and of large spatial extent. This is indeed the case, as illustrated by Figure F.1, where M100 flux maps obtained with the baseline stacking technique described in Section 6.4 and with the drizzling technique are compared. Throughout the drizzled flux map, conspicuous artifacts appear that could be easily confused with point-like features, should the overall signal-to-noise ratio be lower.

---

[1]Actually, the more refined version of the drizzling algorithm calculate the overlap between shrunken samples and flux map elements exactly rather than dividing each shrunken sample in a given number of square subsamples, but this does not significantly change the overall results.
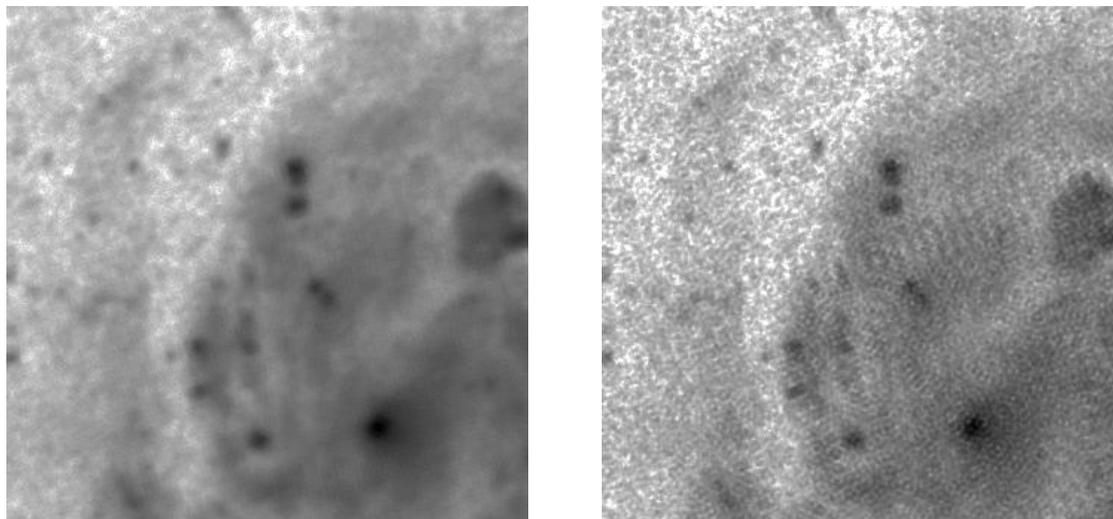
Figure F.1: Drizzling and artifacts. GAIA BBP flux maps of M100 reconstructed from 50 simulated observations, i.e. with an effective total exposure time of 43.09 s, obtained with 6×4 pixels/sample. Left: flux map obtained through the baseline stacking technique. Right: flux map obtained through the drizzling stacking technique. The side of each flux map is about 16 arcsec.

On the other hand, Figure F.2 illustrates how drizzling could increase the angular resolution of flux maps.
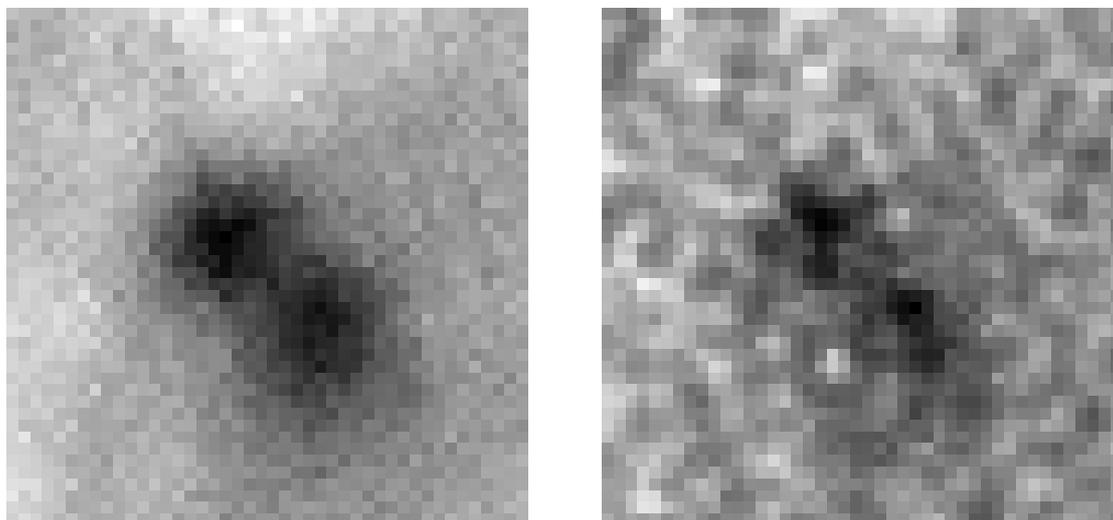
Figure F.2: Drizzling and angular resolution of flux maps. A detail of GAIA BBP flux maps of M100 reconstructed from 50 simulated observations, i.e. with an effective total exposure time of 43.09 s, obtained with 6×4 pixels/sample. Left: flux map obtained through the baseline stacking technique. Right: flux map obtained through the drizzling stacking technique. The side of each image is about 2 arcsec.

For these reasons, the drizzling algorithm, at least in its present form, is not to be considered for application in stacking of GAIA galaxy observations, but may be an interesting starting point for the development of dedicated stacking techniques aimed at fully recovering the optical resolution of GAIA observations.

Appendix G

Software

All the programs used in this study were written in Interactive Data Language (IDL), a complete computing environment integrating a powerful, array-oriented programming language with numerous data analysis and graphical display possibilities. IDL can be used both interactively and to create sophisticated functions, procedures or complex applications, and is becoming increasingly popular in the astronomical community. Since only the programs used for generation of simulated GAIA BBP observations on the basis of HST WFPC2 images and for their stacking into GAIA flux maps contain truly original contributions, only these are presented.

G.1 SIM_STACK.PRO

This program simulates a given number of GAIA BBP simulated observations of a given HST WFPC2 image and stacks them into a flux map following the procedures described in Sections 6.3 and 6.4, respectively.

```
 1 ;    PROGRAM              SIM_STACK.PRO
 2
 3 ; Last Updated           05 Jun 2000          Mattia Vaccari
 4
 5 ; This program generates a set of GAIA BBP simulated observations
 6 ;  of an HST WFPC2 field and stacks them into a GAIA flux map.
 7
 8 ; PARAMETERS
 9 hpix=[45.5,96.6]                   ; HST pixel in mas (PC and WFCs)
10 spfx=2l                            ; Subpixeling factors
11 spfy=2l
12 px=37.2                            ; GAIA pixel in mas
13 py=111.6
14 psx=[6,6,6,1,4,4]                  ; GAIA sample in pixels
15 psy=[8,4,2,8,8,4]
16 sx=psx*px                          ; GAIA sample in mas
17 sy=psy*py
18 obsside=[24998.4,55353.6]
19 ; Side of GAIA observation obtained from a WPPC2 field in mas
20 ;  (PC and WFCs respectively)
```

```
21 xi=round(obsside#(1./sx))
22 yi=round(obsside#(1./sy))
23 ; GAIA observation in samples for different combinations of
24 ;  WFPC2 cameras and BBP sample sizes
25 gaiaet=0.8618
26 ; GAIA observation exposure time in s
27 rn=[5.44289,6.74395,8.78593,10.4357,6.12805,7.83178]
28 ; GAIA BBP readnoise in e-/sample rms, calculated following SAG_MV_04
29 ;  assuming full CCD readout
30 ssfx=psx                                 ; Subsampling factors
31 ssfy=psy*3
32 ; The subsamples are squares of side 37.2 mas, which is also the sample size
33 ;  in the along scan direction
34 gstep=hpix/[1.,2.]                        ; GAIA flux map step in mas
35 ; gstep equals 45.5 and 48.3 mas for PC and WFCs respectively
36 gsize=[350l,320l]
37 ; Side of GAIA flux map in steps for PC and WFCs respectively
38 ; The side of GAIA flux map is thus 15925 and 15456 mas for PC and WFCs
39 ;  respectively
40
41 print,'The following .fits.gz files are available in the ./hstdata directory:'
42 spawn,'cd hstdata ; ls -C1 *.fits.gz | awk ''{print $1}''',fitsfiles,$
43 count=n_fits
44
45 for i=0,n_fits-1 do begin
46     print,i+1,strmid(fitsfiles(i),0,strlen(fitsfiles(i))-8),format='(i3,6x,a)'
47     endfor
48
49 print,'Enter the number of the file you want to open:'
50 fnu=0 & read,fnu
51 print,'Opening file number ',fnu
52 hstdnc=readfits('hstdata/'+fitsfiles(fnu-1),header,/silent)
53 himdim=size(hstdnc)
54
55 f=n_elements(header)
56
57 for j=0,f-2 do begin
58     r=header(j)
59     i=strpos(r,'DADSFILE=')
60     if i ne -1 then d=execute(strcompress(strmid(r,0,30),/remove_all)) else begin
61         i=strpos(r,'ROOTNAME=')
62         if i ne -1 then begin
63             d=execute(strcompress(strmid(r,0,30),/remove_all))
64             DADSFILE=ROOTNAME
65             endif
66         endelse
67     i=strpos(r,'INSTRUME=')& if i ne -1 then d=execute(strcompress(strmid(r,0,30),$
68     /remove_all))
69     i=strpos(r,'DATE    =')& if i ne -1 then d=execute(strcompress(strmid(r,0,30),$
70     /remove_all))
71     i=strpos(r,'TARGNAME=')& if i ne -1 then d=execute(strcompress(strmid(r,0,30),$
72     /remove_all))
73     i=strpos(r,'RA_TARG =')& if i ne -1 then d=execute(strcompress(strmid(r,0,30),$
74     /remove_all))
```

```
 75     i=strpos(r,'DEC_TARG=')& if i ne -1 then d=execute(strcompress(strmid(r,0,30),$
 76     /remove_all))
 77     i=strpos(r,'PA_V3   =')& if i ne -1 then d=execute(strcompress(strmid(r,0,30),$
 78     /remove_all))
 79     i=strpos(r,'FILTNAM1=')& if i ne -1 then d=execute(strcompress(strmid(r,0,30),$
 80     /remove_all))
 81     i=strpos(r,'FILTNAM2=')& if i ne -1 then d=execute(strcompress(strmid(r,0,30),$
 82     /remove_all))
 83     i=strpos(r,'EXPTIME =')& if i ne -1 then d=execute(strcompress(strmid(r,0,30),$
 84     /remove_all))
 85     i=strpos(r,'ATODGAIN=')& if i ne -1 then d=execute(strcompress(strmid(r,0,30),$
 86     /remove_all))
 87     i=strpos(r,'PHOTFLAM=')& if i ne -1 then d=execute(strcompress(strmid(r,0,30),$
 88     /remove_all))
 89     i=strpos(r,'PHOTZPT =')& if i ne -1 then d=execute(strcompress(strmid(r,0,30),$
 90     /remove_all))
 91     endfor
 92
 93 print,'DADSFILE',dadsfile,format='(a,15x,a)'
 94 print,'INSTRUMENT',instrume,format='(a,13x,a)'
 95 print,'OBSERVATION DATE',date,format='(a,7x,a)'
 96 print,'TARGET NAME',targname,format='(a,12x,a)'
 97 print,'RIGHT ASCENSCION',ra_targ,format='(a,1x,a)'
 98 print,'DECLINATION',dec_targ,format='(a,6x,a)'
 99 print,'V3 POSITION ANGLE',pa_v3
100 print,'FIRST FILTER NAME',filtnam1,format='(a,6x,a)'
101 print,'SECOND FILTER NAME',filtnam2,format='(a,5x,a)'
102 print,'EXPOSURE TIME',exptime,format='(a,4x,a)'
103 print,'ATODGAIN',atodgain,format='(a,9x,a)'
104
105 ; HST DATA NUMBER COUNTS
106 if himdim(0) eq 2 then begin
107     print,'This file contains one image.'
108     imagenu=1
109     endif
110
111 if himdim(0) eq 3 then begin
112     print,'This file contains ',himdim(3),' images. Which do you want to take?'$
113     ,format='(a,i1,a)'
114     imagenu=1 & read,imagenu
115     endif
116
117 imagenu=imagenu-1
118 hsti=imagenu<1
119 hpix=hpix(hsti)
120 camerastr=['PC','WFC2','WFC3','WFC4'] & camerastr=camerastr(imagenu)
121 print,'Creating HST WFPC2 '+camerastr+' image.'
122 hstdnc=hstdnc(*,*,imagenu)
123 ; Note that if the .fits.gz file containing the original data consists of one
124 ;  image only, the program assumes that this is a PC image. Otherwise, it
125 ;  assumes the file is in the format used by the HDA for the WFPC2 data files,
126 ;  i.e. that it contains, in this order the four images obtained with the
127 ;  PC, WFC2, WFC3 and WFC4.
128
```

```
129 ; A/D GAIN
130 gain=[[7.12,7.12,6.90,7.10],[13.99,14.50,13.95,13.95]]
131 gain=gain(imagenu,round(atodgain/7.)-1)
132 ; HST WFPC2 A/D conversion gain, from "WFPC2 Instrument Handbook",
133 ;   Version 4.0, page 82
134
135 lss:
136 print,'What BBP sample size do you want to use?'
137 print,'1=6x8  2=6x4  3=6x2  4=1x8  5=4x8  6=4x4'
138 ss=1 & read,ss
139 if total([1.,2.,3.,4.,5.,6.] eq ss) eq 0 then begin
140     print,'Invalid choice!'
141     goto,lss
142     endif
143 ss=ss-1
144
145 ; PARAMETERS' CHOICE
146 psx=psx(ss)
147 psy=psy(ss)
148 sx=sx(ss)
149 sy=sy(ss)
150 xi=xi(hsti,ss)
151 yi=yi(hsti,ss)
152 rn=rn(ss)
153 ssfx=ssfx(ss)
154 ssfy=ssfy(ss)
155 gstep=gstep(hsti)
156 gsize=gsize(hsti)
157
158 ; HST IMAGE PHOTOMETRIC CALIBRATION
159 vi=1.2
160 ; Average V-I Galaxy Color Index from Prugniel and H\'eraudeau 1998
161
162 calpar=[[21.729,-0.051,+0.009],$ ; F555W
163 [22.093,+0.254,+0.012],$ ; F606W
164 [20.920,-0.124,+0.028]]  ; F814W
165
166 case filtnam1 of
167     'F555W' : begin
168         filtnu=0
169         stamag='V'
170         end
171     'F606W' : begin
172         filtnu=1
173         stamag='V'
174         end
175     'F814W' : begin
176         filtnu=2
177         stamag='I'
178         end
179     else : begin
180         print,'The ',filtnam1,' filter is not supported! ',$
181         'Using F555W-V transformations!'
182         filtnu=0
```

```
183         stamag='V'
184           end
185       endcase
186
187 case stamag of
188     'V' : muback=22.06
189     'I' : muback=21.46
190     endcase
191 ; Sky background in mag/arcsec^2. From SAG_GG_05.
192 ; Note that the choice of this parameter does not affect in any way
193 ;  the processing of the data, but their representation only
194
195 gr=[1.987,2.003,2.006,1.955]
196 ; Gain ratio from Holtzman et al. 1995b
197 dm=2.5*alog10(gr)
198 if atodgain eq 7. then dm=dm(imagenu) else dm=0.
199 ; Since most photometric calibration observations were done with atodgain=15,
200 ;  there is a correction dm to be applied for exposures carried out with
201 ;  atodgain=7
202
203 ; HST IMAGE IN UNCALIBRATED MAGNITUDES
204 parhstdn=(exptime*(hpix/1000.)^2)*10^(0.4*(calpar(0,filtnu)+$
205 calpar(1,filtnu)*vi+calpar(2,filtnu)*vi^2+dm+0.1-muback))
206 ; Sky background parameter in data numbers
207 ;parhstdn=4.0
208 ; An alternative sky background parameter can be used to obtain a better
209 ;  image visibility (i.e. an higher contrast). In the case of m100_900,
210 ;  for instance, only 132 out of 122500 pixels (0.1%) in the [350,350] central
211 ;  region of the PC image "contained" less than 4 data numbers.
212 hstmag=-2.5*alog10(hstdnc>parhstdn)
213 rdim=[350l,160l] & rdim=rdim(hsti)
214 hstmagcen=hstmag((himdim(1)-rdim)/2:(himdim(1)+rdim)/2-1,$
215 (himdim(2)-rdim)/2:(himdim(2)+rdim)/2-1)
216 ; hstmagcen covers the central part of hstmag corresponding to a square area
217 ;  of side 15925 and 15456 mas, for PC and WFC respectively, i.e. exactly the
218 ;  portion of the HST image that is covered by GAIA flux map.
219
220 ; HST IMAGE IN WFPC2 INSTRUMENTAL MAGNITUDES
221 ; See "WFPC2 Instrument Handbook", Version 4.0, Section 8.7
222 ;zp=-2.5*alog10(photflam)+photzpt
223 ; Zero-point of the "FILTNAM1" magnitude scale
224 ;hstmagins=-2.5*alog10((hstdnc>parhstdn)/(exptime*(hpix/1000.)^2))+zp
225 ; HST image in "FILTNAM1" magnitudes
226
227 ; HST IMAGE IN STANDARD MAGNITUDES
228 hstmagsta=-2.5*alog10((hstdnc>parhstdn)/(exptime*(hpix/1000.)^2))+$
229 calpar(0,filtnu)+calpar(1,filtnu)*vi+calpar(2,filtnu)*vi^2+dm+0.1
230 ; HST image in stamag standard magnitudes
231 ; The transformations between WFPC2 Data Number counts to standard magnitudes
232 ;  are carried out using Equation 9 and Table 10 from Holtzman et al. 1995b,
233 ;  with a constant correction of 0.1 mag/arcsec^2 for infinite aperture
234
235 ; HST ELECTRON COUNTS
236 ;hstelc=gain*hstdnc
```

```
237 ; The atodgain keyword can be equal to 7 or 15, but the true value of the
238 ;  A/D conversion gain (given by the variable gain) is actually very
239 ;  near to 7 and 14, respectively, and is different in WFPC2's different
240 ;  detectors. Please note that we do not use the gain value in the
241 ;  conversion to a magnitude scale. Actually, we only use it to give an
242 ;  estimate of GAIA's electron counts, which we have to combine with
243 ;  readnoise estimates (given in electrons) to properly take into
244 ;  account the noise.
245 ;parhstel=gain*parhstdn    ; sky background parameter in electrons
246 ; parhstel=30.
247 ; An alternative sky background parameter can be used to obtain a better
248 ;  image visibility (i.e. an higher contrast). In the case of m100_900,
249 ;  for instance, only 171 out of 122500 pixels (0.14%) in the central region
250 ;  of the PC image "contained" less than 30 electrons.
251
252 ; GENERATION OF CENTERS AND POSITION ANGLES OF OBSERVATIONS
253 print,'How many simulated observations do you want to generate?'
254 nobs=1 & read,nobs
255 ; if nobs eq 1 then posa=0. & cx=0. & cy=0. else begin ..... endif
256 lsd:
257 print,'How do you want the position angles of the scan directions '+$
258 'to be distributed?'
259 print,'        1=0-360    2=0-45 or 90-135    3=0-90    4=0-45'
260 sd=1 & read,sd
261 if total([1.,2.,3.,4.] eq sd) eq 0 then begin
262     print,'Invalid choice!'
263     goto,lsd
264     endif
265 ; The value of sd goes in increasing order of non-randomness
266 ;  of the scan directions
267 case sd of
268     1 : posa=randomu(seed,nobs)*(2*!pi)
269     2 : begin
270         posa=randomu(seed,nobs)*(!pi/4)
271         posa=posa+((-1)^round(randomu(seed,nobs)*1000000.)*(!pi/4)+(!pi/4))
272         end
273     3 : posa=randomu(seed,nobs)*(!pi/2)
274     4 : posa=randomu(seed,nobs)*(!pi/4)
275     endcase
276 ; posa contains the position angles (measured counterclockwise)
277 ;  of GAIA FORs with respect to the HST FOR
278 cx=(randomu(seed,nobs)-0.5)*sx
279 cy=(randomu(seed,nobs)-0.5)*sy
280 ; cx and cy contain the coordinates of the centers of GAIA FORs
281 ;  (i.e. of GAIA observations) in the HST FOR
282
283 ; In other words, the GAIA FOR for the nth observation is obtained
284 ;  starting from the HST FOR by a translation of a vector [cx(n),cy(n)]
285 ;  followed by a rotation around the center of the FOR thus obtained
286 ;  of an angle posa(n) measured counterclockwise
287
288 lsc:
289 print,'Do you want to display GAIA flux map on screen (y/n)?'
290 sc='...' & read,sc
```

```
291 if sc ne 'y' and sc ne 'n' then begin
292     print,'Invalid choice!'
293     goto,lsc
294     endif
295
296 lps:
297 print,'Do you want to save the flux map in magnitudes to an eps file (y/n)?'
298 ps='...' & read,ps
299 if ps ne 'y' and ps ne 'n' then begin
300     print,'Invalid choice!'
301     goto,lps
302     endif
303 if ps eq 'y' then begin
304     print,'Enter filename without the .eps extension:'
305     fn='fluxmap.eps' & read,fn
306     print,'Enter the side of the image in centimetres:'
307     fms=16. & read,fms
308     endif
309
310 lst:
311 print,'Do you want to save the important data into an IDL structure (y/n)?'
312 st='...' & read,st
313 if st ne 'y' and st ne 'n' then begin
314     print,'Invalid choice!'
315     goto,lst
316     endif
317 if st eq 'y' then begin
318     lstfile:
319     print,'Do you want to save this structure into a dat file (y/n)?'
320     stfile='...' & read,stfile
321     if stfile ne 'y' and stfile ne 'n' then begin
322         print,'Invalid choice!'
323         goto,lstfile
324         endif
325     if stfile eq 'y' then begin
326         print,'Enter filename without the .dat extension:'
327         simfn='sim_data.dat' & read,simfn
328         endif
329     endif
330
331 ssstr=['6x8','6x4','6x2','1x8','4x8','4x4'] & ssstr=ssstr(ss)
332 print,'Generating and stacking GAIA ',ssstr,' pixels/sample BBP '+$
333 'simulated observations.'
334 print,'Please wait...'
335
336 ; EXPOSURE TIME SCALING OF HST ELECTRON COUNTS
337 ;hgelc=(gain*gaiaet/exptime)*hstdnc
338 ; HST electron counts scaled to GAIA exposure time
339 ; We assume that the electron counts per unit time per unit area of the two
340 ;  instruments are equal, which is conservative for most combinations of
341 ;  HST-GAIA filters.
342
343 ; SUBPIXELING OF HST IMAGE
344 sphim=rebin(hstdnc,himdim(1)*spfx,himdim(2)*spfy,/sample)*$
```

```
345 ((gain*gaiaet)/(exptime*spfx*spfy))
346 ; Subpixeling of each HST pixel into 4 subpixels
347 ; The rebin function with the sample keyword performs a nearest neighbour
348 ;  sampling, thus preserving the total number of electrons with great accuracy
349
350 ; PSF
351 psfname=['68','64','62','18','48','44']
352 psf=readfits('psf/'+'glo_10_'+psfname(ss)+'.fits.gz',/silent)
353 ;psf=readfits('psf/'+psfname+'.fits.gz',/silent)
354 ; (517,517) PSF obtained following SAG_LL_025, using syntfits.f and
355 ; assuming V-I=1.2 and Field Point 10
356 ; The PSF is sampled with a step of 1/4 pixel along both directions
357 ; The total area mapped by the PSF is thus of
358 ;  (517,517)*(1/4)*(px,py)=(4.8081,14.4243) arcsec^2
359 xtot=[21,21,129,33,33,21] & xtot=xtot(ss)
360 xmed=[10,10,64,16,16,10]  & xmed=xmed(ss)
361 dx=[24,24,4,16,16,24]     & dx=dx(ss)
362 xin=(findgen(xtot)-xmed)*dx+258
363 ytot=[33,17,17,33,17,65] & ytot=ytot(ss)
364 ymed=[16,8,8,16,8,32]    & ymed=ymed(ss)
365 dy=[16,32,32,16,32,8]    & dy=dy(ss)
366 yin=(findgen(ytot)-ymed)*dy+258
367 psf=psf(xin,*)
368 psf=psf(*,yin)
369 ; PSF resampling with a step equal to sample size
370 case ss of
371     0 : psf=psf(6:14,10:22)
372     1 : psf=psf(6:14,5:11)
373     2 : psf=psf(40:88,5:11)
374     3 : psf=psf(10:22,10:22)
375     4 : psf=psf(10:22,5:11)
376     5 : psf=psf(6:14,20:44)
377     endcase
378 ; Reduced PSF with a step equal to sample size
379 ; In other words, we truncate the PSF to a central region of about
380 ; (50,50) pixel = (1860,5580) arcsec containing about 99% of the
381 ;  complete PSF (i.e. of the energy)
382 psf=psf/total(psf)
383 ; Normalization
384
385 ; ARRAYS' CREATION
386 scx=(findgen(xi)-0.5*(xi-1))*sx
387 scy=(findgen(yi)-0.5*(yi-1))*sy
388 ; scx and scy contain the coordinates of samples' centers
389 ;  in the observation FOR
390 spcx=( findgen(himdim(1)*spfx)-0.5*(himdim(1)*spfx-1) )*(hpix/spfx)
391 spcy=( findgen(himdim(2)*spfy)-0.5*(himdim(2)*spfy-1) )*(hpix/spfy)
392 ; spcx and spcy contain the coordinates of subpixels' centers
393 ;  in the HST FOR
394 ob=fltarr(xi,yi)
395 ; ob will contain the nth observation during processing
396 obs=fltarr(nobs,xi,yi)
397 ; obs will contain the nobs observations
398 sscx=(findgen(xi*ssfx)-0.5*(xi*ssfx-1))*(sx/ssfx)
```

```
399 sscy=(findgen(yi*ssfy)-0.5*(yi*ssfy-1))*(sy/ssfy)
400 ; sscx and sscy contain the coordinates of subsamples' centers
401 ;  in the observation FOR
402 fmgrid=(findgen(gsize)-0.5*(gsize-1))*gstep
403 ; Coordinates of the centers of the flux map elements in the HST FOR
404 pfm=fltarr(gsize,gsize)
405 ; pfm will contain the partial flux map
406 nfm=fltarr(nobs,gsize,gsize)
407 ; nfm will contain the nobs partial flux maps
408 gfm=fltarr(gsize,gsize)
409 ; gfm will contain the global flux map
410
411 for n=0,nobs-1 do begin
412
413     ; COORDINATES OF SUBPIXELS' CENTERS IN THE OBSERVATION FOR
414     auxx   =+((spcx-cx(n))#(fltarr(himdim(2)*spfy)+1.))*cos(posa(n))$
415     +((fltarr(himdim(1)*spfx)+1.)#(spcy-cy(n)))*sin(posa(n))
416     auxy   =-((spcx-cx(n))#(fltarr(himdim(2)*spfy)+1.))*sin(posa(n))$
417     +((fltarr(himdim(1)*spfx)+1.)#(spcy-cy(n)))*cos(posa(n))
418
419     ; REBINNING OF GAIA OBSERVATION
420     for i=0,xi-1 do begin
421         xin=where(abs(auxx-scx(i)) lt sx/2.,wrx)
422         for j=0,yi-1 do begin
423             if wrx ne 0 then yin=where(abs(auxy(xin)-scy(j)) lt sy/2.,wry)$
424             else wry=0
425             if wry ne 0 then ob(i,j)=total(sphim(xin(yin))) else ob(i,j)=0.
426             endfor
427         endfor
428     ; Rebinning of HST subpixels into GAIA samples
429
430     ; CONVOLUTION WITH PSF
431     ob=kconvol(ob,psf)
432     ; !!! Note the use of kconvol instead of convol !!!
433
434     ; NOISE
435     ;obmed=median(ob)
436     ;ob=poidev(ob>obmed,seed=seed)
437     ; The use of the > operator overestimates the photon noise, but avoids
438     ;  possible problems connected with the use of the poidev function with
439     ;  an argument containing mostly very small numbers
440     ob=poidev(ob,seed=seed)
441     ob=ob+randomn(seed,xi,yi)*rn
442     ; Addition of photon noise and readnoise
443
444     ; NTH OBSERVATION
445     obs(n,*,*)=ob
446
447     ; SUBSAMPLING OF GAIA OBSERVATION
448     ssob=rebin(ob,xi*ssfx,yi*ssfy,/sample)/(ssfx*ssfy)
449     ; subsampling of each sample into ssfx*ssfy subsamples
450
451     ; COORDINATES OF SUBSAMPLES' CENTERS IN THE HST FOR
452     auxx   =+(sscx#(fltarr(yi*ssfy)+1.))*cos(posa(n))$
```

```
453     -((fltarr(xi*ssfx)+1.)#sscy)*sin(posa(n))$
454     +cx(n)
455     auxy  =+(sscx#(fltarr(yi*ssfy)+1.))*sin(posa(n))$
456     +((fltarr(xi*ssfx)+1.)#sscy)*cos(posa(n))$
457     +cy(n)
458
459     ; REBINNING OF GAIA PARTIAL FLUX MAP
460     for i=0,gsize-1 do begin
461         xin=where(abs(auxx-fmgrid(i)) lt gstep/2.,wrx)
462         for j=0,gsize-1 do begin
463             if wrx ne 0 then yin=where(abs(auxy(xin)-fmgrid(j)) lt gstep/2.,wry)$
464             else wry=0
465             if wry ne 0 then pfm(i,j)=total(ssob(xin(yin))) else pfm(i,j)=0.
466             endfor
467         endfor
468     ; Rebinning of GAIA subsamples into GAIA partial flux map
469
470     ; NTH PARTIAL FLUX MAP
471     nfm(n,*,*)=pfm
472
473     endfor
474
475 ; GAIA GLOBAL FLUX MAP
476 gfm=total(nfm,1)
477
478 ; FLUX MAP IN MAGNITUDES
479 parn=(nobs*gaiaet/exptime)*(gstep^2/hpix^2)*(gain*parhstdn)
480 gfmmag=-2.5*alog10(gfm>parn)
481 gfmmax=max(gfmmag,min=gfmmin)
482 ; GAIA flux map in uncalibrated magnitudes
483 pargfmdn=parn/gain
484 gfmdnc=gfm/gain
485 ; GAIA flux map in data number counts
486 gfmmagsta=-2.5*alog10((gfmdnc>pargfmdn)/(gaiaet*nobs*(sx*sy/1000.)^2))+$
487 calpar(0,filtnu)+calpar(1,filtnu)*vi+calpar(2,filtnu)*vi^2+dm+0.1
488 ; GAIA flux map in stamag standard magnitudes
489
490 ; FLUX MAP ON SCREEN
491 ;if sc eq 'y' then begin
492 ;mag=2.
493 ;dispsize=mag*gsize
494 ;set_plot,'x'
495 ;loadct,0
496 ;window,!d.window+1,xsize=dispsize,ysize=dispsize
497 ;pfx=[0,1,1,0] & pfy=[0,0,1,1]
498 ;for i=0,gsize-1 do for j=0,gsize-1 do begin
499 ;polyfill,mag*(pfx+i),mag*(pfy+j),color=round((gfmmag(i,j)-gfmmin)/$
500 ; (gfmmax-gfmmin)*255.),/device
501 ;endfor
502 ;endif
503
504 if sc eq 'y' then begin
505     mag=2.
506     dispsize=mag*gsize
```

```
507      gfmmagsc=rebin(gfmmag,dispsize,dispsize,/sample)
508      set_plot,'x'
509      loadct,0
510      window,!d.window+1,xsize=dispsize,ysize=dispsize
511      tvscl,gfmmagsc
512      endif
513
514 ; SAVE FLUX MAP INTO AN EPS FILE
515 if ps eq 'y' then begin
516      set_plot,'ps'
517      device,filename=fn+'.eps',xsize=fms,ysize=fms,xoffset=(21.-fms)/2.,$
518      yoffset=(29.7-fms)/2.,/encapsulated,bits_per_pixel=8
519      tvscl,gfmmag,xsize=fms,ysize=fms,/centimeters
520      device,/close
521      set_plot,'x'
522      endif
523 ; Note that the image is centered on an a4 page
524
525 ; SAVE IMPORTANT DATA INTO AN IDL STRUCTURE
526 if st eq 'y' then begin
527      ; Simulation Structure
528      result=execute('simstr={dadsfile:dadsfile,date:date,instrume:instrume'+$
529      ',camerastr:camerastr,targname:targname,ra_targ:ra_targ,dec_targ:dec_targ'+$
530      ',pa_v3:pa_v3,filtnam1:filtnam1,filtnam2:filtnam2,filtnu:filtnu'+$
531      ',atodgain:atodgain,gain:gain,photflam:photflam,photzpt:photzpt'+$
532      ',calpar:calpar,vi:vi,dm:dm,hpix:hpix,exptime:exptime,hstdnc:hstdnc'+$
533      ; ',hstelc:hstelc,hstmagins:hstmagins'+$
534      ',muback:muback,parhstdn:parhstdn,hstmagsta:hstmagsta,hstmag:hstmag'+$
535      ',rdim:rdim,hstmagcen:hstmagcen'+$
536      ',ss:ss,ssstr:ssstr,nobs:nobs,sd:sd,posa:posa,cx:cx,cy:cy,gaiaet:gaiaet'+$
537      ',rn:rn,spfx:spfx,spfy:spfy,obs:obs'+$
538      ',ssfx:ssfx,ssfy:ssfy,gstep:gstep,gsize:gsize,nfm:nfm,gfm:gfm,parn:parn'+$
539      ',gfmmag:gfmmag,gfmmagsta:gfmmagsta'+$
540      ',px:px,py:py,psx:psx,psy:psy,sx:sx,sy:sy,xi:xi,yi:yi}')
541      endif
542
543 ; SAVE IMPORTANT DATA INTO A DAT FILE
544 if stfile eq 'y' then begin
545      save,filename=simfn+'.dat',/verbose,simstr
546      endif
547
548 end
```

G.2   STACK_BIS.PRO

This program stacks a set of GAIA BBP simulated observations generated by SIM_STACK.PRO into a flux map using the alternative technique mentioned at the end of Section 6.4.

```
1 ;    PROGRAM               STACK_BIS.PRO
2
3 ; Last Updated           07 Jun 2000          Mattia Vaccari
4
5 ; This program stacks a set of GAIA BBP simulated observations of an HST WFPC2
```

```
 6 ;  field generated by SIM_STACK.PRO into a GAIA flux map.
 7
 8 lsc:
 9 print,'Do you want to display GAIA flux map on screen (y/n)?'
10 sc='...' & read,sc
11 if sc ne 'y' and sc ne 'n' then begin
12     print,'Invalid choice!'
13     goto,lsc
14     endif
15
16 lps:
17 print,'Do you want to save the flux map in magnitudes to an eps file (y/n)?'
18 ps='...' & read,ps
19 if ps ne 'y' and ps ne 'n' then begin
20     print,'Invalid choice!'
21     goto,lps
22     endif
23 if ps eq 'y' then begin
24     print,'Enter filename without the .eps extension:'
25     fn='fluxmap.eps' & read,fn
26     print,'Enter the side of the image in centimetres:'
27     fms=16. & read,fms
28     endif
29
30 lst:
31 print,'Do you want to save the important data into an IDL structure (y/n)?'
32 st='...' & read,st
33 if st ne 'y' and st ne 'n' then begin
34     print,'Invalid choice!'
35     goto,lst
36     endif
37 if st eq 'y' then begin
38     lstfile:
39     print,'Do you want to save this structure into a dat file (y/n)?'
40     stfile='...' & read,stfile
41     if stfile ne 'y' and stfile ne 'n' then begin
42         print,'Invalid choice!'
43         goto,lstfile
44         endif
45     if stfile eq 'y' then begin
46         print,'Enter filename without the .dat extension:'
47         simfn='sim_data.dat' & read,simfn
48         endif
49     endif
50
51 ; RETRIEVE DATA FROM SIMSTR STRUCTURE
52 dadsfile=simstr.dadsfile & date=simstr.date & instrume=simstr.instrume
53 camerastr=simstr.camerastr &targname=simstr.targname & ra_targ=simstr.ra_targ
54 dec_targ=simstr.dec_targ & pa_v3=simstr.pa_v3 & filtnam1=simstr.filtnam1
55 filtnam2=simstr.filtnam2 & filtnu=simstr.filtnu & atodgain=simstr.atodgain
56 gain=simstr.gain & photflam=simstr.photflam & photzpt=simstr.photzpt
57 calpar=simstr.calpar & vi=simstr.vi & dm=simstr.dm & hpix=simstr.hpix
58 exptime=simstr.exptime & hstdnc=simstr.hstdnc
59 ; hstelc=simstr.hstelc & hstmagins=simstr.hstmagins
```

```
60 muback=simstr.muback & parhstdn=simstr.parhstdn & hstmagsta=simstr.hstmagsta
61 hstmag=simstr.hstmag & rdim=simstr.rdim & hstmagcen=simstr.hstmagcen
62 ss=simstr.ss & ssstr=simstr.ssstr & nobs=simstr.nobs & sd=simstr.sd
63 posa=simstr.posa & cx=simstr.cx & cy=simstr.cy & gaiaet=simstr.gaiaet
64 rn=simstr.rn & spfx=simstr.spfx & spfy=simstr.spfy & obs=simstr.obs
65 ssfx=simstr.ssfx & ssfy=simstr.ssfy & gstep=simstr.gstep & gsize=simstr.gsize
66 parn=simstr.parn & px=simstr.px & py=simstr.py & psx=simstr.psx
67 psy=simstr.psy & sx=simstr.sx & sy=simstr.sy & xi=simstr.xi & yi=simstr.yi
68
69 print,'Stacking GAIA ',ssstr,' pixels/sample BBP simulated observations.'
70 print,'Please wait...'
71
72 ; FLUX MAP GRID IN THE HST FOR
73 fmgrid=fltarr(2,gsize^2)
74 k=0l
75 for i=0,gsize-1 do for j=0,gsize-1 do begin
76     fmgrid(*,k)=[i-(gsize-1)/2,j-(gsize-1)/2]*gstep
77     k=k+1
78     endfor
79 ; fmgrid is a (2,gsize^2) array containing along its 2 columns the x and y
80 ;  coordinates of the gsize^2 flux map grid points in the HST FOR.
81 ;  The first row contains the coordinate of the point at the lower left corner
82 ;  of the grid and the two columns are ordered first bottom/up and then
83 ;  left/right (which is the order in which IDL dipslays 2-D arrays).
84 ;  The essentially 2-D arrays folded into 1-D arrays that will be used in the
85 ;  following for the sake of efficiency will maintain the same ordering.
86
87 ; FLUX MAP GRID IN THE OBSERVATION FOR
88 ones=replicate(1.,gsize^2)
89 ;obsfmx=[[+cos(posa)],[+sin(posa)]]#fmgrid+$
90 ; diag([[+cos(posa)],[+sin(posa)]]#transpose([[cx],[cy]]))#ones
91 ;obsfmy=[[-sin(posa)],[+cos(posa)]]#fmgrid+$
92 ; diag([[-sin(posa)],[+cos(posa)]]#transpose([[cx],[cy]]))#ones
93 ;obsfmx=[[+cos(posa)],[-sin(posa)]]#fmgrid+cx#transpose(ones)
94 ;obsfmy=[[+sin(posa)],[+cos(posa)]]#fmgrid+cy#transpose(ones)
95 obsfmx=[[+cos(posa)],[+sin(posa)]]#fmgrid-$
96 diag([[+cos(posa)],[+sin(posa)]]#transpose([[cx],[cy]]))#ones
97 obsfmy=[[-sin(posa)],[+cos(posa)]]#fmgrid-$
98 diag([[-sin(posa)],[+cos(posa)]]#transpose([[cx],[cy]]))#ones
99 ; obsfmx and obsfmy are (nobs,gsize^2) arrays containing the x and y
100 ;  coordinates of the flux map elements in the observation for
101
102 ; OBSERVATIONS' REBINNING
103 obsreb=rebin(obs,nobs,xi*ssfx,yi*ssfy,/sample)/(ssfx*ssfy)
104
105 ; ASSIGNMENT OF A SUBSAMPLE VALUE TO EACH FLUX MAP ELEMENT
106 xin=round(obsfmx/(sx/ssfx)+0.5*(xi*ssfx-1))
107 yin=round(obsfmy/(sy/ssfy)+0.5*(yi*ssfy-1))
108 ; xin and yin express obsfmx and obsfmy in samples
109 nfm=fltarr(nobs,gsize^2)
110 for n=0,nobs-1 do nfm(n,*)=obsreb([intarr(gsize^2)+n],[xin(n,*)],[yin(n,*)])
111 ;nfm=obsreb(indgen(nobs)#replicate(1,gsize^2),$
112 ; round(obsfmx/(sx/ssfx)+0.5*(xi*ssfx-1)),$
113 ; round(obsfmy/(sy/ssfy)+0.5*(yi*ssfy-1)))
```

```
114 ; nfm now contains along its nobs columns the sample value of the sample
115 ;  whose centre is nearest to each flux map element for each observation
116 ; In other words, nfm contains along its nobs columns the nobs
117 ;  one-dimensional partial flux maps
118
119 nfm=transpose(reform(nfm,nobs,gsize,gsize),[0,2,1])
120 ; nfm now contains the nobs two-dimensional partial flux maps
121 gfm=total(nfm,1)
122 ; gfm is the two-dimensional GAIA glaobal flux map
123
124 ; FLUX MAP IN MAGNITUDES
125 gfmmag=-2.5*alog10(gfm>parn)
126 gfmmax=max(gfmmag,min=gfmmin)
127 ; GAIA flux map in uncalibrated magnitudes
128 pargfmdn=parn/gain
129 gfmdnc=gfm/gain
130 ; GAIA flux map in data number counts
131 gfmmagsta=-2.5*alog10((gfmdnc>pargfmdn)/(gaiaet*nobs*(sx*sy/1000.)^2))+$
132 calpar(0,filtnu)+calpar(1,filtnu)*vi+calpar(2,filtnu)*vi^2+dm+0.1
133 ; GAIA flux map in stamag standard magnitudes
134
135 ; FLUX MAP ON SCREEN
136 ;if sc eq 'y' then begin
137 ;mag=2.
138 ;dispsize=mag*gsize
139 ;set_plot,'x'
140 ;loadct,0
141 ;window,!d.window+1,xsize=dispsize,ysize=dispsize
142 ;pfx=[0,1,1,0] & pfy=[0,0,1,1]
143 ;for i=0,gsize-1 do for j=0,gsize-1 do begin
144 ;polyfill,mag*(pfx+i),mag*(pfy+j),color=round((gfmmag(i,j)-gfmmin)/$
145 ; (gfmmax-gfmmin)*255.),/device
146 ;endfor
147 ;endif
148
149 if sc eq 'y' then begin
150     mag=2.
151     dispsize=mag*gsize
152     gfmmagsc=rebin(gfmmag,dispsize,dispsize,/sample)
153     set_plot,'x'
154     loadct,0
155     window,!d.window+1,xsize=dispsize,ysize=dispsize
156     tvscl,gfmmagsc
157     endif
158
159 ; SAVE FLUX MAP INTO AN EPS FILE
160 if ps eq 'y' then begin
161     set_plot,'ps'
162     device,filename=fn+'.eps',xsize=fms,ysize=fms,xoffset=(21.-fms)/2.,$
163     yoffset=(29.7-fms)/2.,/encapsulated,bits_per_pixel=8
164     tvscl,gfmmag,xsize=fms,ysize=fms,/centimeters
165     device,/close
166     set_plot,'x'
167     endif
```

```
168 ; Note that the image is centered on an a4 page
169
170 ; SAVE IMPORTANT DATA INTO AN IDL STRUCTURE
171 if st eq 'y' then begin
172     ; Simulation Structure
173     result=execute('simstr_bis={dadsfile:dadsfile,date:date,instrume:instrume'+$
174     ',camerastr:camerastr,targname:targname,ra_targ:ra_targ,dec_targ:dec_targ'+$
175     ',pa_v3:pa_v3,filtnam1:filtnam1,filtnam2:filtnam2,filtnu:filtnu'+$
176     ',atodgain:atodgain,gain:gain,photflam:photflam,photzpt:photzpt'+$
177     ',calpar:calpar,vi:vi,dm:dm,hpix:hpix,exptime:exptime,hstdnc:hstdnc'+$
178     ; ',hstelc:hstelc,hstmagins:hstmagins'+$
179     ',muback:muback,parhstdn:parhstdn,hstmagsta:hstmagsta,hstmag:hstmag'+$
180     ',rdim:rdim,hstmagcen:hstmagcen'+$
181     ',ss:ss,ssstr:ssstr,nobs:nobs,sd:sd,posa:posa,cx:cx,cy:cy,gaiaet:gaiaet'+$
182     ',rn:rn,spfx:spfx,spfy:spfy,obs:obs'+$
183     ',ssfx:ssfx,ssfy:ssfy,gstep:gstep,gsize:gsize,nfm:nfm,gfm:gfm,parn:parn'+$
184     ',gfmmag:gfmmag,gfmmagsta:gfmmagsta'+$
185     ',px:px,py:py,psx:psx,psy:psy,sx:sx,sy:sy,xi:xi,yi:yi}')
186     endif
187
188 ; SAVE IMPORTANT DATA INTO A DAT FILE
189 if stfile eq 'y' then begin
190     save,filename=simfn+'.dat',/verbose,simstr_bis
191     endif
192
193 end
```

G.3   STACK_TRIS.PRO

This program stacks a set of GAIA BBP simulated observations generated by SIM_STACK.PRO into a flux map using the drizzling technique mentioned at the end of Section 6.4 and described in Appendix F.

```
 1 ;   PROGRAM             STACK_TRIS.PRO
 2
 3 ; Last Updated          09 Jun 2000      Mattia Vaccari
 4
 5 ; This program stacks a set of GAIA BBP simulated observations of an HST WFPC2
 6 ;  field generated by SIM_STACK.PRO into a GAIA flux map.
 7 ; The technique used in the stacking is inspired by the drizzling technique
 8 ;  devised for HST Deep Field North (Williams et al. 1996)
 9
10 lsc:
11 print,'Do you want to display GAIA flux map on screen (y/n)?'
12 sc='...' & read,sc
13 if sc ne 'y' and sc ne 'n' then begin
14     print,'Invalid choice!'
15     goto,lsc
16     endif
17
18 lps:
19 print,'Do you want to save the flux map in magnitudes to an eps file (y/n)?'
20 ps='...' & read,ps
```

```
21 if ps ne 'y' and ps ne 'n' then begin
22     print,'Invalid choice!'
23     goto,lps
24     endif
25 if ps eq 'y' then begin
26     print,'Enter filename without the .eps extension:'
27     fn='fluxmap.eps' & read,fn
28     print,'Enter the side of the image in centimetres:'
29     fms=16. & read,fms
30     endif
31
32 lst:
33 print,'Do you want to save the important data into an IDL structure (y/n)?'
34 st='...' & read,st
35 if st ne 'y' and st ne 'n' then begin
36     print,'Invalid choice!'
37     goto,lst
38     endif
39 if st eq 'y' then begin
40     lstfile:
41     print,'Do you want to save this structure into a dat file (y/n)?'
42     stfile='...' & read,stfile
43     if stfile ne 'y' and stfile ne 'n' then begin
44         print,'Invalid choice!'
45         goto,lstfile
46         endif
47     if stfile eq 'y' then begin
48         print,'Enter filename without the .dat extension:'
49         simfn='sim_data.dat' & read,simfn
50         endif
51     endif
52
53 ; RETRIEVE DATA FROM SIMSTR STRUCTURE
54 dadsfile=simstr.dadsfile & date=simstr.date & instrume=simstr.instrume
55 camerastr=simstr.camerastr &targname=simstr.targname & ra_targ=simstr.ra_targ
56 dec_targ=simstr.dec_targ & pa_v3=simstr.pa_v3 & filtnam1=simstr.filtnam1
57 filtnam2=simstr.filtnam2 & filtnu=simstr.filtnu & atodgain=simstr.atodgain
58 gain=simstr.gain & photflam=simstr.photflam & photzpt=simstr.photzpt
59 calpar=simstr.calpar & vi=simstr.vi & dm=simstr.dm & hpix=simstr.hpix
60 exptime=simstr.exptime & hstdnc=simstr.hstdnc
61 ; hstelc=simstr.hstelc & hstmagins=simstr.hstmagins
62 muback=simstr.muback & parhstdn=simstr.parhstdn & hstmagsta=simstr.hstmagsta
63 hstmag=simstr.hstmag & rdim=simstr.rdim & hstmagcen=simstr.hstmagcen
64 ss=simstr.ss & ssstr=simstr.ssstr & nobs=simstr.nobs & sd=simstr.sd
65 posa=simstr.posa & cx=simstr.cx & cy=simstr.cy & gaiaet=simstr.gaiaet
66 rn=simstr.rn & spfx=simstr.spfx & spfy=simstr.spfy & obs=simstr.obs
67 ssfx=simstr.ssfx & ssfy=simstr.ssfy & gstep=simstr.gstep & gsize=simstr.gsize
68 parn=simstr.parn & px=simstr.px & py=simstr.py & psx=simstr.psx
69 psy=simstr.psy & sx=simstr.sx & sy=simstr.sy & xi=simstr.xi & yi=simstr.yi
70
71 print,'Stacking GAIA ',ssstr,' pixels/sample BBP simulated observations.'
72 print,'Please wait...'
73
74 ; ARRAYS' CREATION
```

```
75 sscx=reform(transpose((((findgen(xi)-0.5*(xi-1))*sx)#replicate(1,ssfx)),xi*ssfx)+$
76 reform((((findgen(ssfx)-0.5*(ssfx-1))*(0.5*sx/ssfx))#replicate(1,xi),xi*ssfx)
77 sscy=reform(transpose((((findgen(yi)-0.5*(yi-1))*sy)#replicate(1,ssfy)),yi*ssfy)+$
78 reform((((findgen(ssfy)-0.5*(ssfy-1))*(0.5*sy/ssfy))#replicate(1,yi),yi*ssfy)
79 ; sscx and sscy contain the coordinates of subsamples' centers
80 ;  in the observation FOR
81 fmgrid=(findgen(gsize)-0.5*(gsize-1))*gstep
82 ; Coordinates of the centers of the flux map elements in the HST FOR
83 pfm=fltarr(gsize,gsize)
84 ; pfm will contain the partial flux map
85 nfm=fltarr(nobs,gsize,gsize)
86 ; nfm will contain the nobs partial flux maps
87 gfm=fltarr(gsize,gsize)
88 ; gfm will contain the global flux map
89
90 for n=0,nobs-1 do begin
91
92     ; RETRIEVE NTH OBSERVATION
93     ob=reform(obs(n,*,*))
94
95     ; SUBSAMPLING OF GAIA OBSERVATION
96     ssob=rebin(ob,xi*ssfx,yi*ssfy,/sample)/(ssfx*ssfy)
97     ; subsampling of each sample into ssfx*ssfy subsamples
98
99     ; COORDINATES OF SUBSAMPLES' CENTERS IN THE HST FOR
100    auxx   =+(sscx#(fltarr(yi*ssfy)+1.))*cos(posa(n))$
101    -((fltarr(xi*ssfx)+1.)#sscy)*sin(posa(n))$
102    +cx(n)
103    auxy   =+(sscx#(fltarr(yi*ssfy)+1.))*sin(posa(n))$
104    +((fltarr(xi*ssfx)+1.)#sscy)*cos(posa(n))$
105    +cy(n)
106
107    ; REBINNING OF GAIA PARTIAL FLUX MAP
108    for i=0,gsize-1 do begin
109        xin=where(abs(auxx-fmgrid(i)) lt gstep/2.,wrx)
110        for j=0,gsize-1 do begin
111            if wrx ne 0 then yin=where(abs(auxy(xin)-fmgrid(j)) lt gstep/2.,wry)$
112            else wry=0
113            if wry ne 0 then pfm(i,j)=total(ssob(xin(yin))) else pfm(i,j)=0.
114            endfor
115        endfor
116    ; Rebinning of GAIA subsamples into GAIA partial flux map
117
118    ; NTH PARTIAL FLUX MAP
119    nfm(n,*,*)=pfm
120
121    endfor
122
123 ; GAIA GLOBAL FLUX MAP
124 gfm=total(nfm,1)
125
126 ; FLUX MAP IN MAGNITUDES
127 gfmmag=-2.5*alog10(gfm>parn)
128 gfmmax=max(gfmmag,min=gfmmin)
```

```
129 ; GAIA flux map in uncalibrated magnitudes
130 pargfmdn=parn/gain
131 gfmdnc=gfm/gain
132 ; GAIA flux map in data number counts
133 gfmmagsta=-2.5*alog10((gfmdnc>pargfmdn)/(gaiaet*nobs*(sx*sy/1000.)^2))+$
134 calpar(0,filtnu)+calpar(1,filtnu)*vi+calpar(2,filtnu)*vi^2+dm+0.1
135 ; GAIA flux map in stamag standard magnitudes
136
137 ; FLUX MAP ON SCREEN
138 ;if sc eq 'y' then begin
139 ;mag=2.
140 ;dispsize=mag*gsize
141 ;set_plot,'x'
142 ;loadct,0
143 ;window,!d.window+1,xsize=dispsize,ysize=dispsize
144 ;pfx=[0,1,1,0] & pfy=[0,0,1,1]
145 ;for i=0,gsize-1 do for j=0,gsize-1 do begin
146 ;polyfill,mag*(pfx+i),mag*(pfy+j),color=round((gfmmag(i,j)-gfmmin)/$
147 ; (gfmmax-gfmmin)*255.),/device
148 ;endfor
149 ;endif
150
151 if sc eq 'y' then begin
152     mag=2.
153     dispsize=mag*gsize
154     gfmmagsc=rebin(gfmmag,dispsize,dispsize,/sample)
155     set_plot,'x'
156     loadct,0
157     window,!d.window+1,xsize=dispsize,ysize=dispsize
158     tvscl,gfmmagsc
159     endif
160
161 ; SAVE FLUX MAP INTO AN EPS FILE
162 if ps eq 'y' then begin
163     set_plot,'ps'
164     device,filename=fn+'.eps',xsize=fms,ysize=fms,xoffset=(21.-fms)/2.,$
165     yoffset=(29.7-fms)/2.,/encapsulated,bits_per_pixel=8
166     tvscl,gfmmag,xsize=fms,ysize=fms,/centimeters
167     device,/close
168     set_plot,'x'
169     endif
170 ; Note that the image is centered on an a4 page
171
172 ; SAVE IMPORTANT DATA INTO AN IDL STRUCTURE
173 if st eq 'y' then begin
174     ; Simulation Structure
175     result=execute('simstr_tris={dadsfile:dadsfile,date:date,instrume:instrume'+$
176     ',camerastr:camerastr,targname:targname,ra_targ:ra_targ,dec_targ:dec_targ'+$
177     ',pa_v3:pa_v3,filtnam1:filtnam1,filtnam2:filtnam2,filtnu:filtnu'+$
178     ',atodgain:atodgain,gain:gain,photflam:photflam,photzpt:photzpt'+$
179     ',calpar:calpar,vi:vi,dm:dm,hpix:hpix,exptime:exptime,hstdnc:hstdnc'+$
180     ; ',hstelc:hstelc,hstmagins:hstmagins'+$
181     ',muback:muback,parhstdn:parhstdn,hstmagsta:hstmagsta,hstmag:hstmag'+$
182     ',rdim:rdim,hstmagcen:hstmagcen'+$
```

```
183     ',ss:ss,ssstr:ssstr,nobs:nobs,sd:sd,posa:posa,cx:cx,cy:cy,gaiaet:gaiaet'+$
184     ',rn:rn,spfx:spfx,spfy:spfy,obs:obs'+$
185     ',ssfx:ssfx,ssfy:ssfy,gstep:gstep,gsize:gsize,nfm:nfm,gfm:gfm,parn:parn'+$
186     ',gfmmag:gfmmag,gfmmagsta:gfmmagsta'+$
187     ',px:px,py:py,psx:psx,psy:psy,sx:sx,sy:sy,xi:xi,yi:yi}')
188     endif
189
190 ; SAVE IMPORTANT DATA INTO A DAT FILE
191 if stfile eq 'y' then begin
192     save,filename=simfn+'.dat',/verbose,simstr_tris
193     endif
194
195 end
```

References

Abraham R.G. et al. 1996a, The Morphologies of Distant Galaxies. II. Classifications from the Hubble Space Telescope Medium Deep Survey, The Astrophysical Journal Supplement Series, 107, 1–17

Abraham R.G. et al. 1996b, Galaxy morphology to $I = 25$ in the Hubble Deep Field, Monthly Notices of the Royal Astronomical Society, 279, L47–52

Andredakis Y.C., Peletier R.F. and Balcells M. 1995, The Shape of the Luminosity Profiles of Bulges of Spiral Galaxies, Monthly Notices of the Royal Astronomical Society, 275, 874

Arias E.F., Charlot P., Feissel M. and Lestrade J.-F. 1995, The Extragalactic Reference System of the International Earth Rotation Service, ICRS, Astronomy and Astrophysics, 303, 604–608

Binney J. and Merrifield M. 1998, Galactic Astronomy, Princeton University Press

Biretta J.A. et al. 1996, WFPC2 Instrument Handbook, Version 4.0, Baltimore, Space Telescope Science Institute

Boroson T. 1981, The Distribution of Luminosity in Spiral Galaxies, The Astrophysical Journal Supplement Series, 46, 177–209

Byun Y.I. and Freeman K.C. 1995, Two-Dimensional Decomposition of Bulge and Disk, The Astrophysical Journal, 448, 563

Byun Y.I. et al. 1996, The Centers of Early-Type Galaxies with HST. II. Empirical Models and Structural Parameters The Astronomical Journal, 111, 1889–1900

Caon N., Capaccioli M. and D'Onofrio M. 1993, On the shape of the light profiles of early-type galaxies, Monthly Notices of the Royal Astronomical Society, 265, 1013–1021

Capaccioli M., Piotto G.P. and Rampazzo R. 1988, Photographic and CCD Surface Photometry of nine Early-Type Galaxies, The Astronomical Journal, 96, 487–503

Capaccioli M., Held E.V., Lorenz H. and Vietri M. 1990, Photographic and CCD Surface Photometry of the Standard Elliptical Galaxy NGC 3379, The Astronomical Journal, 99, 1813–1822

Carollo C.M. 1999, The Centers of Early- to Intermediate-Type Spiral Galaxies: A Structural Analysis, The Astrophysical Journal, 523, 566–574

Casertano S. et al. 1995, Structural Parameters of Faint Galaxies from Prerefurbishment Hubble Space Telescope Medium Deep Survey Observations, The Astrophysical Journal, 453, 599-610

de Vaucouleurs G. 1948, Recherches sur les Nebuleuses Extragalactiques, Annales d'Astrophysique, 11, 247

de Vaucouleurs G. 1959, in "Handbuch der Physik", 53, 275, ed. Flügge J., Springer Verlag

de Vaucouleurs G., de Vaucouleurs A., Corwin H.G., Buta R.J., Paturel G. and Fouqué P. 1991, Third Reference Catalogue of Bright Galaxies, Springer Verlag, New York

ESA 1997a, The Hipparcos and Tycho Catalogues, ESA SP–1200

ESA 1997b, Proceedings of the ESA Symposium "Hipparcos – Venice '97", eds. Battrick B., Perryman M.A.C. and Bernacca P.L., ESA SP–402

ESA 2000, GAIA Concept and Technology Study Report, in preparation, a draft version of the Science Section of the report is available at the web page http://astro.estec.esa.nl/GAIA/Science/Science.html, maintained by the Astrophysics Division, Space Science Department, ESTEC, ESA

Faber S.M. et al. 1997, The Centers of Early-Type Galaxies with HST. IV. Central Parameter Relations, The Astronomical Journal, 114, 1771–1796

Freeman K.C. 1970, On the Disks of Spiral and S0 galaxies, The Astrophysical Journal, 160, 811–830

Gilmore G. 1998, SAG_GG_05

Gilmore G. et al. 1998, GAIA: Origin and Evolution of the Milky Way, in "Astronomical Interferometry", SPIE Proceedings, 3350, 541–550

Glazebrook K., Ellis R., Santiago B. and Griffiths R. 1995, The morphological identification of the rapidly evolving population of faint galaxies, Monthly Notices of the Royal Astronomical Society, 275, L19–22

Høg E. 1993, Astrometry and Photometry of 400 million stars brighter than 18 mag, in "Developments in Astrometry and their impact on Astrophysics and Geophysics", IAU Symposium 156, 37–45

Høg E. 1995, A new era of global astrometry. II: a 10 microarcsecond mission, in "Astronomical and Astrophysical Objectives of sub-milliarcsecond Astrometry", IAU Symposium 166, 317–322

Høg E. 1999, Self-consistency in the photometric design, SAG_CUO_68[1]

---

[1] SAG_AUT_NN refers to the NNth technical report presented to the European Space Agency Science Advisory Group for the GAIA mission by the author specified by the AUT abbreviation. The abbreviation CUO, in particular, stands for Copenhagen University Observatory.

Høg E., Fabricius C., Knude J. and Makarov V.V. 1998a, GAIA Surveys of Nebulae and Sky Background, SAG_CUO_32

Høg E., Fabricius C., Knude J. and Makarov V.V. 1998b, GAIA Surveys of Surface Brightness, SAG_CUO_39

Høg E., Fabricius C., Knude J. and Makarov V.V. 1999, Sky Survey and Photometry by the GAIA Satellite, Baltic Astronomy, 8, 25–56, SAG_CUO_53

Høg E., Knude J. and Straižys V. 1999, Specification of GAIA photometric systems, SAG_CUO_58

Høg E. et al. 1998, The Tycho Reference Catalogue, Astronomy and Astrophysics, 335, L65–L68

Høg E. et al. 1998, Progress on the Tycho-2 Catalogue from the Hipparcos Mission, Proceedings of the International Colloquium "Modern Astrometry and Astrodynamics"

Høg E. et al. 2000a, The Tycho-2 Catalogue of the 2.5 Million Brightest Stars, Astronomy and Astrophysics, in press

Høg E. et al. 2000b, Construction and verification of the Tycho-2 Catalogue, Astronomy and Astrophysics, in press

Holtzman J. et al. 1995a, The Performance and Calibration of the WFPC2 on the Hubble Space Telescope, Publications of the Astronomical Society of the Pacific, 107, 156–178

Holtzman J. et al. 1995b, The Photometric Performance and Calibration of WFPC2, Publications of the Astronomical Society of the Pacific, 107, 1065–1093

Hoskin M. (ed.) 1999, The Cambridge Concise History of Astronomy, Cambridge University Press

Hubble E. 1926, Extra-Galactic Nebulae, The Astrophysical Journal, 54, 321–369

Hubble E.P. 1936, The Realm of the Nebulae, Yale University Press

Im M., Casertano S., Griffiths R.E. and Ratnatunga K.U. 1995, A Test of Galaxy Evolutionary Models through Angular Sizes, The Astrophysical Journal, 441, 494–504

Impey C. and Bothun G. 1997, Low Surface Brightness Galaxies, Annual Review of Astronomy and Astrophysics, 35, 267–307

Jedrzejewski R.I. 1987, CCD Surface Photometry of Elliptical Galaxies — I. Observations, Reduction and Results, Monthly Notices of the Royal Astronomical Society, 226, 747–768

Kent S.M. 1985, CCD Surface Photometry of Field Galaxies. II. Bulge/Disk Decompositions, The Astrophysical Journal Supplement Series, 59, 115–159

Kinney A.L. et al. 1996, Template Ultraviolet to Near-Infrared Spectra of Star-Forming Galaxies and their Applications to K-corrections, The Astrophysical Journal, 467, 38–60

Kovalevsky J. 1995, Modern Astrometry, Astronomy and Astrophysics Library, Springer Verlag

Kovalevsky J. 1998, First results from Hipparcos, Annual Review of Astronomy and Astrophysics, 36, 99–129

Lattanzi M. 1997, Stars and Galaxies at $I = 20$, SAG_MGL_03

Lauer T.R. et al. 1995, The Centers of Early-Type Galaxies with HST. I. An Observational Survey, The Astronomical Journal, 110, 2622–2654

Leinert C. et al. 1998, The 1997 reference of diffuse night sky brightness, Astronomy and Astrophysics Supplement Series, 127, 1–99

Lindegren L. and Perryman M.A.C. 1995, A small interferometer in space for global astrometry: the GAIA concept, in "Astronomical and Astrophysical Objectives of sub-milliarcsecond Astrometry", IAU Symposium 166, 317–322

Lindegren L. and Perryman M.A.C. 1996, GAIA: Global Astrometric Interferometer for Astrophysics, Astronomy and Astrophysics Supplement Series, 116, 579–595

Lindegren L. 1998a, Point Spread Functions for GAIA including aberrations, SAG_LL_25

Lindegren L. 1998b, Simulation of GAIA Scanning of Arbitrary Directions, SAG_LL_26

Lindegren L. 2000, Detection of faint galaxies with GAIA, SAG_LL_29

Makino J., Akiyama K. and Sugimoto D. 1990, On the apparent universality of the $R^{1/4}$ law for brightness distribution in galaxies, Publications of the Astronomical Society of Japan, 42, 205–215

Mérat P., Safa F., Camus J.P., Pace O. and Perryman M.A.C. 1999, GAIA: a leading step in the understanding of the galactic structure, Baltic Astronomy, 8, 1–24

Mihalas D. and Binney J. 1981, Galactic Astronomy, Structure and Kinematics, 2nd edition, Freeman, San Francisco

Moro D. and Munari U. 2000, The Asiago Database on Photometric Systems (ADPS). I. Census parameters for 150 systems, Submitted to Astronomy and Astrophysics

Mould J.R. et al. 2000, The Hubble Space Telescope Key Project on the Extragalactic Distance Scale. XXVIII. Combining the Constraints on the Hubble Constant, The Astrophysical Journal, 529, 786–794

Munari U. 1999, A modular and consistent photometric system for GAIA, Baltic Astronomy, 8, 123–138

Munari U. and Castelli F. 2000, High resolution spectroscopy over 8500–8750 Åfor GAIA. II. A library of synthetic spectra for $T_{eff} \leq 7500$ K, Astronomy and Astrophysics Supplement Series, 141, 141–148

Okamura S. et al. 1999, Retrieving Bulge and Disk Parameters and Asymptotic Magnitudes from the Growth Curves of Galaxies, Publications of the Astronomical Society of the Pacific, 111, 31–44

O'Mullane W. and Lindegren L. 1999, An Object-Oriented Framework for GAIA Data Processing, Baltic Astronomy, 8, 57–72

Pace O. 1997, Lagrangian L2 or Geostationary Orbit: a system level trade-off for the GAIA mission, in "Hipparcos – Venice '97", 807–809 eds. Battrick B. Perryman M.A.C. and Bernacca P.L. ESA SP–402

Press W.H., Teukolsky S.A., Vetterling W.T. and Flannery B.P. 1992, Numerical Recipes in Fortran 77: The Art of Scientific Computing (Volume I of Fortran Numerical Recipes), Cambridge University Press

Prugniel Ph. and Héraudeau Ph. 1998, Total Magnitude, Radius, Colour Indices, Colour Gradients and Photometric Type of Galaxies, Astronomy and Astrophysics Supplement Series, 128, 299–308

Ratnatunga K.U., Griffiths R.E. and Ostrander E.J. 1999, Disk and Bulge Morphology of WFPC2 Galaxies: The Hubble Space Telescope Medium Deep Survey, The Astronomical Journal, 118, 86–107

Sandage A. 1961, The Hubble Atlas of Galaxies, Carnegie Institution of Washington, Washington D.C.

Sandage A. and Bedke J. 1994, The Carnegie Atlas of Galaxies, Carnegie Institution of Washington and the Flintridge Foundation, Washington D.C.

Sersic J.L. 1968, Atlas de Galaxias Australes, Observatorio Astronomico, Cordoba, Argentina

Shapley H. and Ames A. 1932, A survey of the external galaxies brighter than the thirteenth magnitude, Astronomical Observatory of Harvard College, Cambridge, Massachussets

Shimasaku K. and Fukugita M. 1998, The History of Galaxies and Galaxy Number Counts, The Astrophysical Journal, 501, 578–596

Straižys V. (ed.) 1999, Proceedings of the GAIA workshop, Leiden, November 23–27 1998, reproduced from Baltic Astronomy, Volume 8, Numbers 1–2

Turon C. et al. 1992, The Hipparcos Input Catalogue, ESA SP–1136

Urban S.E., Corbin T.E. and Wycoff G.L. 1998, The ACT Reference Catalog, The Astronomical Journal, 115, 2161–2166

Urban S.E. et al. 1998, The AC 2000: The Astrographic Catalogue on the system defined by the Hipparcos Catalogue, The Astronomical Journal, 115, 1212–1223

Vaccari M. and Høg E. 1999a, Statistical model of galaxies, SAG_CUO_61

Vaccari M. and Høg E. 1999b, Simulated GAIA Observations of Galaxies, SAG_CUO_69

Vaccari M., Høg E. and Makarov V.V. 1999, Three Images of M100, SAG_CUO_66

van den Bergh S. 1960, A reclassification of the northern Shapley-Ames galaxies, Publications of the David Dunlap Observatory, 2, 159–199

van den Bergh S. et al. 1996, A Morphological Catalog of Galaxies in the Hubble Deep Field, The Astronomical Journal, 112, 359–368

van den Bergh S. 1998, Galaxy Morphology and Classification, Cambridge University Press

van der Marel R.P. 1999, The Black Hole Mass Distribution in Early-Type Galaxies: Cusps in Hubble Space Telescope Photometry interpreted through Adiabatic Black Hole Growth, The Astronomical Journal, 117, 744–763

van Leeuwen F. 1997, The Hipparcos Mission, Space Science Reviews, 81, 201–409

Vannier M. 1999, Noise of GAIA Astro Instrument, SAG_MV_04

Voit M. (ed.) 1997, HST Data Handbook, Volume I: Current Instruments, Version 3.0, Baltimore, Space Telescope Science Institute

Williams R.E. et al. 1996, The Hubble Deep Field: Observations, Data Reduction and Galaxy Photometry, The Astronomical Journal, 112, 1335–1389

Acknowledgements/Ringraziamenti

In ordine approssimativamente cronologico, vorrei poi ringraziare:

- I miei genitori, le uniche persone senza le quali tutto questo non sarebbe *davvero* stato possibile: mia madre per la sua irritante pazienza e mio padre per la sua altrettanto irritante totale mancanza della stessa.

- La mia "sorellina", per avermi sempre ricordato che cosa significa, e quanto è importante, essere "giovani e stupidi".

- Maura, per esserci stata (quasi) tutte le volte in cui ce n'era bisogno.

- Gli amici conosciuti, frequentati, amati e magari dimenticati durante le mie peregrinazioni tra Padova, Copenaghen e Asiago, per avermi dato speranza.

Un affettuoso ringraziamento va infine alle "mie" macchine, `ursa.astro.ku.dk` a Copenaghen e `skoll.pd.astro.it` ad Asiago, che hanno visto la faticosa nascita di questa tesi.